Project No. 31021

WPI

Lunar Micro Rover

A Major Qualifying Project
Submitted to the Faculty of
WORCESTER POLYTECHNIC INSTITUTE
In partial fulfillment of the requirements for the
Degree of Bachelor of Science

Submitted March 24, 2023

_____ David Acuna (RBE/AE)	_____ Zachary Angell (AE)	_____ William Fisher (AE)
_____ Corbin Grubb (AE)	_____ Watts Herideen-Woodruff (AE)	_____ Lily Kinne (AE)
_____ Marcela Mayor (AE)	_____ Travis McGregor (AE)	_____ Caleb Powell (AE)

Report Submitted to:

_____
Professor Nikhil Karanjgaokar, Advisor, WPI

Abstract

The goal of this project is to design a fully autonomous micro rover for the exploration and mapping of the Moon's polar regions. NASA hopes to one-day land humans within these lunar polar regions, resulting in the need for an exploratory micro rover prototype. This project's micro rover is designed to withstand and autonomously traverse the lunar regolith while serving as the theoretical prototype of NASA's proposed idea. This is done using a 4-wheel rocker-bogie system connected to a primary pivoting point. The pivoting point allows for the rocker-bogie system to remain stable when in transit while also allowing the micro rover clearance over obstacles it may encounter on the lunar surface. The rover autonomously plans a path through the lunar terrain using an RRT* path planning algorithm. An Extended Kalman Filter is then used with IMU and GPS sensor data to estimate the rover's orientation as it traverses. This data in addition to encoder-based odometry is fed into a feedback control system to drive the rover. As the project concluded, many criteria used for designing the micro rover were successfully achieved. The results from computer simulations and real-world testing involving various components acted as the justification for the design's success and the functionality of the micro rover. Ultimately, this micro rover aims to advance the exploration and mapping of the Moon's surfaces through autonomy.

Acknowledgments

Table of Contents

List of Figures

List of Tables

Table of Authorship

Subsection	Primary Author	Primary Editor(s)
Introduction		
1.1	Marcela	Caleb
Background		
2.1	Marcela	Caleb
2.1.1	All	Marcela
2.1.2	All	Marcela
2.1.3	All	Marcela
2.1.4	All	Marcela
2.1.5	All	Marcela
2.2	All	Marcela
2.3	All	Marcela
2.4	Marcela	Caleb
2.5	Watts	Lily
2.5.1	Watts	Lily
2.5.2	Watts	Lily
2.5.3	Watts	Lily
2.5.4	Watts	Lily
2.5.5	Watts	Lily
2.5.6	Watts	Lily
2.5.7	Watts	Lily
2.5.8	Watts	Lily
2.5.9	Watts	Lily
Methodology		
3.1	Will	Marcela
3.1.1	Will	Marcela
3.1.2	Zac	Will
3.2	Will	Caleb
3.3	David	Lily
3.3.1	David	Caleb
3.4	Travis	Will
3.4.1	Travis	Will
3.4.2	Travis	Will
Design and Integration		
4.1	Will	Marcela
4.1.1	Corbin	Lily
4.1.2	Corbin	Lily
4.1.3	Corbin	Lily
4.1.4	Corbin	Lily
4.1.5	Corbin	Lily
4.2	Travis	Marcela
4.2.1	Travis	Marcela

1. Introduction

The polar regions on the Moon present an exceptional opportunity for advancing exploration and scientific discovery within our solar system, and beyond. The discovery of ice in permanently shadowed polar craters has made these regions of particular interest. However, conditions such as the extremely low-temperatures and permanent darkness within these craters pose a significant challenge to conventional solar-powered rovers. One potential solution has been proposed in which a laser on a stationary platform located on the rim of the crater is focused on a solar panel mounted on a micro-rover to power it.

The objective of this Major Qualifying Project was to design and build a small, low-power rover capable of operating on the moon to explore the dark crater interiors using laser power. This project involved various aspects of a typical capstone design project, including exploration of existing literature, experimental and numerical assessments of thermo-mechanical performance and power requirements, and subsequent testing of a prototype on rough terrain. The design constraints for the micro-rover included a maximum power requirement of 20 W, a maximum weight of 5 kg, a stowage volume of 70 centimeters by 70 centimeters x 35 centimeters, payload requirements of 2 kg, and a minimum power requirement of 2 W.

The harsh conditions of the polar regions of the Moon, including cold temperatures, radiation, and dust ingress, presented significant hazards that dictated many of the goals of this project. These hazards also influenced the specific design choices made for the micro-rover, which will be covered in depth in a later section. Given the budget and time constraints, it was not feasible to build a fully functional Moon-ready rover. Rather, this project aimed to produce a prototype for proof of concept and preliminary testing.

One significant challenge for this project was the tight time constraints. The project needed to be completed as a Major Qualifying Project within three terms, with each term lasting only seven weeks. This provided a very short amount of time to design, analyze, build, and test the rover. In addition, the project is also limited by a total budget of $2250.This further constrained the design choices making many of the optimal design options unavailable.

Overall, the project presented an exciting opportunity to contribute to NASA's goal of exploring the solar system by designing and building a small, low-power rover capable of operating in the dark crater interiors of the Moon using laser power. The original project description from WPI eProjects is shown below. This project was administered by Professor Nikhil Karanjgaokar and Professor Mohammad Mahdi Agheli Hajiabadi.

Project Description:

"NASA has a goal of a human landing on the polar regions of the moon as the next step in the human exploration of the solar system. The poles of the moon are of particular interest because orbital missions have shown that water ice can be found in the low-temperature interiors of permanently shadowed polar craters. Since these craters are in permanent darkness, conventional solar-powered rovers will not operate. One solution would be to use a laser on a stationary platform on the rim of the crater to beam light to the solar panels on a micro-rover to power it. The objective of this project is to design and build a small, low-power rover capable of operating on the moon to explore the dark crater interiors. In particular, the purpose of this project is to make a rover capable of operating on laser power in conditions like the lunar surface, the design of a stationary platform that supplies the power won't be the focus of this study. This project would involve various aspects of a typical capstone design project such as an exploration of the existing literature for designing a micro-rover capable of operating in rough and low-temperature terrain, the experimental and numerical assessment of the thermo-mechanical performance and power requirements for the micro-rover, and the subsequent testing of a prototype on rough terrain. Some design constraints for the micro-rover include:

1) Maximum power requirement – 20 W,
2) Maximum weight of micro-rover - 5 kg,
3) Stowage volume – (70 cm x 70 cm x 35 cm), and
4) Payload requirements (2 kg and power requirement 2 W).

2. Background

2.1 Past Projects Overview

To design, analyze, and fabricate a rover capable of meeting the requirements outlined in the project description, many problems must be solved. Lunar exploration is complex, and the lunar surface is an incredibly hostile environment, so the design of the Micro Rover must be carefully considered to meet the project's objectives. The purpose of this section is to review previous relevant micro rover and full-scale rover projects, to gain a better understanding of the challenges faced in a lunar environment and potential solutions to those problems. This section examines the literature on four lunar rover designs and one hopping robot, identifying the objectives, mechanical design, electrical and software architecture, mechanical and thermal analysis, fabrication, and mission profile of each project. This section also includes additional papers focusing on individual aspects of the design and analysis process, such as designing electrical subsystems and modeling the thermal behavior of a rover.

2.1.1 Virginia Tech Mission

In 2018, Virginia Polytechnic Institute and State University wrote a proposal for a robotic lunar mission sponsored by NASA in response to an AIAA Request for Proposal (RFP). The purpose of this mission was to explore the permanently shadowed regions of the lunar south pole, and in addition, gather data on the water-to-regolith ratio in two of the major craters present in the area [2]. The missions' architecture favored two identical rovers that would explore a single crater separately, rather than having a single rover that must traverse long distances between each crater [2].

Figure 1: An image of Virginia Tech's rover.
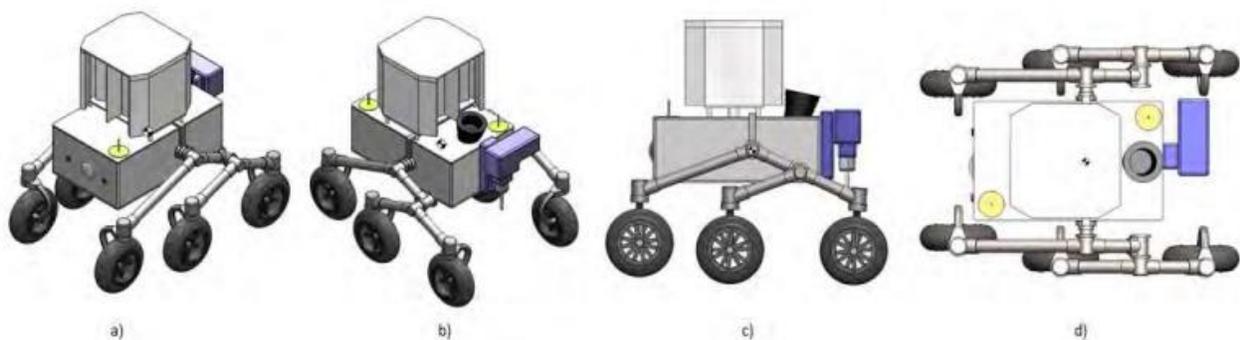
Quinn, Alison. "Engineering Views of the Lunar Rover Exterior" *American Institute of Aeronautics and Astronautics,* 2018, https://www.aiaa.org/docs/default-source/uploadedfiles/education-and-careers/university-students/design-competitions/1stplace_virginia_tech_space_design.pdf?sfvrsn=59cff8b5_0

2.1.2 Carnegie Mellon Rover (MoonRanger)

In March 2020, a team of students and professors at Carnegie Mellon University (CMU) began working on a small robotic rover for the exploration of the Moon titled MoonRanger [3]. The MoonRanger is an autonomous micro-rover designed with the intent to explore the lunar south pole. The primary mission of the rover is to confirm the presence of water or ice either on the surface or within the lunar regolith in the region. If successful, this discovery could potentially supply future human expeditions to the Moon, as well as develop propellants for fueling expeditions for deep space [3].

Figure 2: An image of Carnegie Mellon's rover, MoonRanger.
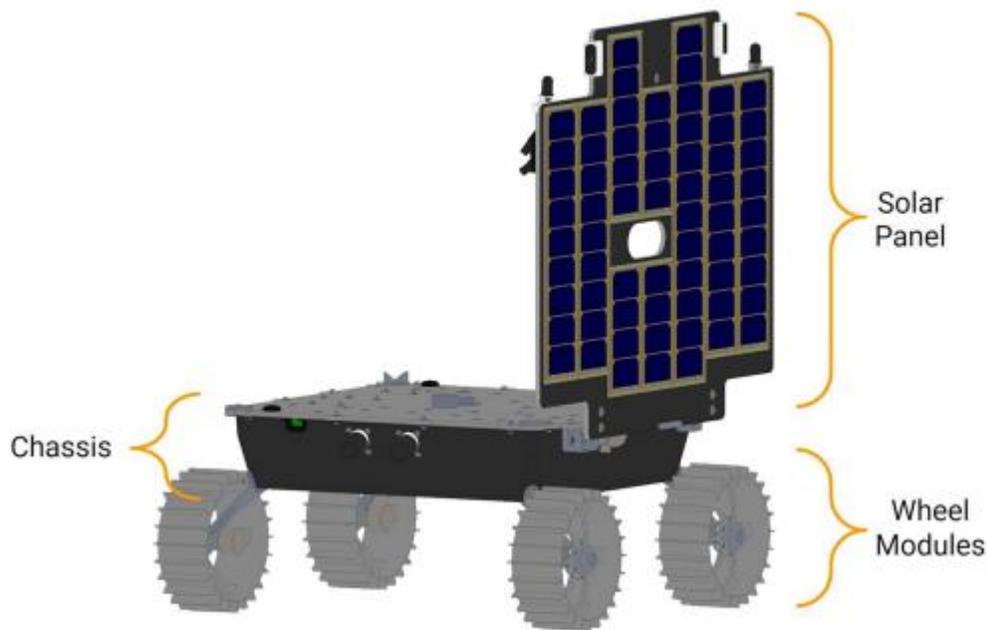
Schweitzer, Lydia. "MoonRanger rover configuration with solar panel vertically deployed" *IEEE Xplore,* 2021, https://ieeexplore.ieee.org/document/9438261

MoonRanger is the first micro rover documented as operating fully autonomously. The micro rover will be a part of NASA's Masten XL-1 lander payload which was set to launch in 2022 under the Commercial Lunar Payload Service (CLPS) [3]. Some major design constraints included a maximum mass of 18 kg, onboard system power budgets, structural integrity, and numerous autonomous

operations. Ultimately MoonRanger is being built as a proto-flight project, meaning the same rover developed on Earth will be deployed on the Moon [3].

2.1.3 WPI Lunabotics Rover

In 2021, a group of students at Worcester Polytechnic Institute (WPI) participated in NASA's Lunabotics competition to design an autonomous rover that collects gravel samples. The objective during the 2021-2022 competition was to excavate, store, and deposit gravel [4]. The team set a series of minimum goals to accomplish based on certain parameters such as battery life, rover mass, autonomy, and the amount of gravel that could be collected.

Figure 3: An image of WPI Lunabotics MQP rover.
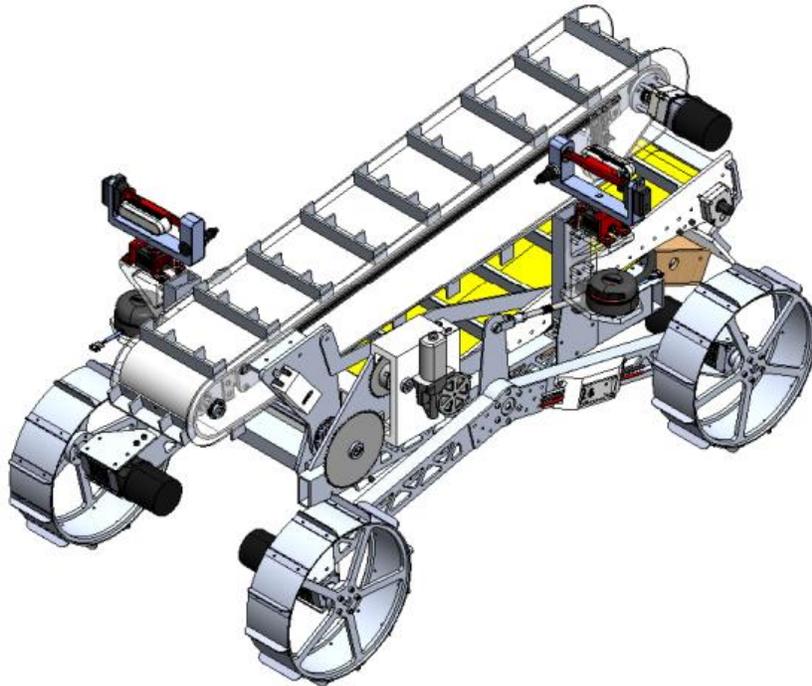
Akinyele, Jesulona. "Full Robot Assembly in Stored Configuration." *Worcester Polytechnic Institute,* 2022,
https://www.wpi.edu/news/can-you-dig-it-wpi-student-team-takes-nasa-mining-challenge

2.1.4 WPI Two-wheel Rover

In 2013, a team at WPI designed a two-wheeled micro rover as their Major Qualifying Project (MQP). The purpose of the micro rover was to assist a larger robotic rover in the exploration of an extraterrestrial rocky surface [5].

Figure 4: An image of WPI Two-wheel MQP rover.

Cunningham, Andrew. "Inspection and Reconnaissance Micro-Rover for Use in Extraterrestrial Environments." *Worcester Polytechnic Institute,* 2013, https://web.wpi.edu/Pubs/E-project/Available/E-project-042513-103357/unrestricted/WPI_Micro_Rover_Report.pdf

2.1.5 SpaceBok

SpaceBok Is a quadrupedal hopping robot developed to test the practicality and potential of the use of hopping robots within low-gravity planetary bodies. This is done by creating four-bar mechanisms in the legs, giving them two degrees of freedom for walking, and jumping motions [6].

Figure 5: An image of ETH Zürich's rover called Spacebok.

Arm, Phillip. "SpaceBok during tests at ETH Zurich" *IEEE Xplore,* 2019, https://ieeexplore.ieee.org/document/8794136

2.2 Structure and Analysis

Every micro rover researched in this project had different considerations related to the overall mission of the rover. Despite there being design differences, there were similarities and trends in the ideas and considerations within every design. The first design looked at was the micro rover designed by Virginia Tech. Each rover had a mass of 119 kg and featured a rocker-bogie suspension system [2]. The purpose of this suspension design allowed for the wheels to move upwards and downwards relative to the rover body to better cope with traversing uneven terrain. Additionally, this system also allows the micro rover's orientation to remain stable and not dramatically change as it traverses the environment. The rocker-bogie design features six drive wheels made of a super elastic Nickel-Titanium alloy mesh, with each wheel having its independent drive motor [2]. This allows the rover to overcome obstacles up to 28 cm in height based on the geometry [2]. However, there was no mention of the steering system used for each rover within this design proposal.

Similarly, the drivetrain designed for MoonRanger consisted of a 4-wheel skid drive that raised the chassis 16 cm above the ground [3]. This allowed the micro rover to have higher torque while keeping a low center of gravity. Each wheel was powered by a brushless Maxon EC-32 Flat motor for optimal weight budgeting, interfacing, and combatting the environmental hazards MoonRanger would endure

[3]. It was found through testing that this drivetrain and chassis design had a maximum traversable ascension angle of 10°, whereas the maximum descending angle was 15° [3].

A different approach was taken when considering a design for the rover produced by the Lunabotics team. The Lunabotics chassis design was composed of three subassemblies: a chassis frame, the suspension, and a drivetrain. The team needed to have a frame design that would not only be stable for mounting an excavation subassembly but also mobile enough to allow the rover to maneuver obstacles [4]. A rocker-bogie drivetrain design was chosen as the best-suited system to achieve this requirement for the frame. For better optimization, the gear ratio of the wheels in the drivetrain was determined using motor curves, and the top speed of the wheels [4]. However, the gear ratio was scaled down to account for the peak efficiency of the motors. In addition to the frame requirement, there were volumetric constraints as there was a common problem of interferences with other subsystems. As a result, a cable suspension system with a sufficient dynamic load rating was used to combat the interference of the main excavation system on other subassemblies [4]. Once the overall design was finalized, each subassembly was evaluated for risks and how they could mitigate them most efficiently. The report then went on to discuss the project methodology by going into detail about why they chose and designed specific parts of the rover based on their analysis.

Testing and analysis are vital for the success of any mission when designing a rover as they can prevent catastrophic failures. For the analysis of the Lunabotics rover, the team began with position analysis, specifically by looking at ground clearance. The team used scale drawings and geometry to determine the rover's clearance, defining the maximum rock radius that the rover needed to clear [4]. The team then focused on the suspension. They determined the dynamic load on the rover and calculated reaction forces on the front and rear wheels using MATLAB, the weight of the rover, and horizontal distances from the center of mass [4]. They conducted Finite Element Analysis (FEA) on their wheels and other structural members to verify that the structure can be supported [4]. Using Ansys simulations, they were able to determine the maximum von-Mises equivalent stresses, an acceptable maximum deformation, and tensile yield strength under varying conditions.

In addition to the traditional 4-wheel skid or rocker bogie drivetrains, two unique designs were found that offered efficiency in their respective missions. The first of which was the WPI two-wheel micro

rover. This rover was constructed with a mass of only 2.7 kilograms and had two carbon fiber wheels with diameters of 29 cm [5]. The two-wheel design features no moving suspension system, but the wheel diameter itself allows for the rover to traverse a step obstacle of 5 cm and round obstacles that are 10 cm [5]. The rover was also designed to survive drops up to 0.25 meters in Earth's gravity, to ensure it could safely drive off a larger rover and deploy to the ground [5]. For stability, extended roll bars bolted on the outer side of each wheel prevent the rover from tipping over sideways, and a trailing tail attached to the chassis prevents the rover from tipping backward during forward acceleration [5]. The wheels extend beyond the body of the rover in every direction, and because of this, the wheels will always remain on the ground at any orientation. The two wheels are driven independently by two motors with a 66:1 gearbox and create a center of mass located below the axis of rotation of the wheels on the main chassis [5].

This MQP team used the Finite Element Analysis tool in SolidWorks to simulate both radial and axial loads on the wheels. The analysis verified the strength of the lightweight wheel design, both in normal operation scenarios and in the case of a sharp impact. The benefits of this design are the simplicity and stability of the rover, but the two-wheel design lacks any redundancy should a motor, motor driver, or wheel fail. Overall, the two-wheel concept is an attractive design option for its simplicity, minimal moving parts, and ability to self-right from almost any orientation.

The last design taken into consideration was SpaceBok's quadrupedal hopping robot. The legs of the robot were constructed using a four-bar mechanism with two actuated links rotating about the same point on the hip of the robot [6]. The legs have two degrees of freedom to allow for both walking and jumping motions, and the lengths of the linkage elements were optimized to maximize jump height [6]. By mounting both motors concentrically on the hip of the robot, the mass of the legs can be minimized. The total mass of the robot was 20 kilograms and can hop 600 mm and trot at a pace of 1 m/s in Earth's gravity [6].

2.3 Electronic Design, Power, and Imaging Research

Any rover that is designed to be deployed in the permanently shaded regions (PSRs) of the lunar polar craters will require a power source that functions independently of solar power. One such power system utilized in the Virginia Tech rover's design was a Radioisotope Thermoelectric Generator (RTG), which

used the heat of decaying Pu-238 to generate electricity [2]. The RTG charged two 28 Volt lithium-ion batteries that were responsible for powering the instruments, motors, and other electronic systems onboard [2]. The electronic system itself consisted of multiple stages. One stage was developed to protect the mechanical components of the rover from lunar dust, while another allows data to be processed and communicated from on-board computers [2]. The rover was also designed with a 6-phase software structure for operation while grounded on the moon. These include the idle phase, routing phase, traverse phase, and sample collection phases, the last of which begins after driving for 10 m [2]. Assuming no mission failure, it was estimated that the rover would traverse the crater in 345 days.

While RTGs are a desirable power source for many space missions, it's their large size, mass, and regulatory restrictions on nuclear material that prevents RTGs from being a feasible power source for many missions. Instead, interest has increasingly turned towards far-field wireless power transmission [2]. This power transmission system relies on one or multiple power stations placed on the rim of a crater that directs a laser beam toward a collector placed on the rover. The rover is then either continuously powered by the laser beam, or the laser beam charges a battery to allow the rover to operate independently for some time [7].

NASA's Space Technology Mission Directorate (STMD) has identified "Sustainable power in extreme lunar surface environments" as a key technology challenge for future exploration and has organized several technology competitions involving beam power transmission as part of the Centennial Challenges [8]. Demonstrations from these challenges have shown that a well-collimated laser beam can continuously provide power at the kilometer scale. Other laser tracking designs have targeted a rover with centimeter-order accuracy to 15 km distances, which allows for deeper exploration of lunar crater PSRs.

In addition to power concerns in PSRs, there also arose the concern of how the rover itself would be able to traverse the environment autonomously or manually operated. The micro rover MoonRanger is fully autonomous as mentioned and relies on onboard sensors and cameras to generate navigation maps of the Lunar surface to travel. Because some areas on the lunar pole surface are permanently shadowed or have little to no light present, lasers and cameras were used to digitally reconstruct the micro rover's environment [9]. Light striping reconstruction has been known since the 1970s and only requires one

planar light strip fixed relative to a monocular camera [9]. The camera reads the light strip by analyzing the image captured from the light by running it through an algorithm that generates 3D points along the light strip about the camera's position. An inertial measurement unit (IMU) was developed to convert the camera reference images and interrupt them into a real-world reference. The IMU operates through a Kalman Filter that fuses the data collected by the 3D points, accelerometers, and gyroscopes to predict the current vehicle trajectory by making a series of generated 3D meshes of the environment [9]. The autonomy software of the micro rover would create a trajectory based on what environmental meshes were generated. The algorithm was also designed to periodically correct the vehicle kinematics and account for the gravitational differences in sensor data on the Moon [9]. After deployment on the Moon, MoonRanger would commence a 3 Trek procedure. The 1st Trek would be to the edge of the designated Communication Zone to allow system diagnostics by mission control. The 2nd Trek tested the connectivity of the rover by leaving the Communication Zone and then reentering, with the 3rd Trek being the mission objective of exploration [9].

Regardless of the selected electrical system components, onboard electronics may also be exposed to radiation from galactic cosmic rays (GCR). The GCRs may not only cause permanent damage to components but also damage any sensor readings and data used by the devices. According to [8], there would be an annual exposure by GCR equivalent to 380-110 mSv or 38-11 krad/yr on the lunar surface as a device would fail catastrophically at doses between 35-18 krad due to degradation [10]. This signifies that on average the devices would fail from radiation in less than one year of operation. Furthermore, electronics also experience the hazard of the buildup of electrical charges in components due to the properties of lunar regolith which is abrasive and conductive [10]. This build-up may cause damage to sensitive lenses and electronics that may be exposed. In contrast, radiation can be mitigated by the presence of lead and aluminum reflective surfaces as well as redundant systems that can correct each other in the case of failure [12]. Lastly, the electrical charge buildup can be mitigated with an indium tin oxide coating which will release the buildup over time [13].

It is worth noting that alternative wireless power transmission solutions, particularly microwave radiation, experience higher efficiency in almost every area of energy conversion. Microwave sources have an electrical-to-optical conversion efficiency typically around 85%, while near-infrared lasers have an equivalent efficiency of approximately 67%. Additionally, microwave receivers have

efficiencies ranging from 80-90%, while photovoltaic converter efficiency lies around 50% [10]. Despite their decreased comparative efficiency, laser implementations remain considerably simpler due to the beam wavelength being on the order of 1000s of times shorter. Therefore, they can produce a smaller corresponding spot size while allowing for a more compact receiver. As well, the photovoltaic cell used to receive the laser beam can also be utilized as a traditional solar panel, if necessary, provided of course the rover exits a PSR of the Moon [10].

2.4 Thermal Design Research

The Lunar polar environment possesses many unique hazards that may render a rover's electronics inoperable during missions utilizing terrestrial vehicles. For instance, the lunar craters that are characteristic of the polar regions of the Moon are known to be fully cast in shadows which causes a great drop in temperature, sometimes up to -250° C (25 K) as shown in the Shackleton Crater [1]. This temperature range would render most electronics functionless. Furthermore, the regions that are exposed to solar radiation experience temperatures that fluctuate between 120° C (400 K) during the day and -130° C (140 K) at night [1]. These thermal fluctuations can cause strain from material expansion and contraction leading to failure that renders the rovers inoperable, as many materials show signs of brittleness due to frigid temperatures. The Virginia Tech rover was exposed to these conditions, and its design featured an active thermal control system consisting of temperature sensors and a heat pump loop. The excess heat from the RTG was relocated to the isolated box containing the control and navigation electronics to keep on board systems operational [2].

Similar environmental conditions were present when looking at the MoonRanger mission. The micro rover would be exposed to temperature ranges of 50 K to 300 K [3] in addition to difficult lunar terrain. It was determined that the margin of operation for the sensors and components under these conditions was -10°C to 35°C [3]. To maintain system components and operations, a combination of both an active and passive thermal heating system was implemented. The active thermal solution would be a small heater placed near vital sensors and components that would activate for a short period to bring the sensor back to the designated temperature threshold [3]. These automated heaters were in every internal avionics component, wheel motor, external laser, and sun sensor to provide the necessary heat as mentioned. The passive thermal solution primarily came from a solar panel that was built on top of the micro rover's chassis where heat was generated from the sunlight gathered [3]. Both solutions were

analyzed through a Thermal Desktop simulation that depicted the entire micro rover's thermal distribution when placed in a frigid environment [3].

Efficient thermal control is essential for the performance and longevity of the rover's internal subsystems. The harsh environmental conditions of the lunar south pole necessitate the employment of both passive and active thermal solutions. Active thermal solutions include design elements that require power to be redirected from other functions to raise the temperature of the system if it reaches temperatures that could risk the rover's functionalities, while passive elements optimize the optical properties of the rover's surface to better maintain these temperatures without expending any additional energy. For instance, industrial-grade semiconductors are rated for operating temperatures between -40 to 85°C which can fall short of both the minimum and maximum temperatures experienced [14]. Therefore, any passive or active heating needs to be able to work within these bounds.

In contrast, radiative heat loss can be mitigated by the presence of lead and aluminum reflective surfaces as well as systems that can correct each other in the case of failure [12]. This process is primarily present with the addition of a solar panel, as mentioned in the MoonRanger design. Solar panels are designed to convert light from the sun or a concentrated laser beam to electric power. By applying a surface finish, the absorptivity and emissivity characteristics of the panel are changed, making it better suited for a cryogenic environment. Additionally, coatings, VDA tape, and localized finishes provide passive heat solutions depending on the component's needs [12]. In general, for the lunar environment to be explored successfully, missions must be equipped with preventative measures for these hazards.

2.5 Mission Plan

This project involves modeling and theoretically launching a payload containing a micro rover and communications module from the Earth to the South Pole of the Moon. In addition to basic orbital mechanics, this mission is modeled using certain features of the Chang'e 5 (2020) and Artemis I (2022) Missions. Provided are the details of all stages of the mission from launch to re-entry/touchdown, including the cislunar transfer, lunar capture/escape orbits, and rover release/recovery rendezvous maneuvers. The mission is split into several phases and treats each one (gravitationally) independently of the others except for basic conic patching, which is significantly more elementary compared to the real-time onboard feedback and control used in the missions. Several Hohmann transfers are typically

used to facilitate orbital changes. A launch window was determined, and total Delta-V and Time-of-Flight minima were estimated. No other parameters are given or constrained, so a mission was devised that keeps Delta-V to a minimum as much as possible. This mission outline and calculations were created referencing the following textbooks: *Orbital Mechanics for Engineering Students* [15], and *Fundamentals of Astrodynamics: Second Edition* [16].

2.5.1 Rocket and Launch Details

Similar to the aforementioned unmanned missions, a multistage rocket was chosen to utilize solid propellant to produce the necessary thrust for launch and subsequent maneuvers. The payload includes the lunar rover (with small thrusters, parachute attachment, and airbags) and a solar-powered communications module satellite. The rocket, rover, and module are capable of minor attitude corrections. The launch takes place at the Kennedy Space Center in Cape Canaveral, FL with a Latitude of 28.5 degrees [15][16]. The launch window and corresponding lead angle correspond to when the Moon reaches its perigee with the Earth, around the *Supermoons* of 2023, that is, August 1st and 31st [15][16]. This launch window was chosen to minimize the travel distance upon rendezvous with the Moon.

2.5.2 Basic Details of Earth Heliocentric Orbit and Lunar Geocentric Orbit

The orbital velocities of the Earth about the Sun and the Moon about the Earth were computed in their respective mildly elliptical orbits. P provided that the orbits Keplerian in nature and under the influence of a body with standard gravitational parameters, we compute the orbital velocity,

$$V(r) = \sqrt{2\left(\varepsilon + \frac{\mu}{r}\right)},$$

at radial distance r (from a body-centered focus) and specific energy $\varepsilon = -\mu/2a$. The Earth and Moon SOI were also determined, which define regions for the mission phases that involve the Moon [15][16]. These are necessary calculations for the method of patched conics that we use to determine lunar capture and escape. We use the result derived in [2], that is,

$$r_{SOI} = a_{pl}\left(\frac{M_{pl}}{M_S}\right)^{\frac{2}{5}}$$

where M_{pl} is the mass of the corresponding planetary body, a_{pl} is the semi-major axis of the planetary body to the Sun, and M_S is the mass of the Sun itself.

Figure 6: Spacecraft Trajectory from Surface of Earth to LEO via the 1st Hohmann Transfer

Surface to LEO (via Hohmann 1)
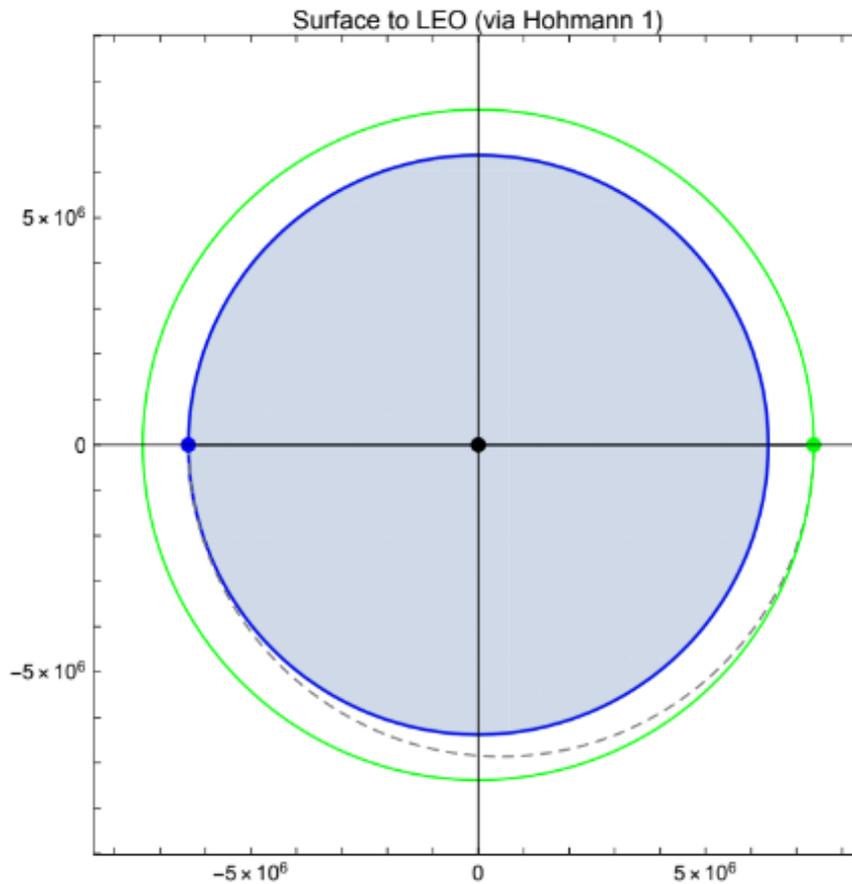
2.5.3 Geocentric Hohmann Transfer 1 (Surface to LEO, Phase I)

This mission implemented a series of Hohmann transfers and other controlled maneuvers (Figure 6). After launching from the Kennedy Space Station, a short Hohmann transfer of eccentricity e was used to place the spacecraft into a Low Earth Orbit (LEO) with an altitude of 1000 km. This is done to launch at the right moment, so the rendezvous occurs at the precise radius of perigee,

$$r_p = a(1 - e)$$

The time of flight for such a maneuver is one-half the transfer ellipse,

$$T = 2\pi \sqrt{\frac{a^3}{\mu}}$$

[15][16].

Figure 7: Spacecraft Trajectory from LEO to Lunar SOI via the 2nd Hohmann Transfer
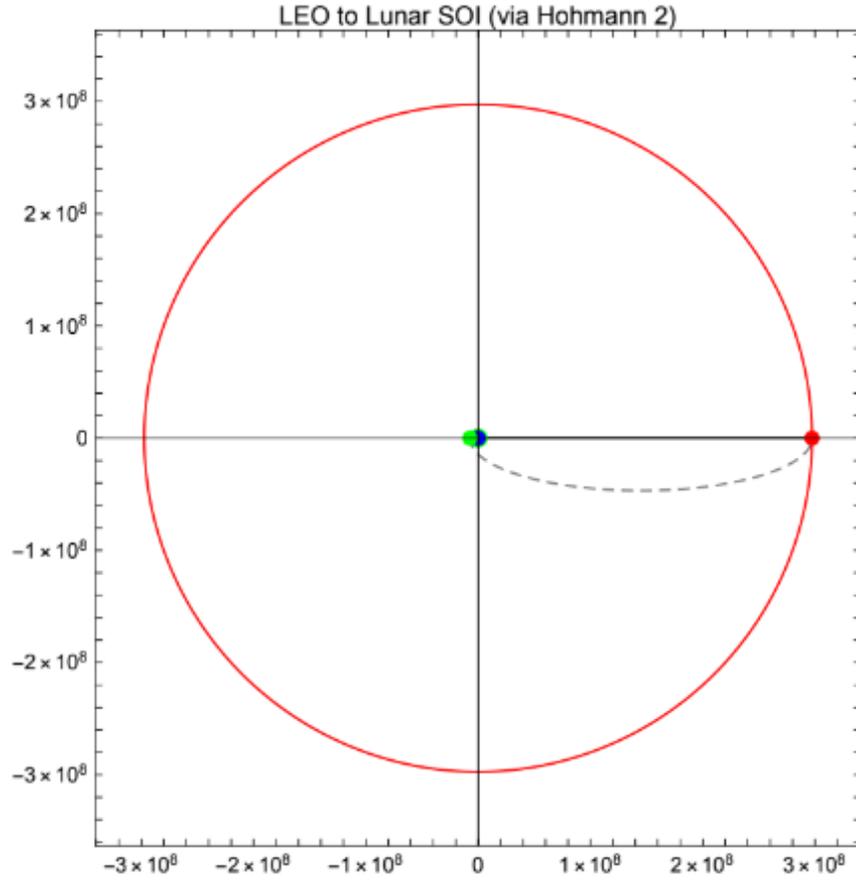
2.5.4 Capture (Lunar SOI to LMO, Phase III)

Upon entering the lunar SOI and performing a plane change, conics from the Hohmann transfer ellipse to a flyby trajectory hyperbola are matched. A burn to slow the spacecraft was then used at the perilune distance of 500 km, which places the spacecraft into a circular lunar capture orbit (LMO) at this altitude [15][16].

Figure 8: Spacecraft Trajectory into Lunar SOI Entry and Lunar Capture into LMO
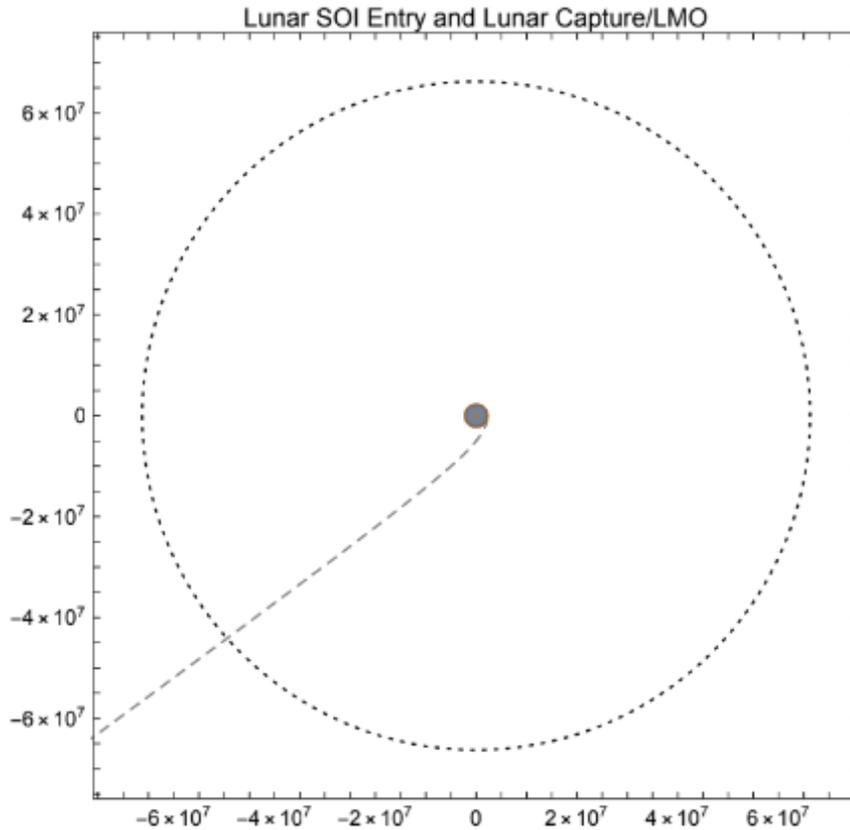
2.5.5 Rover Release (LMO to Low Perilune Orbit, Phase IV)

The spacecraft would remain in a low parking orbit around the moon to eventually make a drop-off of the lunar rover. This resulted in a low perilune orbit (LPO) with an altitude of 25 km to complete this maneuver [15][16]. Essentially this is a Hohmann transfer ellipse, but with no transfer except for the release and recovery of the lunar rover [15][16]. A burn to slow the spacecraft at the north pole of the Moon was used, which places it into a controlled descent from the LMO into the LPO with perilune [15][16]. The lunar rover is then released at the perilune while the communications module remains in the same low perilune orbit (LPO) to monitor and remain at a close physical distance from the drop-off location [15][16].

Figure 9: Spacecraft Trajectory into Lunar Capture/LMO
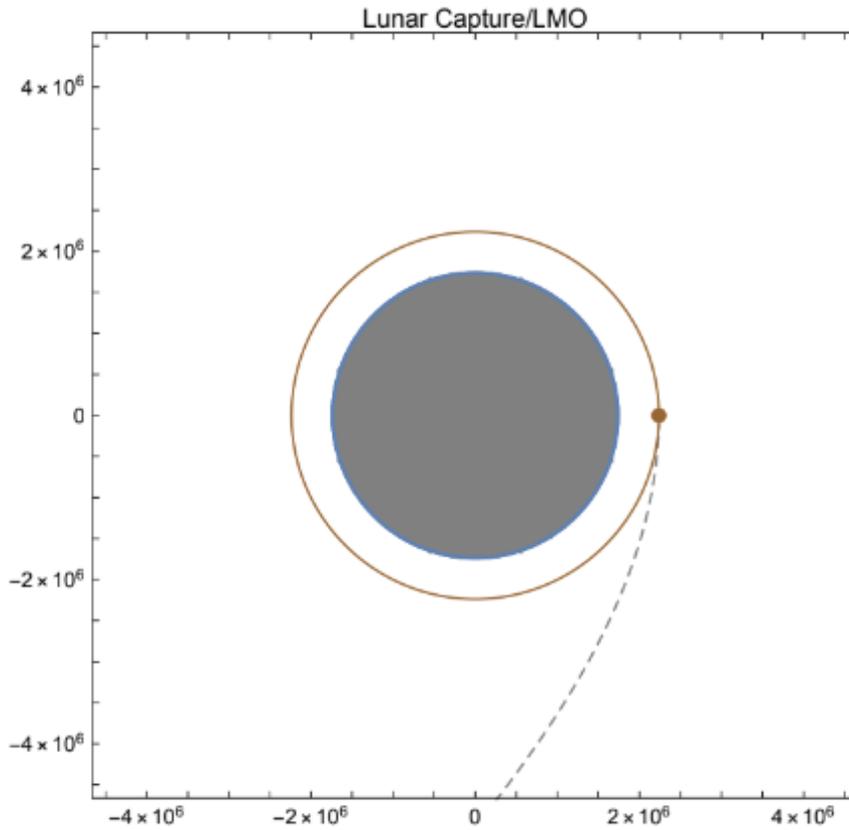
To model the rover release, a ballistic missile drop theory was used. The rover itself uses onboard thrusters and parachutes to enable controlled descent and touch down on the lunar surface [15][16]. At this point, the attention is focused on the lunar rover itself, which may take days, weeks, months, or years to collect data. The rover then sends this data to the communications module at each perilune rendezvous.

Figure 10: Trajectory of LMO to/from Spacecraft Drop-Off Orbit

LMO to/from Drop Off Orbit (Lunar South Pole)
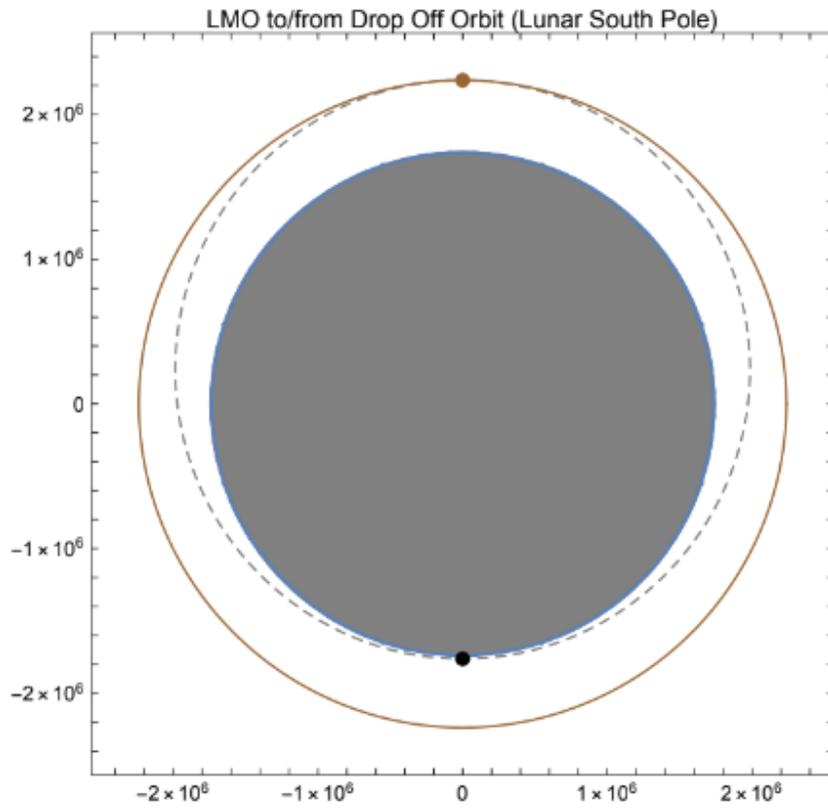
2.5.6 Rover Return (Low Perilune Orbit to LMO, Phase V)

After the rover has conducted all necessary explorations and experiments, it would then return to the communications module. The communications module then retracts the net and encloses the rover.

Figure 11: Spacecraft Exit Trajectory from LMO
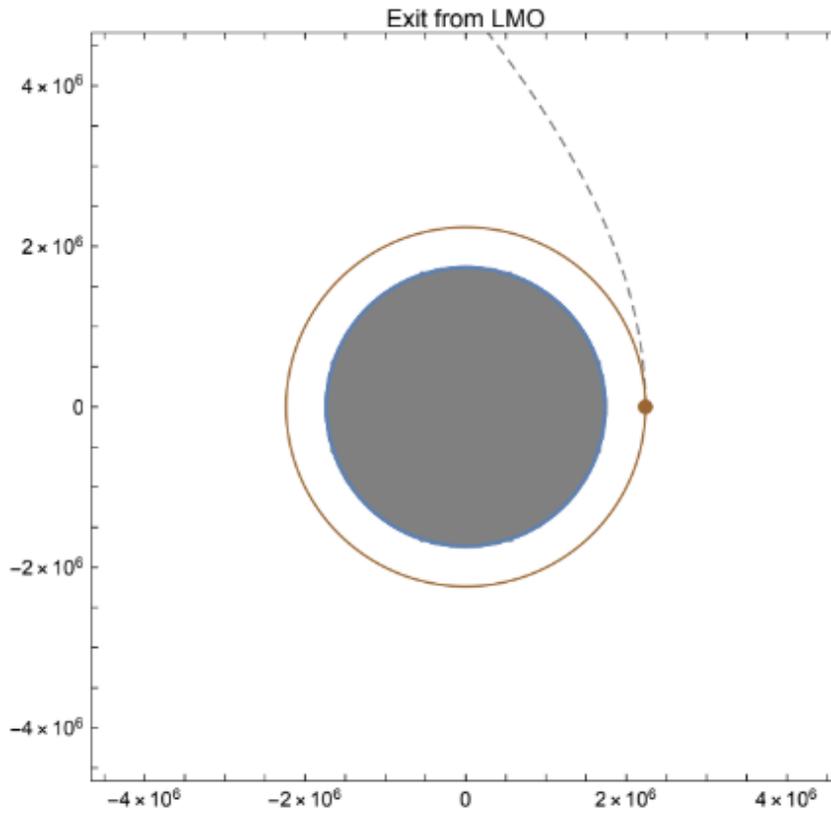
2.5.7 Lunar Escape (LMO to Lunar SOI, Phase VI)

The lunar module with the rover then goes on a trajectory back to Earth. To do so, an escape burn from the apolune toward the edge of the sphere of influence of the Moon is used [15][16].

Figure 12: Spacecraft Trajectory from LMO to Lunar SOI Exit

LMO to Lunar SOI Exit
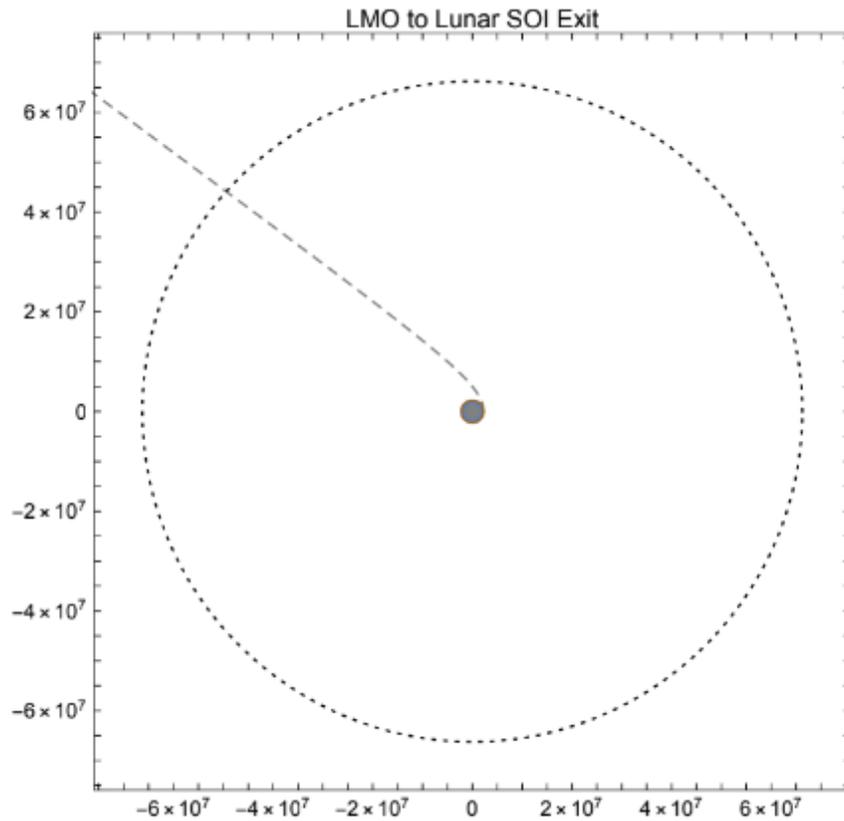
2.5.8 Geocentric Hohmann Transfer 3 (Lunar SOI to LEO, Phase VII)

Once the spacecraft has reached the necessary distance at the edge of the lunar SOI, conics are matched, and a plane change is performed to a return cislunar Hohman transfer along the ecliptic plane toward Earth [15][16].

Figure 13: Spacecraft Trajectory from Moon SOI to LEO via the 3rd Hohmann Transfer
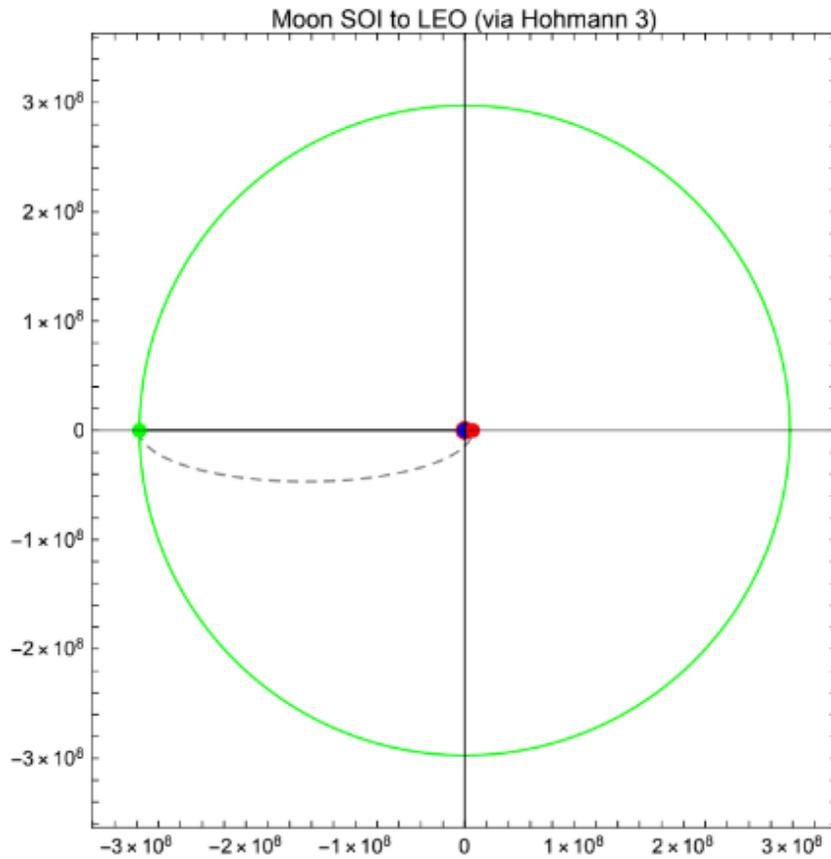
2.5.9 Earth Capture plus Inclination Change and Reentry (LEO to Surface, Phase VIII)

When the spacecraft has arrived at the LEO altitude, a burn is performed to put the spacecraft into a capture orbit about the Earth. Depending on the time, simultaneously it begins the descent toward the Atlantic Ocean 1 mile off the coast of FL nearest the launch site of the Kennedy Space Center [15][16].

Figure 14: Spacecraft Trajectory from LEO to Surface via 4th Hohmann Transfer

LEO to Surface (via Hohmann 4)
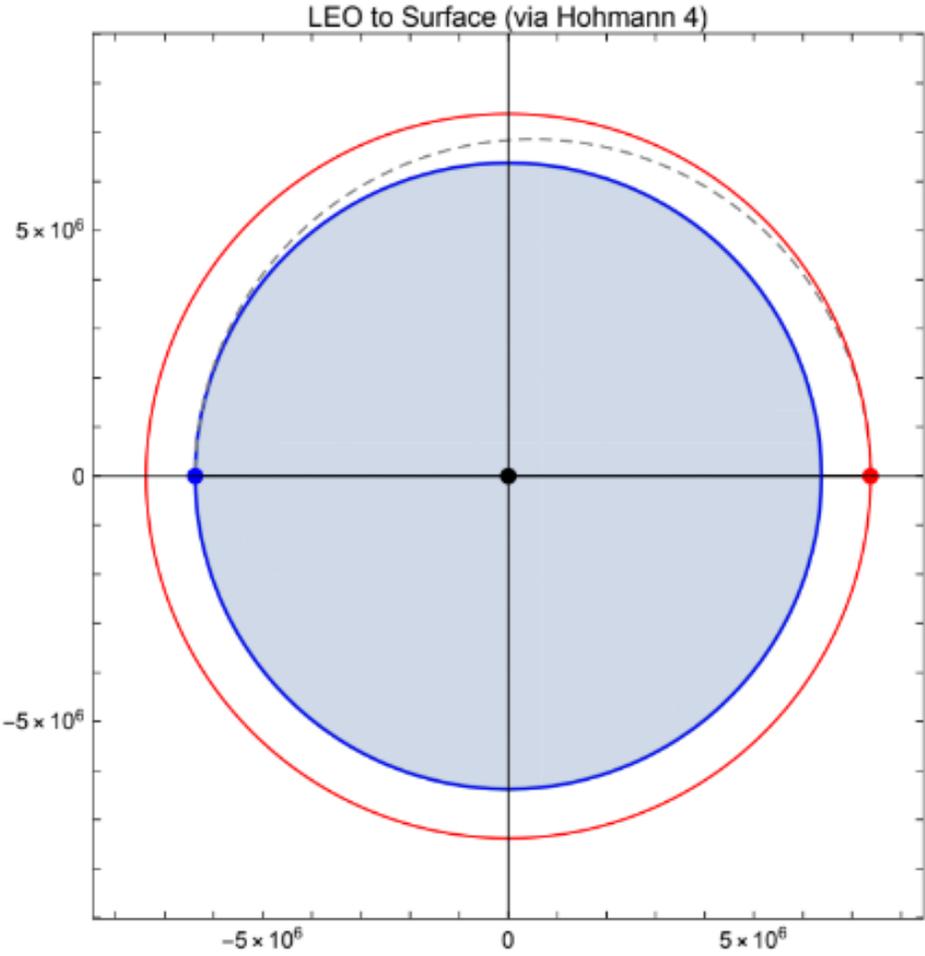
3. Methodology

3.1 Figures of Merit

It was decided by the team that the project would be approached by dividing into two sub-teams, mechanical and electrical, to facilitate simultaneous work on both aspects of the rover. By doing so, the completion of the project within the short timeframe was more manageable.

The mass budget was determined to be the primary consideration by the mechanical sub-team. The initial project requirements dictate the rover weighs no more than 5 kilograms. Thus, the materials used for the rover's structure had to be both lightweight and maintain strength at cryogenic temperatures. Before the design phase, multiple points of failure within the micro rover were determined as a critical features. These features were designed with redundancy in consideration wherever possible. Such redundancy ensures that all critical features can function correctly under typical operating conditions.

The primary goals of the electrical sub-team were to reduce the subsystem mass and power consumption of the hardware. Lower mass reduces necessary motor torque and therefore motor size, and minimizing power consumption extends operation time when operating independently from power transmission. For the software, the main goal was to develop modular autonomous navigation functions. Secondary important considerations for both software and hardware were in-situ hazard recognition, scientific data collection, and shielding dust ingress.

3.1.1 Mechanical Considerations

The mechanical sub-team focused on the research of relevant projects to give guidance and structure to how the design process was to be completed. This gave the sub-team a base of knowledge that would help create a more successful design made possible by the trade space. The mechanical team used the literature review, past rover designs, current research, and industry standards to aid in the decisions made throughout the project. These together helped in the final design and decisions that were made.

3.1.2 Electrical Considerations

The approach used in the initial quarter of the project term was largely research-based. Heavy emphasis was put on this portion of the project due to the limited time and budget. The research needed to be high quality and explored thoroughly for the team to decide on the best-fitting attributes for the rover. This was ideally the goal of the literature review, to access and study the assorted designs other engineering teams created to fulfill a similar task: to create a working scientific rover able to withstand the Moon's polar terrain and its dangerously low temperatures. It consisted of a blend of different approaches, all of which could be applied to this project. It all included studying aspects of both the detailed mission plans and rover features, which assisted in the creation of the preliminary design later in the term. To gather more sources on the variability of the different materials and components the team wanted to use in the design, databases such as those found on WPI's Gordon Library aided in the search.

From the literature review, it was identified that any electrical components on the rover would need to meet certain criteria. Materials would have to be durable, for the rover was meant to operate independently for extended durations in a harsh environment. Weight was also a concern, though not prioritized as highly as durability. The sub-team agreed that even the lightest component would become unnecessary weight if it did cease to function. It was also determined that methods involving a Global Positioning System (GPS) were a viable option. This decision was made with the assumption that similar radio-navigation systems will be present on the Moon in the future, whether this be through satellites or triangulation from base stations located on a crater rim. With rough criteria in place, the sub-team settled on three potential methods for autonomous navigation.

The first method identified was a combination of a 360º Light Detection and Ranging (LiDAR) system paired with GPS for mapping and localization of the rover. The LiDAR would be able to detect variations in the rover's immediate vicinity while the GPS would allow both mission control and the rover itself to estimate its position. The primary benefit of this option was the ease of mapping the lunar surface and processing that data using LiDAR-based systems. However, the downside came in the form of cost. Were this method to prove ineffective, there would not have been sufficient funding for a replacement option.

The second option discussed was using a camera programmed with hazard recognition software to identify local hazards while maintaining GPS as the method of location on the lunar surface. This option's primary benefit is cost. The downside was the software that would have to be developed for close-range hazard recognition. This option was eventually selected as the primary option.

The third option that was considered was supplying the rover with a pre-generated point cloud while continuing to provide locational data to mission control via GPS. This option was by far the simplest, with the slight issue of providing the pre-generated point cloud. As the desired rover was meant to be exploratory, sending a manually controlled rover to map an area before sending an autonomous rover to the same area was determined to be impractical. Furthermore, were any changes to the lunar surface to occur between the map generation and the map implementation, the rover would find itself unable to course correct in any way as it would not have a means of observing its environment.

3.2 Mechanical

The team elected to use 6061 aluminum for the material of all manufactured components on the micro rover. 6061 aluminum is a proven material, as it has been used in the aerospace industry extensively and featured in past rover designs. For the design of the micro rover, the first question was how many wheels would be most conducive to our mission constraints. To do this the team created a decision matrix where seven different wheel configurations were weighed against each other: hopper, 2-wheel, 4-wheel, 5-wheel, 6-wheel rocker bogie, 6-wheel articulated, and tank treads. Comparing the complexity, max obstacle size, redundancy, stability, feasibility, and power requirements. This narrowed the decision down to three options the 2-wheel, 4-wheel, or 5-wheel.

Figure 15: A decision matrix depicting the feasibility of wheel designs through numerical ranking.

Number of Wheels	Hopper	2	4	5	6 (Rocker-Bogie)	6 (Articulated)	Tank Treads
Steering Complexity	10	0	0	0	4	6	3
Suspension Complexity	10	2	5	6	8	10	10
Max Obstacle size	4	0.37	0.75	1.5	2	2.5	1.5
Size Score	4	1.85	1.5	2.5	1.666666667	1.5625	1.15385
Redunecy	1	1	6	6	10	10	3
Stabilty	3	10	5	6	8	7	6
Feasibility	1	10	8	7	5	4	2
Power requirements	1	5	5	5	5	8	10
Total Score	27	55.4	38	41	35.66666667	27.25	15.6154

Rough models were then created in SolidWorks of the three designs to get a weight estimate. This would help in the sizing of the initial design. From this, it was determined that the 5-wheel design, while providing more stability, added unnecessary weight from the extra wheel compared to the others. The 4-wheel rover was therefore selected as our final design, as it provided enough stability while also offering a much greater maximum obstacle size compared to the 2-wheel design.

Once the number of wheels was selected, the drivetrain could then be considered. For the micro rover's mission, the drivetrain must be redundant to prevent failures as it moves on the lunar regolith. Rather than having one motor that drives all the wheels, each wheel will have a separate motor that drives it. This allows for one or two motors to fail before the rover becomes inoperable compared to a single point of failure if relying on a singular motor. The suspension system was the last part that was looked at by the team. A 4-wheel rocker suspension was selected as it offered flexibility and the ability to climb obstacles. The CAD models for all iterations of the structural components were generated in

SolidWorks. Many of the parts that were used were off the shelf from McMaster-Carr, and these parts had existing 3D models that were downloaded from the McMaster-Carr website.

The initial CAD model for each structural component and the full assembly of the various components for the rover was created in SolidWorks. They then were imported into Ansys Explicit Dynamics for a numerical drop test simulation to estimate impact accelerations. This simulated dropping the rover from 4 inches in Earth's gravity with initial acceleration, equivalent to a 24-inch drop in the Moon's gravity. The impact data from that was then used to run static simulations on subassembly. Then an iterative process was followed, going back and forth between Ansys to test the strength and SolidWorks to redesign the part to be weaker and lighter where possible and strengthen it where needed. This process is discussed in more detail in section 5. Traction tests were not able to be completed in Ansys, so preliminary testing was done with modified 3D-printed wheels. Three different designs for treads and 3 different depths for each tread type were tested.

HAAS mini mills were used in tandem with the computer-aided manufacturing (CAM) software ESPRIT to fabricate the rover. By importing the models created in SolidWorks to ESPRIT, the proper toolpaths and the NC code were created. Some of the contours, weight reduction cuts, threads, and through holes that were modeled in SolidWorks were not able to be cut by the mills due to how the parts needed to be mounted into the machine. These cuts and contours were either done on a bandsaw or skipped over due to how complicated they were to execute. The through holes for screws in the motor mounts were hand drilled because the bit size needed was not an option on the mill. The treads for the screws were hand tapped to make sure that they went to the proper depth.

3.3 Electrical
3.3.1 Hardware Component Selection

For the selection of the rover's electronic components, three figures of merit were prioritized. The primary figure of merit was choosing the lightest possible components that could suffice for the needs of the project. This merit weighed heavily since most of the weight budget would be taken up by mechanical components thus leaving little room to work with electrical components. While this merit did not affect most aspects, it came into account when looking for an appropriate battery to use for the micro rover since this was by far the heaviest electronic component, with the lightest option being 800

28

grams. The second merit was to reduce power usage as possible to prolong the operation time of the micro rover. For this purpose, a high-capacity battery was chosen with low operating voltage components. Lastly, components that are resistive to the hazardous lunar environments were selected, with both minimum operating temperature and risk of radiation exposure being considered. These components were small enough to be encased within the inner housing of the rover.

Considering these figures of merit, the micro rover drive motors were sized by calculating a worst-case torque requirement. When selecting a motor, it needed to provide a large factor of safety for this torque scenario. The estimated required force produced by each motor is a sum of three components: the rolling resistance force required to move the rover from zero velocity, the force required to drive the rover up a hill of 30 degrees, and the force required to accelerate the rover up to its design velocity of 0.1 m/s^2 over 5 seconds. These values were calculated as follows:

$$F_{rr} = M_{rover} \cdot \mu_{sand} \cdot g = 5kg \cdot 0.3 \cdot 9.8 = 14.7 \text{ N}$$

$$F_{slope} = M_{rover} \cdot g \cdot sin(\theta) = 5 \cdot 9.8 \cdot sin(30°) = 24.5N$$

$$F_{accel} = M_{rover} \cdot \frac{V_{rover}}{t_{accel}} = 5kg \cdot \frac{0.1}{5} = 0.1N$$

Therefore, the total force to drive the rover on Earth should be 29.3 N, or 7.3 N per wheel. Given a wheel radius of 0.13 m, each motor must provide 0.949 N-m of torque. A safety factor greater than 2 was desired to account for variation in lunar regolith friction coefficients and to provide redundancy. From this information, the Pololu 20D gear motor with a 488:1 gear ratio was selected. This motor provides 2.45 N-m of torque at stall current, giving a maximum factor of safety of 2.58, which allows the motors to operate well below stall torque in normal operation.

After the motors were selected, the process of choosing sensors and components necessary for the mission operations began. Due to the exploratory nature of the mission, two aspects of the sensors were considered: scientific data collection and pathfinding data. Based on this, a camera module that would be used for hazard recognition was selected, as well as a 9 Degree of freedom IMU, motor encoders, and GPS receiver utilized for pathfinding purposes. These sensors would be sufficient to traverse the lunar polar regions and avoid any threats it may encounter along the way, while the camera provides basic scientific data potential.

Based on environmental factors, specific types of sensors were refrained from. For instance, a LIDAR sensor was eliminated as a possible action because the unevenness of the lunar surface as well as the reflectiveness of regolith would obscure sensor readings. Furthermore, pressure sensors were refrained from since approaching an object to that extent could be hazardous to the rover.

The specifications and effectiveness of each component were researched to determine which microcontroller module could handle the processing power required to do state estimation calculations as well as Kalman filtering. For this purpose, several primary factors needed to be considered such as the processing power, memory, and input/output (I/O) capabilities of the microcontroller. All these factors determined whether the microcontroller could handle the raw data flow for all the sensors. Additionally, alternative factors such as cost, power consumption, ease of use, and thermal resistance of the microcontroller were considered to optimize the best choice. Based on these results two families of microcontrollers were selected, the Raspberry Pi and Arduino, because in conjunction they fit all the micro rover's processing needs. Within these families, the Arduino Mega 2560 Rev3 was chosen due to its low min temperature, low power consumption, and plenty of I/O to gather all the data and handle motor controls while a Raspberry Pi 4 was used for Kalman filter calculations.

Table 1: A table showing the design specifications of electrical components selected for the micro rover.

Function:	Model:	Quantity:	Cost:	Size:	Weight:
Camera	C1-PRO	1	$139.00	40x40x23 mm	53 g
Microcontroller	Arduino Mega	1	$24.90	101.52x55.3 mm	37g
	Raspberry Pi 4	1	$112	88X58X19.5 mm	46g
Battery	11.1V 10000mAh Lithium-Polymer Battery Pack	1	$62.99	170x61x32 ±2 mm	647 ±5 g
Motor	Pololu 20D Gearmotors	4	$29.95	20x20x46 mm	45 ±5 g
Encoder	Pololu Encoders for	2	$8.95	20x16.5x3 mm	2.4 g

	Micro Metal Gearmotors				
Controller	Romeo BLE	1	$39.50	98x80mm	

3.4 Software

3.4.1 Path Planning Approach

Operating under an assumed threat field cost function that represents a risk of traversing terrain near obstacles, a path planning algorithm needed to be developed to allow the rover to plan a trajectory from its current location to a goal end position. Commonly used path planning algorithms typically fall into two categories: grid-based search algorithms and sampling-based search algorithms [17]. Grid-based algorithms overlay a discrete array of points onto the navigation space and assign a cost for traversing between any two valid points. Movement between points is typically considered valid if the two points are adjacent horizontally, vertically, and often diagonally, and these connections are vertices on the graph. This allows a path to be constructed as a sequence of movements along connected vertices from a start to an endpoint [17]. Grid-based algorithms present a tradeoff: sparser grids are computationally faster but may fail to solve in the presence of narrow spaces between objects. Conversely, creating a dense enough grid to navigate a crowded space can result in significantly longer computation times. Additionally, the discrete nature of the grid presents a lot of short path segments with many turning points between them, although this can be mitigated using additional smoothing algorithms. Examples of grid-based search algorithms commonly used include Dijkstra's algorithm and A*.

Sampling-based algorithms instead attempt to connect the start and goal positions by randomly sampling points in the navigation space and connecting them in a tree structure [18]. Nodes of the tree are randomly placed in non-obstructed positions and are connected to the existing tree structure using one of a variety of nearest-neighbor algorithms. The tree is continuously expanded until a node is generated in the goal region. Although these algorithms alone do not produce optimal paths, modifications are possible to allow them to approach optimality given infinite execution time. Practically, these modified algorithms converge to a pseudo-optimal solution in a finite time, though typically more slowly than grid-search algorithms execute [19]. The optimal variants introduce a cost function over the navigation space and calculate the cost of connections between nodes. When connecting a new node, the lowest-cost neighbor is connected. When creating new nodes, the nearest neighbors are also examined to see if they can be connected to the new node, and if this would decrease

the cost, the tree is rewired to connect through the new node. This tends to make the path smoother as nodes are added to the tree and decreases the total cost of the final path, pushing it closer to optimality. Optimized sampling-based algorithms tend to produce smoother paths than grid-search algorithms, with longer path lengths between turning points. This becomes advantageous when exploring large, open navigation spaces [19]. Examples of these types of algorithms include Rapidly Exploring Random Trees (RRT) planning, RRT* (the optimized variant), and Probabilistic RoadMap (PRM) planning. Given the open, relatively unconstrained nature of the lunar surface environment, the relatively long and straight path lengths, and the lack of a real-time path planning requirement, the RRT* planning algorithm was selected for the rover.

3.4.2 Hazard Detection Considerations

Given that implementing a SLAM algorithm with a monocular camera was infeasible for this project, it was decided that the rover would operate under a known map. This map would be represented by a threat field, which spans the navigation space and assigns a scalar cost to traversing any given location. This threat field could represent a cost function generated through a SLAM map and would provide an easy way to expand autonomy to include SLAM in the future. Even though the rover operates under a predetermined threat field, it was desired to provide a method to detect unmapped or dynamic threats in real-time onboard the rover. To accomplish this, two methods were considered. The first approach would use an additional LIDAR sensor to generate a point cloud of the area immediately surrounding the rover. Software analysis of this point cloud could identify potential obstacles and provide exact size and distance information about them. The second approach would use the existing scientific camera, utilizing computer vision algorithms to identify the contours of objects in front of the rover.

The LIDAR approach was quickly rejected, primarily due to weight and cost concerns. Although the precision and certainty of LIDAR data are highly desirable, rover navigation requires the detection of negative space obstacles such as craters or holes. This would necessitate articulating the LIDAR scanner up and down, requiring the addition of a servo motor to allow for scanning. This assembly would add on the order of hundreds of grams of mass to the total rover assembly, contrary to the design goal of minimizing mass. Additionally, the cost of materials and manufacturing such a scanning assembly were outside of the electronics budget, eliminating this as a choice for hazard detection.

Conversely, the computer vision approach utilizes existing hardware on the rover and requires only additional software development to implement the OpenCV library. The lunar environment is also conducive to high-quality contour detection. Given the functional lack of a lunar atmosphere, Rayleigh scattering of light does not occur, which results in very dark and defined shadows. These sharp shadows significantly improve the efficacy of contour detection and allow a high degree of accuracy in detecting objects given a relatively low-fidelity engineering camera. Even without distance measurement from LIDAR, the size of and distance to the object can be estimated by comparing data from different video frames over time. Because of the mechanical and electronic simplicity of this implementation, contour detection was selected as the primary dynamic hazard recognition approach.

4. Design and Integration

4.1 Mechanical Components

4.1.1 Design Overview

The selected rover design features a four-wheel 'rocker' suspension system. This system features two rockers, which connect to the middle of the rover chassis and split into two legs, each leg housing one wheel. Each rocker is free to rotate relative to the chassis, and a differential linkage system connects the rockers in such a way that one rocker must rotate in the opposite direction as the other. This linkage also allows the four wheels to individually traverse uneven ground, while the chassis remains at the average angle of the two rockers.

Figure 16: A view of the full micro rover assembly within Solidworks.
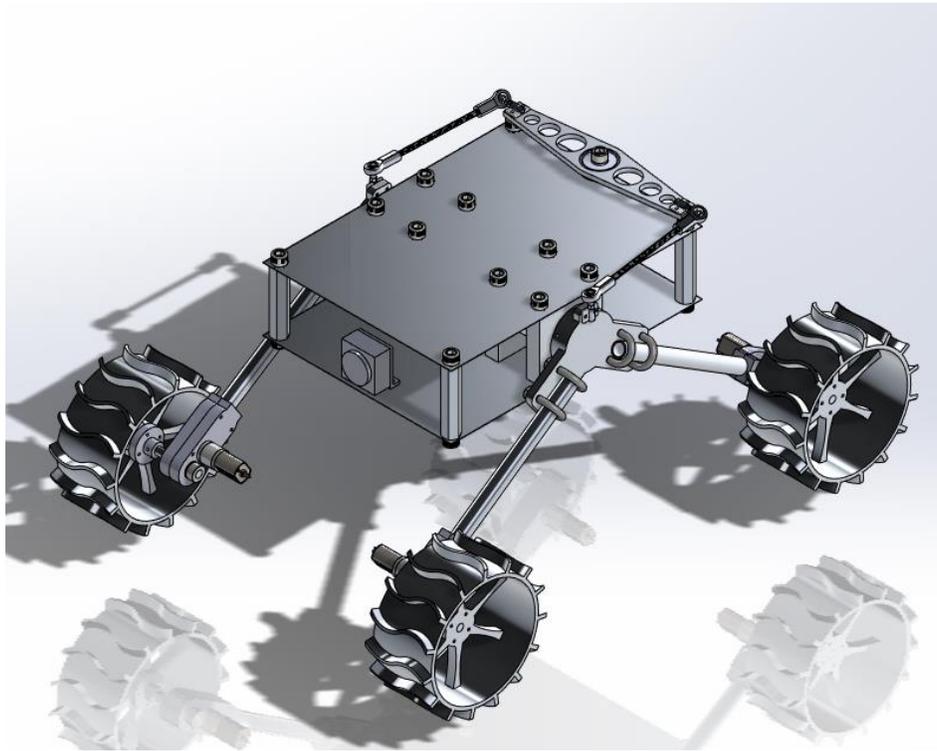
4.1.2 Chassis

The chassis needed to have enough volume to house the electronics, be able to support the weight of the solar panel, and provide pivot points for the two rockers and the differential linkage. The design features a rectangular prism with four ball bearings fixed in blocks to allow the rocker axles to rotate freely. The four blocks also provide rigidity to the structure, allowing the chassis to support the weight of the battery and control electronics.

Figure 17: An isometric view of the micro rover's chassis interior CAD model.
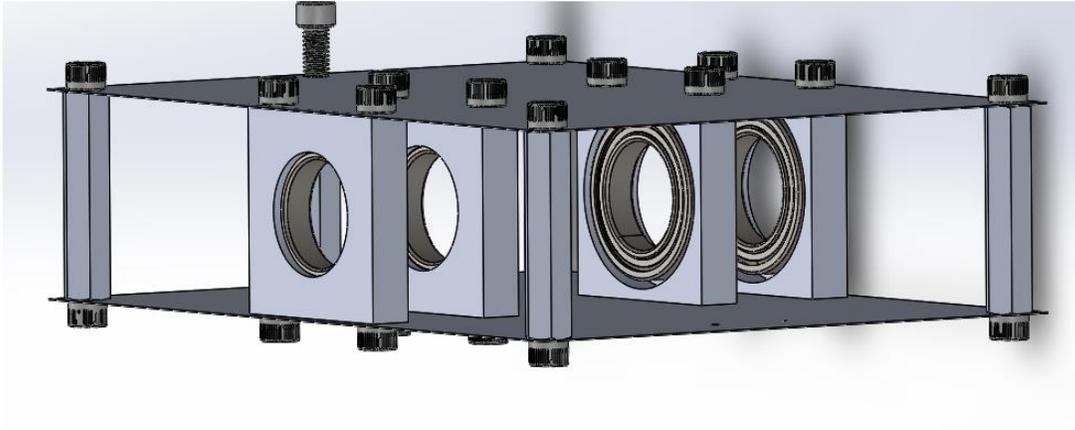
The chassis was also constructed out of five 3-inch-tall hexagonal standoffs, one in each corner and then one in the middle of the rear side of the rover. The center-rear standoff provides a rigid pivot point for the differential pivot link.

4.1.3 Wheel-Leg Assembly

The rockers on either side of the rover attach to the blocks in the chassis via two axles supported by ball bearings. At the end of each axle, a mounting plate was used to connect the two legs and the differential linkage. The axles were chosen to be hollow tubes with a large inside diameter. This allowed larger holes to be cut out of the supporting blocks, reducing weight while increasing the strength of the axles and reducing the forces on the joint between the axles and the leg-mounting plates.

Figure 18: An isometric view of the micro rover's Wheel – Leg CAD assembly that attaches the wheels and motors to the chassis.
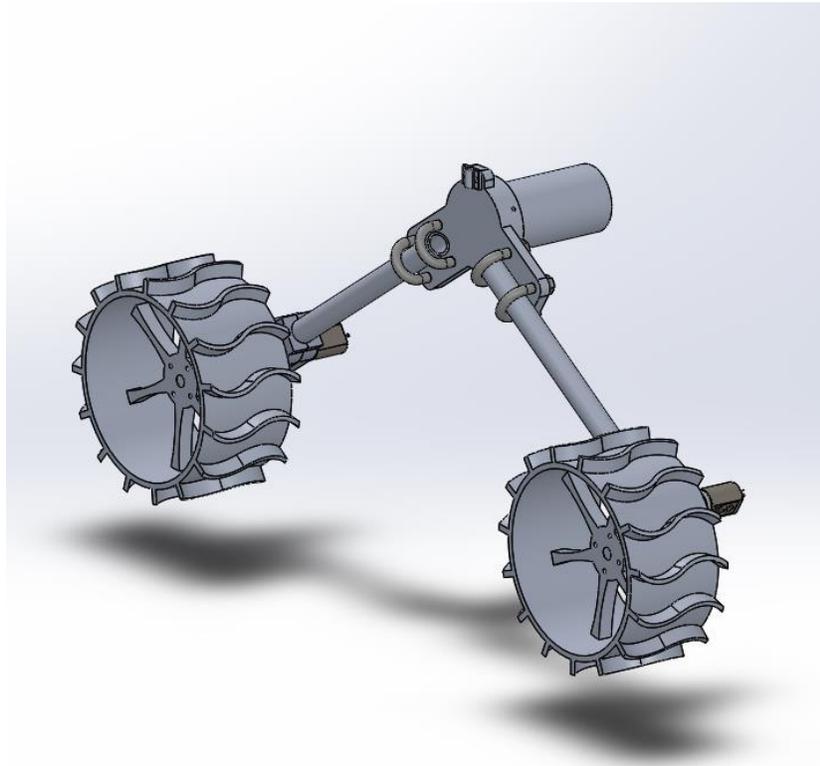
A motor mount assembly connects to the end of each leg. The motor mount held the motor as well as a gearbox that connected the motor to the wheel axle, rather than having the wheels directly on the motor shaft. This allows the weight of the rover to rest directly on the wheel axles and the wheels rather than on the relatively fragile motors. The motor mount assembly is held together by four M3 bolts running through the assembly.

Figure 19: A view inside the micro rover's motor mount CAD with its gearbox attached to the motor.
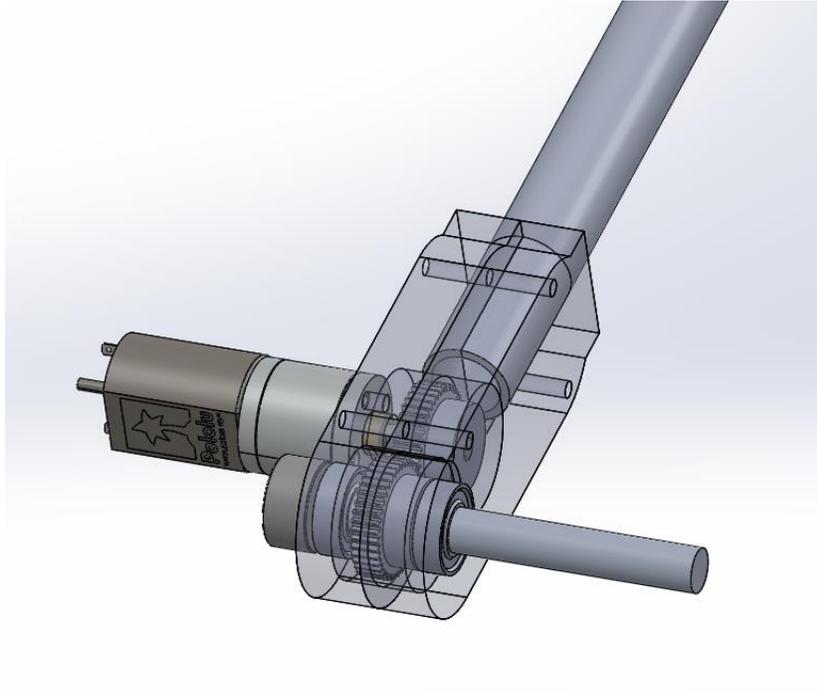
4.1.4 Pivot

The differential linkage is made up of a differential link at the rear, with two connecting rods that connect the differential link to each rocker. Each link in the linkage is connected via a ball-joint link, to allow the rockers and the differential link to rotate about a perpendicular axis. The differential link is connected to the chassis via a ball bearing bolted to a standoff. Holes are cut out of the pivot link to reduce weight.

Figure 20: A view of the pivoting system that acts as the suspension system for the left and right micro rover Wheel-Leg CAD assemblies.
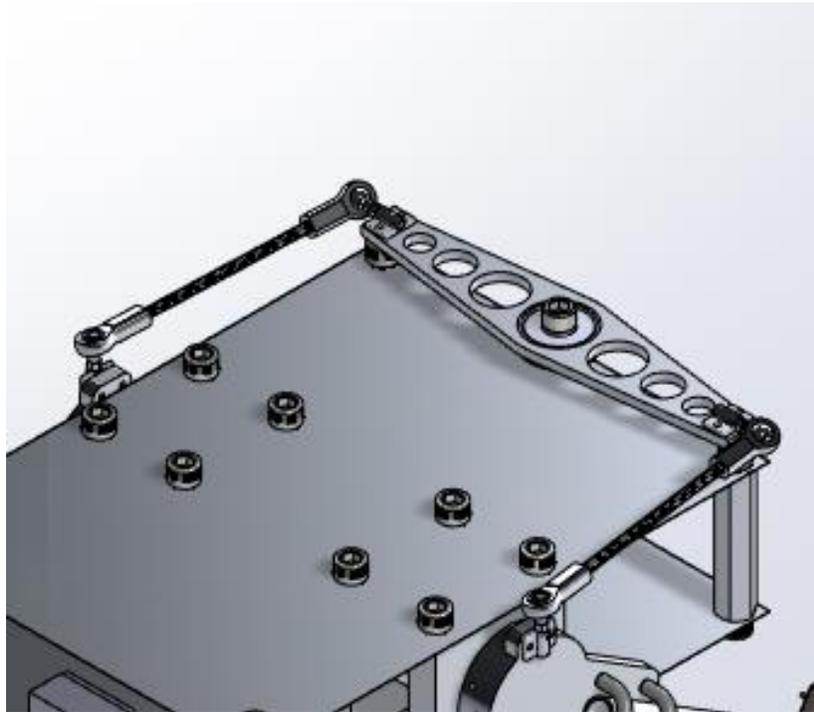
4.1.5 Wheels

The wheel design was comprised of six spokes that revolve around an 8-millimeter hole, with treads situated on the outer surface of the wheel. The wheels are mounted on their respective axles via mounting plates. This reduced the complexity of the wheels and allows the wheels to be easily removed from the axles during testing. Extensive FEA simulations of the wheels were run to reduce wheel weight as much as possible.

Figure 21: An isometric view of the wheel CAD model showing treading details.
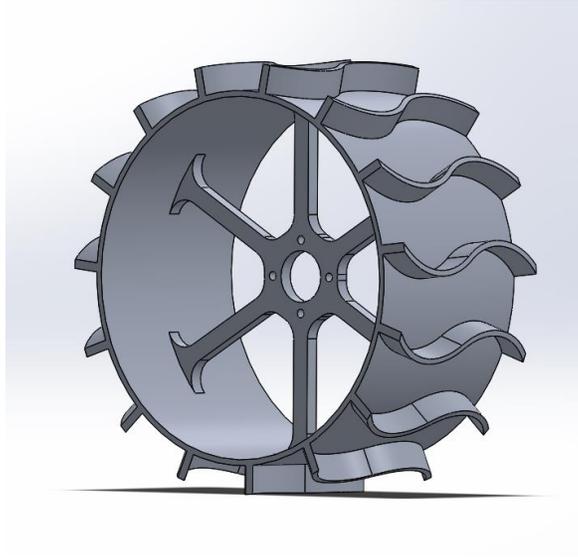
Figure 22: A head-on view of the wheel CAD model to show the inner hub and support details.
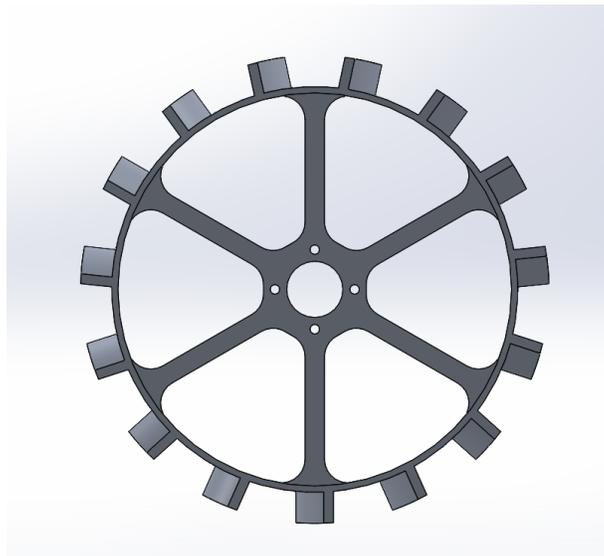
4.2 Software

4.2.1 Autonomy Software Architecture

The autonomy code was designed to be as modular as possible, allowing for easy expansion and modification and providing the possibility of more robust capability in the future. Each component of the software operates as an independent function, running on either one of the onboard processors or the base station. Separating these functions across different processors allowed the specialization of software to be more compatible with future expansions. The path-finding functions, for example, are processed by the base station and sent to the rover. As future expansion may involve swarms of autonomous rovers, this will allow the path-finding software to consider the position of other rovers without the rovers having to communicate with each other as frequently. Instead, the base station can factor in both the current and future position of every operating rover when planning trajectories and transmit this information independently to each rover. Meanwhile, most of the Guidance, Navigation, and Control (GNC) loop outside of path planning is performed onboard the rover. high-performance cost algorithms and functions requiring data transmission can be performed on the onboard Raspberry Pi, while low-level motor control and sensor processing can be performed by the more efficient Arduino microcontroller. Altogether, the software architecture is designed to be as open as possible to any route of expansion.

4.2.2 Path Finding Algorithm

The path-finding algorithm for the autonomy stack allows the rover to plan a trajectory through a pre-determined threat field to minimize a cost function. The implementation used is a pseudo-optimal Rapidly-Exploring Random Tree (RRT*) algorithm, which is a random sampling-based algorithm that produces a space-filling tree throughout the navigation space. The pseudo-optimal variant of this algorithm stores the traversal cost from the base of the tree to each vertex and rewires vertices to different nearest neighbor nodes in the tree if lower-cost paths are found. While this algorithm technically only converges to an optimal solution given infinite execution time, in practice the algorithm more rapidly converges to a pseudo-optimal solution that can be used for navigation. The nature of the cost function also allows for both a spatial cost and a time-accumulating cost. The spatial cost is calculated from the scalar threat field and represents the relative risk of the rover not being able to navigate over any given section of the navigation space. The time-accumulating cost allows an operator to "tune the risk" of the algorithm. A lower time cost will place a relatively larger effect on the spatial

cost, which encourages the rover to take less risk and follow a minimum-cost path. As the time cost increases, the total cost may be lower by taking a shorter route through a slightly higher-risk area. This encourages the rover to take a shorter, riskier path when it is justified.

This implementation of the RRT* algorithm is not designed to be run in real-time onboard the rover. As mentioned in earlier sections, the real-time operation was one of the main tradeoffs between sampling-based search algorithms and graph-based search algorithms, as the latter tend to be computationally simpler and converge to optimal values. However, given the slow operating speed of the rover and the lack of moving obstacles on the lunar surface, real-time operation was not a major criterion when selecting the path-finding algorithm. For these reasons, the RRT* algorithm operates from the base station, simulated by a laptop for this project, with the resultant path being sent to the rover's onboard Raspberry Pi over Wi-Fi.

4.2.3 Kalman Filter/IMU

The GPS receiver onboard the rover has approximately meter-order accuracy at tested latitudes. Given that any strap-down IMU is subject to significant drift over moderate periods, a state estimation and sensor fusion algorithm is necessary to properly localize the position and attitude of the rover. An Extended Kalman Filter (EKF) was implemented onboard the rover to allow the fusion of GPS and IMU data and to use this fused sensor data to reduce noise and drift. This is one component of the core GNC loop, the other being the motor controller detailed below. The relatively low data rate of the IMU and GPS, 100Hz and 1Hz respectively, made position estimation exceedingly impractical and inaccurate but was sufficient for attitude estimation. Therefore, the EKF implementation onboard the rover estimates attitude only, and encoder data is used for odometry to estimate the distance traveled. As stated previously the RRT* path-finding algorithm returns separate vectors of distances and directions to travel, and so encoders measure that distance value while the estimated heading is used to track direction. This decoupled nature significantly decreases the complexity of the EKF algorithm while still providing sufficient fidelity for navigation.

In the rover's EKF implementation, raw IMU data is fed into an algorithm, and the rover dynamic model is used in conjunction with a fourth-order Runge-Kutta numerical integration method to integrate the input data. This is used as the data basis for the prediction step of the EKF algorithm. GPS position and

GPS-derived velocity estimations are then used as the measurement for the update step of the EKF. This then allows for Euler angles to be predicted and from these angles, the estimated rover heading can be determined. This heading can then be passed to the motor control algorithm as the input for direction-tracking feedback control.

4.2.4 Motor Control

The motor control algorithm onboard the rover is the second component of the core GNC loop and consists of two main components: direction tracking, and distance tracking. Both utilize feedback control, but the slow speed of the rover allowed for a simpler distance-tracking controller compared to the higher-fidelity direction-tracking controller. The rover moves slowly enough that full PID control was not necessary for distance control, so a simpler bang-bang feedback controller was utilized for this function. Before the rover reaches the distance setpoint, a logically high signal is sent to all motors that set the motors to operate at their maximum safe continuous torque. This signal is continuously sent until the rover is within 0.1 meters of the distance setpoint, at which point a logically low signal is sent to the motors to stop the rover.

The direction control of the rover is required to be significantly more accurate to allow for accurate pointing to the target position, so a PID controller was implemented. The differential drive dynamic model calculates the required torque variation across each side of the rover's motors to turn at the requested rate from the controller. As the motors already run on a logical high signal from the distance control, Pulse-Width Modulation (PWM) is used to vary the duty cycle on one side of the rover's motors, allowing the rover to turn. Varying the duty cycle in this way allows both controllers to run simultaneously. The combination of bang-bang distance control in conjunction with PID direction control avoids any coupling effects that might emerge from using PID control for both distance and direction.

4.2.5 Image Stitching

While the implementation of a threat field cost map allows the rover to traverse through areas of a lunar crater with known hazards, the potential for unmapped obstacles being present still exists. Given that the rover cannot yet perform dynamic mapping of its environment and instead relies on a predetermined threat field, some ability to detect these unmapped hazards is necessary. To accomplish this while

keeping rover weight to a minimum, a contour detection algorithm was implemented using the existing forward-facing camera on the rover. This algorithm allows the camera to detect borders between high-contrast areas in the camera field, which becomes exceptionally useful in distinguishing foreground objects from background objects as well as detecting shadows on the terrain. Such shadows or foreground objects typically indicate the presence of an obstacle, and contour detection can be used to estimate the size of this obstacle and determine if this obstacle presents a significant hazard to the rover.

The implementation of contour detection on the rover utilizes the OpenCV library, which allows for real-time computer vision functionality implemented in Python code. The contour detection code samples images from the front camera at a rate of 30 Hz. Each of these images is converted to grayscale to allow for one-channel brightness, and a binary threshold is then applied to the grayscale image. This binary threshold samples the brightness of each pixel in the image, converting any pixel above the threshold to maximum brightness, and any pixel below the threshold to minimum brightness. This results in a black-and-white map of the image, in which high-brightness and low-brightness areas are distinguished. The program then identifies the edges of these areas, or contours, which correspond to areas where the contrast of the image varies suddenly by a significant amount. In the lunar environment, these areas are likely to correspond to edges of sizable positive obstacles such as rocks, the lip of negative obstacles such as craters, or shadows of positive obstacles. Any one of these may present an unnavigable obstacle from the rover. The contours of the potential obstacles are highlighted by the program, and the size of closed contours or the length of open contours can then be determined. As a visual reference to the end user, the contours remain colored green on camera footage as demonstrated in the figure below to indicate no object is currently identified as a hazard.

Figure 23: The contour map testing showing objects that pose no identifiable hazards as seen by the selected micro rover camera.
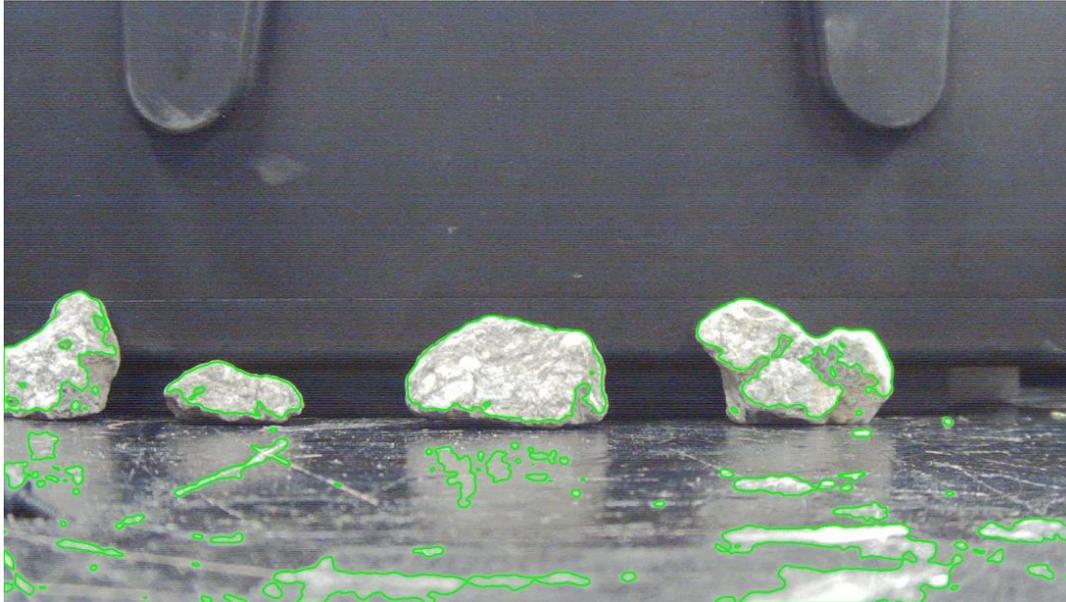
If any single contour is determined to be of sufficient size to be a potential hazard, this object contour is tracked over subsequent frames. Given the moving speed of the rover, any object that remains of hazardous size for over 60 frames or 2 seconds at 30Hz is considered to be likely in the path of the rover. The below figure shows how the video feed changes when a hazard is identified. If both these size and persistence criteria are met, the contours in the video feed are colored red to indicate a likely hazard is in the path of the rover, and an interrupt is sent to the GNC loop to immediately stop power to the motors. At this point, the ground station can be notified, and manual teleoperation can be initiated to clear the hazard. Once the hazard is cleared, the pathfinding function must be re-initialized with the current position of the rover as the starting position and the goal position remaining the same.

4.3 Electronics hardware

The electrical components are outlined in Table 1. Their specifications, including voltage, load current,
and power draw are as noted in Table 2.

Table 2: A list of power regimes of every selected electrical component.

Element	Voltage (V)	Load current (mA)	Power draw – operational (mW/h)	Power draw – idle (mW/h)
Camera	5	350	1750	0
Motor	12	1600	6000	0
Microcontroller	5.5	73.19	658.71	1000
Heating	12	1000	50000	50000
Total			58408.71	51000

Note. The total power draw without the heating element in normal operation was 8408.71 mW/h, and in idle was 1000 mW/h. The components are connected as shown in the wiring diagram in Figure 25. The connections made to all the components are based on the controller. Connections are made to the motors, GPS module and antenna, battery, camera, and IMU.

Figure 25: Electronics wiring diagram for the entire micro rover.
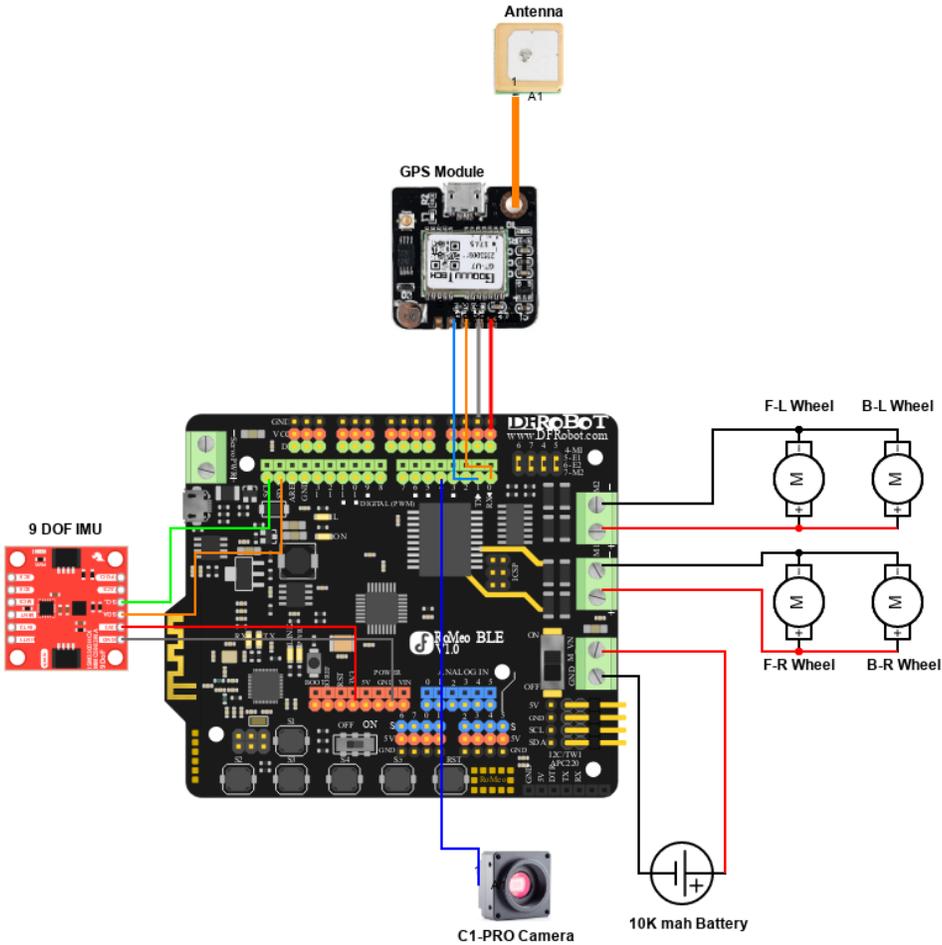
The components were preliminarily arranged as seen in Figure 26. This arrangement included components that the team had researched but did not end up being the final choice for the hardware components. This preliminary arrangement was made to reduce the volume inside the rover chassis.

Figure 26: A preliminary arrangement of electrical components within the micro rover chassis.
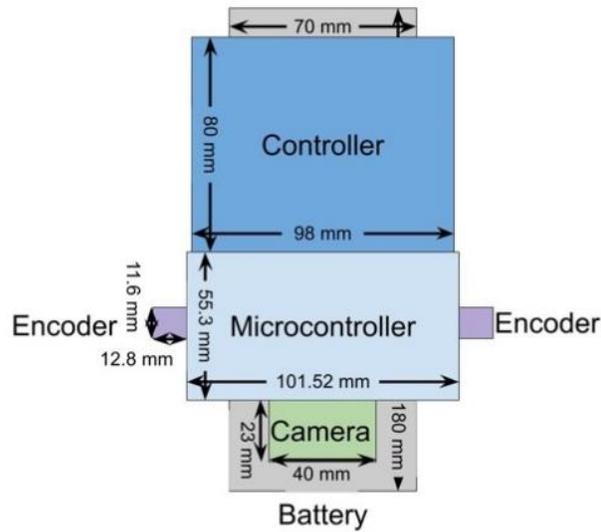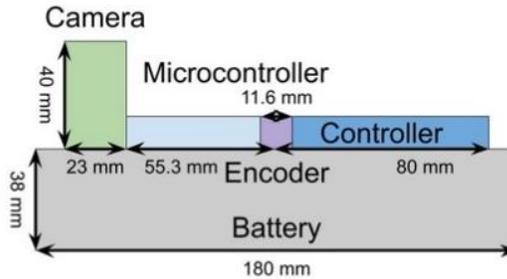
The electronics components draw very little power overall and can run off the battery for 111 hours at rover idle with no heating, or 2.18 hours at idle with heating. It is evident from this that active heating of the rover is the single largest power drain on the rover.

4.3.1 GPS and INS

The Global Positioning System (GPS) receiver and Inertial Navigation System (INS) were integrated and connected based on the wiring diagram seen in Figure 25. The GPS unit selected by the team was a NEO-6M GPS module including its associated passive antenna. The unit features a time-to-first fix of approximately 30 seconds from a cold start and has a horizontal accuracy of 2.5m, a velocity accuracy of 0.1 m/s, and a 1Hz navigation update rate. It had an operating voltage of 3.3V to 5.2V with an operating current of 50 mA normally and 30 mA in power-saving mode [20].

The INS consisted of a nine-degree-of-freedom ICM-20948 Inertial Measurement Unit (IMU). The IMU contains an accelerometer, gyroscope, and magnetometer, each of which operates with three degrees of freedom. This unit can operate within a range of 1.95V and 3.6V, with the breakout board having the ability to step down the input voltage from 5V into the appropriate range. Both the gyroscope and the accelerometer are micro-electromechanical systems (MEMS) [21]. The IMU was used in conjunction with the GPS to run the positioning and path planning algorithms as outlined in section 4.2.

4.3.2 Camera and lens

The camera selected was a KUROKESU C1-PRO industrial image sensor. This camera utilizes a Sony IMX290 sensor with the capability to produce 1920x1080 resolution video at 30 frames per second within the operating temperature of -50ºC to 85ºC [22]. The team mounted this camera on the front bottom board of the chassis. There was a hole cut within the mylar to enable a clear viewpoint for the camera lens. The camera lens is an Arducam 4-12mm Varifocal C-Mount Lens designed to work with a Raspberry Pi-compatible camera [23]. As seen in the wiring in Figure 25, the camera was wired to the controller, allowing video data to be sent to the base station via the WiFi capabilities of the controller.

4.3.3 Motors

The selected motors were 20D metal gear motors manufactured by Pololu. These motors are 12V DC gear motors with a 488.3:1 metal spur gearbox. They have a D-shaped output shaft with an equivalent circular diameter of the shaft of 20mm. These motors have a stall current of 1.6A and a no-load current of 0.08A. The maximum stall torque to be output by these motors is between 1.9 and 25 kg-cm at the no-load speed and at stall respectively [24]. These motors were installed behind-the-wheel spokes within the wheel mechanism. They were installed with the attached encoders as outlined in section

4.3.5. The motors were connected to the controller through wiring to the VCC and GND pins as seen in Figure 26.

4.3.4 Microcontroller and Controller

The microcontroller selected was a Romeo BLE Arduino-based control board. The RomeoBLE uses an ATmega328P single-chip microprocessor with the Arduino Uno bootloader, making it compatible with the Arduino IDE. Additionally, the Romeo BLE features a two-channel DC motor driver with a 2-amp maximum current output, supporting input voltages ranging from 5-23 volts. This allowed a single board to be used to both run motor control algorithms and power the motors, as well as process sensor data input. Most importantly, the Romeo BLE integrates Bluetooth 4.0 into the microcontroller, allowing an iOS app to be used to teleoperate the rover when required. Teleoperation was a key requirement for the rover as it features only partial autonomy, and this board provided such functionality without additional hardware.

The ATmega328P microprocessor on board the Romeo BLE lacked computational power to perform state estimation and could only receive Bluetooth commands and not transmit data. Therefore, a Raspberry Pi 4 was implemented to run the EKF algorithm and to send and receive data from the base station. The base station and the Raspberry Pi communicate via Wi-Fi, and the Pi performs two-way serial communication with the Romeo BLE via a USB cable. This communication structure allows path planning data to be sent from the rover to the base station, sensor data to be sent from the Romeo BLE to the Raspberry Pi for state estimation, and attitude estimates to be sent back to the Romeo BLE for motor control.

4.3.5 Encoder

The motor encoders chosen by the team were the Pololu magnetic encoders for 20D gear motors. These encoders use hall effect sensors to measure the rotation of a magnetic disk on the motor shaft and are powered by the VCC and GND pins as seen in Figure 26. These encoders were soldered to the motors within the wheel mechanism. They were soldered ensuring that the magnetic encoder disc was pushed onto the motor shaft. These encoders allow estimation of the linear distance the rover has traveled by relating the number of rotations of the motor shaft to the radius of the rover wheels. [25]

4.3.6 Battery

The battery is an 11.1V lithium-polymer battery pack with a capacity of 10000 mA/h. This battery has three cells and has a maximum discharge rate of 35C while constant, and 45C during a burst. It charges at a rate of 5C using an XT60 discharge plug. This battery was chosen due to the performance of lithium-polymer batteries in extreme temperature conditions. The temperature range for this battery is -20ºC to 60ºC while the electronics system is operating, and it has a temperature range from 0ºC to 45ºC while charging. The battery was the primary source of power for the rover and could be charged by the solar panels while the system was idle.

4.3.7 Solar panel

The team was able to use a double layer of 1/4 -in acrylic sheet mounted to the top of the rover chassis to simulate the volume, mass, and placement of a solar panel. This resultant solar panel simulant was 1/2 in thick which the team accomplished by gluing together two sheets of acrylic. The solar panels were mounted with additional acrylic to the chassis. These solar panels would have been used to charge the battery that powers the rover. These solar panels would have been able to charge while the rover was in areas of the mission that were not in complete darkness, and the mission mapping would have instituted a part of the path in a part of the crater in which the solar panel would be able to charge.

5. Simulations

5.1 Ansys Static Drop Test

To confirm that the final design could survive a 4-inch drop test on earth, an estimate of the forces involved was needed. Ansys Explicit Dynamics was chosen as the tool to simulate the rover in a drop test, as it can solve dynamic simulations with custom materials. A heavily simplified CAD model of the four-wheel rover design was created to reduce the workload of the computers, and the simulation was set up with varying mesh sizes to further reduce the complexity of the simulation. Every component of the rover was defined to be made of aluminum 6061. The pivoting linkage was defined by using revolute and ball joints to connect the individual links. The initial state of the rover was defined to be only a few centimeters from a rigid, fixed plate, and at a slight angle so that the four wheels would impact the plate at different times. The rover was given an initial downward velocity of 1.40 m/s, corresponding to a four-inch drop in Earth's gravity, and a 9.8 m/s^2 squared downward acceleration was applied to all bodies in the rover. The simulation was solved for 0.2 seconds of simulated time, to confirm that the rover would not bounce higher than the 4-inch supposed drop height. The joint probes were defined on every joint to show the forces exerted on each joint for the impact test.

Several drop-test simulations were run, with different mesh settings, and many of the results seemed outrageously high and varied greatly with minor changes in mesh sizing. Some forces were reported to be about 4000 newtons, in directions that made no intuitive sense. For this reason, the joint force probe data was discarded, and the focus was turned on the timing of the impact. The velocity of the rover before impacting the rigid plate was 1.40 meters per second downward, and the post-impact velocity was estimated to be 0.7 meters per second upward. The impact occurred in only 0.03 seconds, so the rover's upward acceleration during that time was 70 meters per second squared on average. This value was rounded up to 100 meters per second squared, as the acceleration cannot be assumed to be constant during the impact. This acceleration, combined with the masses of the rover components, was used to simulate the final rover design with Ansys Static Structural.

5.2 Ansys Static Simulations

After the drop test was conducted, additional static simulations on various components of the design were needed to simulate how the micro rover would structurally react in the lunar environment. The

full rover assembly was split into 5 major subassemblies that were deemed critical to the micro rover if one were to fail. These subassemblies were as follows; Chassis – Pivot, Pivot, Wheel Tread, Leg-Wheel, and the Chassis itself. Each subassembly was tested structurally so that if a major design flaw was shown, the subassembly could be improved upon to prevent catastrophic failure. The software Ansys Workbench R1 2022 was used to conduct the static simulations, because, within Ansys Workbench R1 2022, material properties could be applied to the subassembly model, and specify parameters of the simulation such as where the force was applied, or what on the model is considered fixed in motion. As mentioned, Aluminum 6061 was used as the material for almost all components on the micro rover, as it was found that the material becomes far stronger the colder it becomes. To emulate Al 6061 in the lunar environment, a custom material was declared within Ansys. When creating a custom material in Ansys, the user has the freedom to input any numerical value into any material property of choice. For simplicity, the custom material had the following properties: Modulus of Elasticity = 75. 84 GPa (11,000 ksi), Poisson's Ratio = 0.33, Yield Stress = 327.5 MPa (47,500 psi), and lastly Ultimate Stress = 448.16 MPa (65,000 psi). These values were found according to strength vs temperature charts (Appendix B) for Aluminum 6061 at -130 K. It is worth noting that this general procedure of declaring a custom material within Ansys Workbench was done for every static simulation conducted.

Figure 27: A side view of the full micro rover drop test within Ansys R1 Workbench 2022.
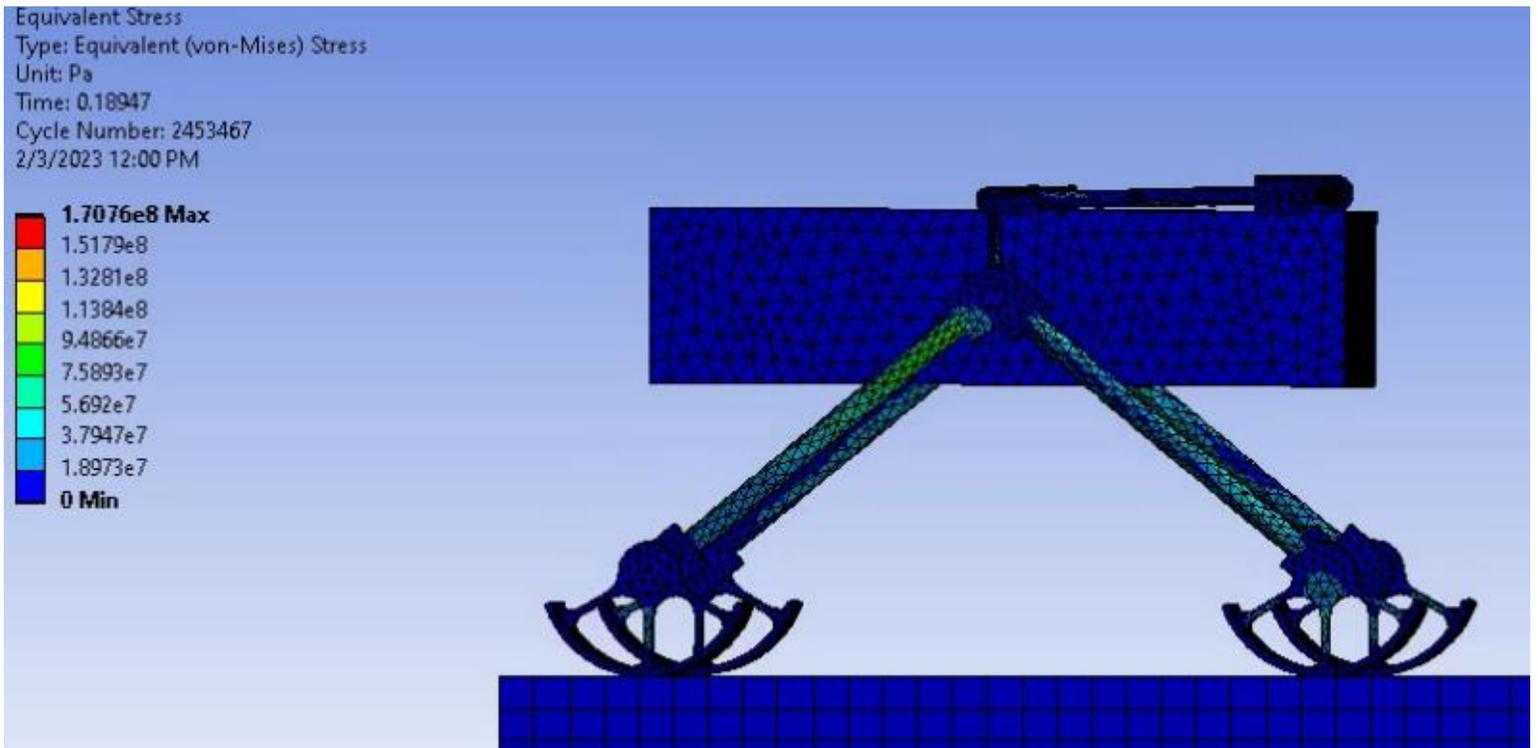
Figure 28: A isometric view of the full micro rover drop test within Ansys R1 Workbench 2022.
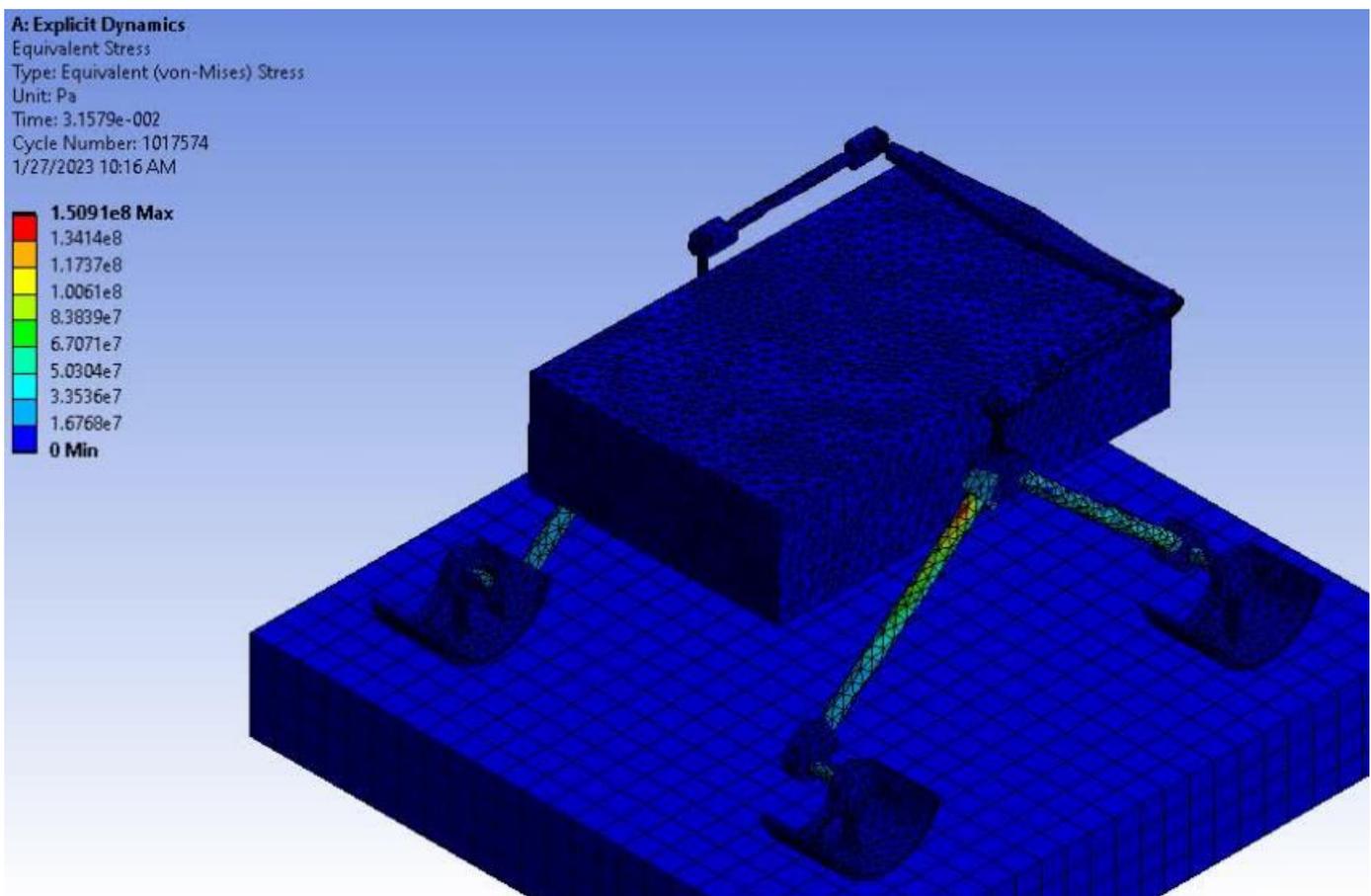
The static simulations also allowed each subassembly evaluation to display which results were generated in the simulation. The results of the simulation primarily displayed the von-Mises stress and Factor of Safety present in the model when X amount of force was applied, but on certain subassemblies, the Deformation of the model was displayed in addition. The results guided the decision in determining if a part was structurally stable for the lunar environment. Starting with von-Mises stress, after the force was applied at a specified location, the simulation would display how the stress was dispersed throughout the subassembly. If a component within the subassembly modeled as Al 6061 material properties appeared to have too much stress in accordance, the subassembly model returned to SolidWorks and where improvements were made to the design to lessen the stress that component experienced. Additionally, the Factor of Safety played an important role when looking at the overall design of some components too. If this value was found to be too high, the model or component would

be edited in SolidWorks by reducing thickness to save weight and allow for it to not be as overbuilt. This decreased the factor of safety of the given component within the subassembly model. The Deformation analysis only applied to a subassembly with components that if deformed too much, complications on other micro rover components could arise, or the entire subassembly could fail altogether.

5.2.1 Early Simulations

Static simulations acted as the justification for determining if components on the micro rover were deemed sufficient for manufacturing. There initially were two choices of simulation software to choose from, the first being SolidWorks, and the second being Ansys Workbench. Both Ansys and SolidWorks required a learning curve to be overcome before conducting simulations that provided real data for analysis. The learning curve for the simulation software was diminished through a combination of WPI info sessions, tutorials on YouTube, and even a user interface guide produced by both SolidWorks and Ansys. Initially, static simulations were conducted in SolidWorks because it was more familiar software to the MQP team. An early static simulation testing the treads on the wheels can be shown in Figure 29. The purpose of this simulation was to show how much force it would've taken to shear the treads off the wheels. A force was applied to the front face of the treads and increased until a deformation of X amount of mm was shown for the tread. However, this test was producing forces in the range of 1.5 million Newtons and hardly affected the wheel body itself. With the level of force being produced, it was expected that more deformation to be seen on the wheel instead of just the treads.

Figure 29: An early simulation testing the strength of a wheel with its tread within Solidworks 2022.
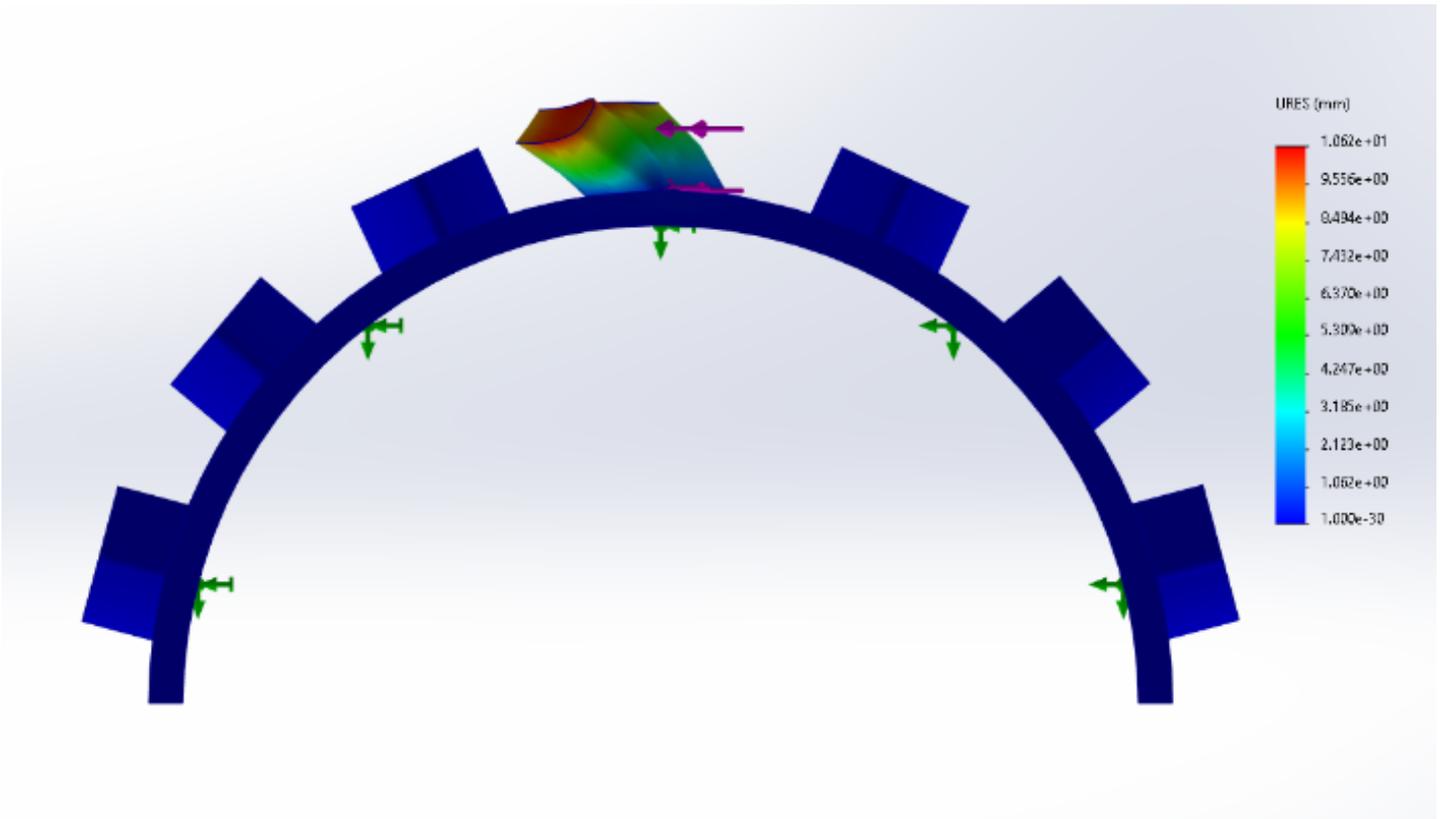
Additionally, Figure 30 showed an early von-Mises stress simulation on how the stress affected the top plate of an older chassis design. The distribution of stresses was somewhat inaccurate about how the forces were applied, as the forces were located on the corners of the top plate. It was expected that stress would stem from the corners, but as shown, it stemmed from the front and back middle edges primarily. This could be because of some initial assumptions made to get these early simulation results, but the stress didn't match the application of the forces present with or without the assumptions made. These early simulation results were then compared to simulation results in Ansys Workbench. Ansys had the steepest learning curve of both software, but in return, it simulated far more specific scenarios and produced more precise data. A custom material with user-specified properties could be declared within the software as mentioned previously. SolidWorks only had set materials with set properties and didn't allow access to creating any custom material.

Figure 30: Distribution of von-Mises stresses over an early chassis design when force is applied to the corners to the top of the CAD model.
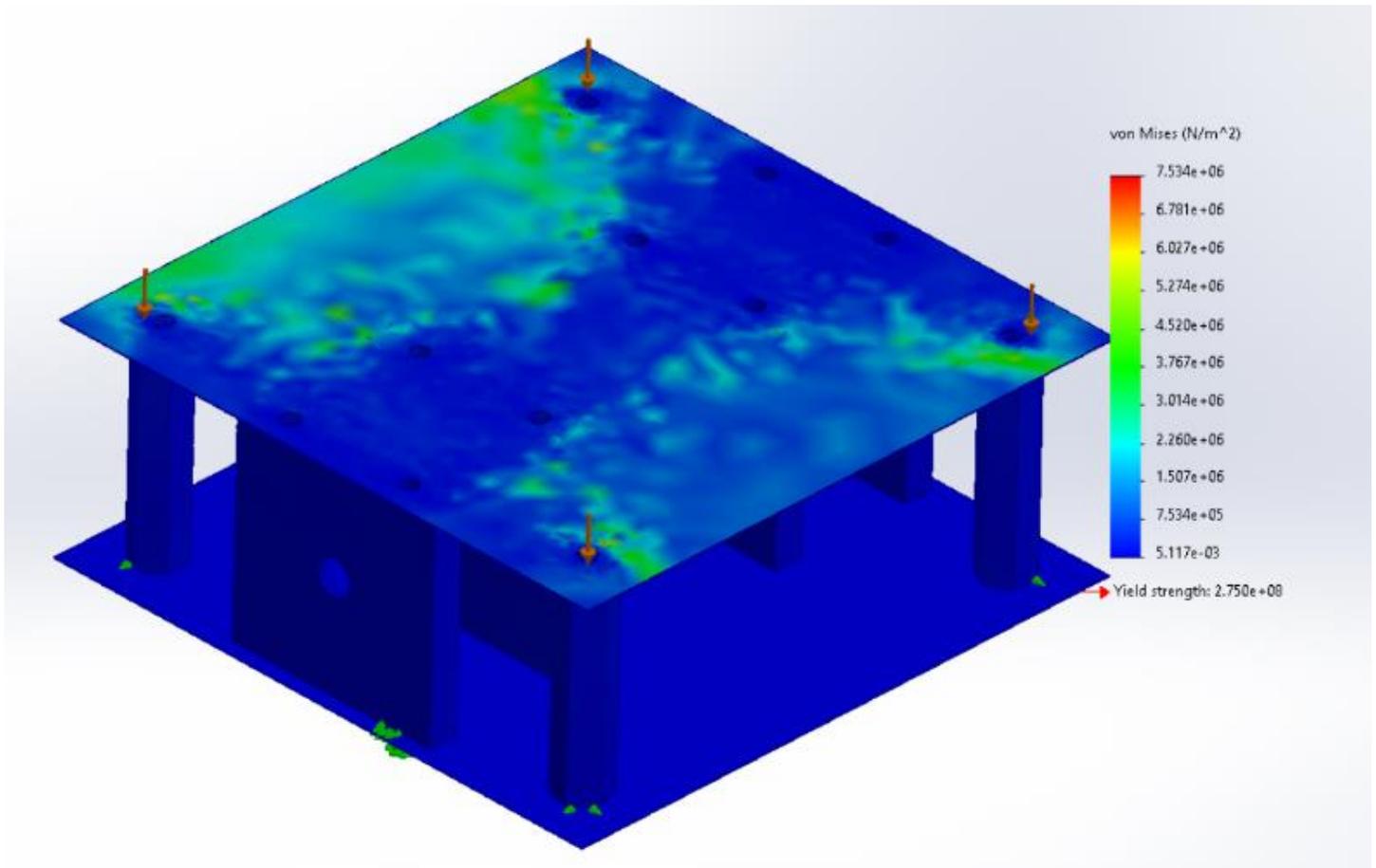
5.2.2 Wheel and Tread Analysis

The wheels of the micro rover are one of the most critical components, if they were to fail, the micro rover would be inoperable. The wheels were tested for how they would react to a substantial amount of force applied to the treads. As mentioned, Ansys allows the user to declare a wide variety of parameters within the simulation window, such as what parts of the model are fixed, or where the force will be applied. A 330 N force was applied perpendicular to the vertical face of the tread for this simulation, in an attempt to show how the force affected the overall wheel strength. This force value comes from the maximum motor stall torque at a wheel radius of 75 mm. Next, bodies or faces on the model were

declared as fixed to prevent the whole wheel from moving with the force. The mounting holes located in the center of the wheel were selected to be fixed because of the direction of the applied force. This would cause the wheel to twist in motion, creating a focus on the strength of the inner support legs in addition to the wheel. Additionally, compression of the wheel was looked at to see if it could support the weight of the micro rover and withstand 330 N of force. The compression test had the force facing downwards on the wheel and was applied in the center hub. With all parameters declared, the simulation results show that the wheel itself is more than sufficient to withstand a force of this magnitude. In Figure 31, most of the von-Mises stress was located on the wheel supports attached to the center hub.

Figure 31: The distribution of von-Mises stresses over the wheel when force is applied to the top treading and the wheel center is fixed in place.
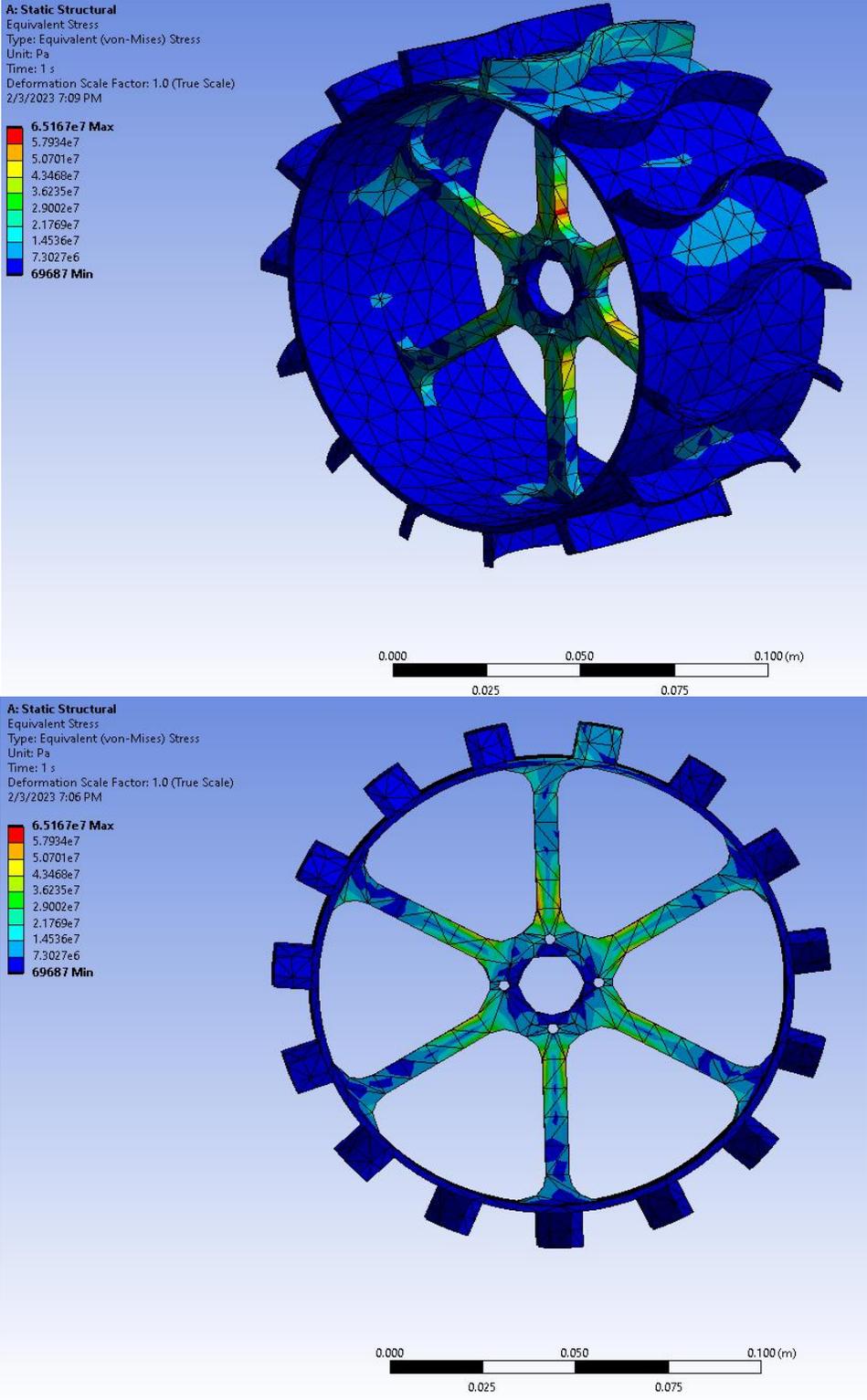
The maximum value created from this scenario is 65,167,000 Pa, or 65.167 MPa, and is located near the center of the wheel hub. This stress is expected to occur near this location because of the force creating a twisting motion to the whole wheel as previously described. Additionally, in Figure 32 the simulation shows the factor of safety of the overall wheel, generating the lowest factor of safety of 5.0256.

Figure 32: The distribution of the Factor of Safety over the wheel when force is applied to the top treading and the wheel hub is fixed in place.
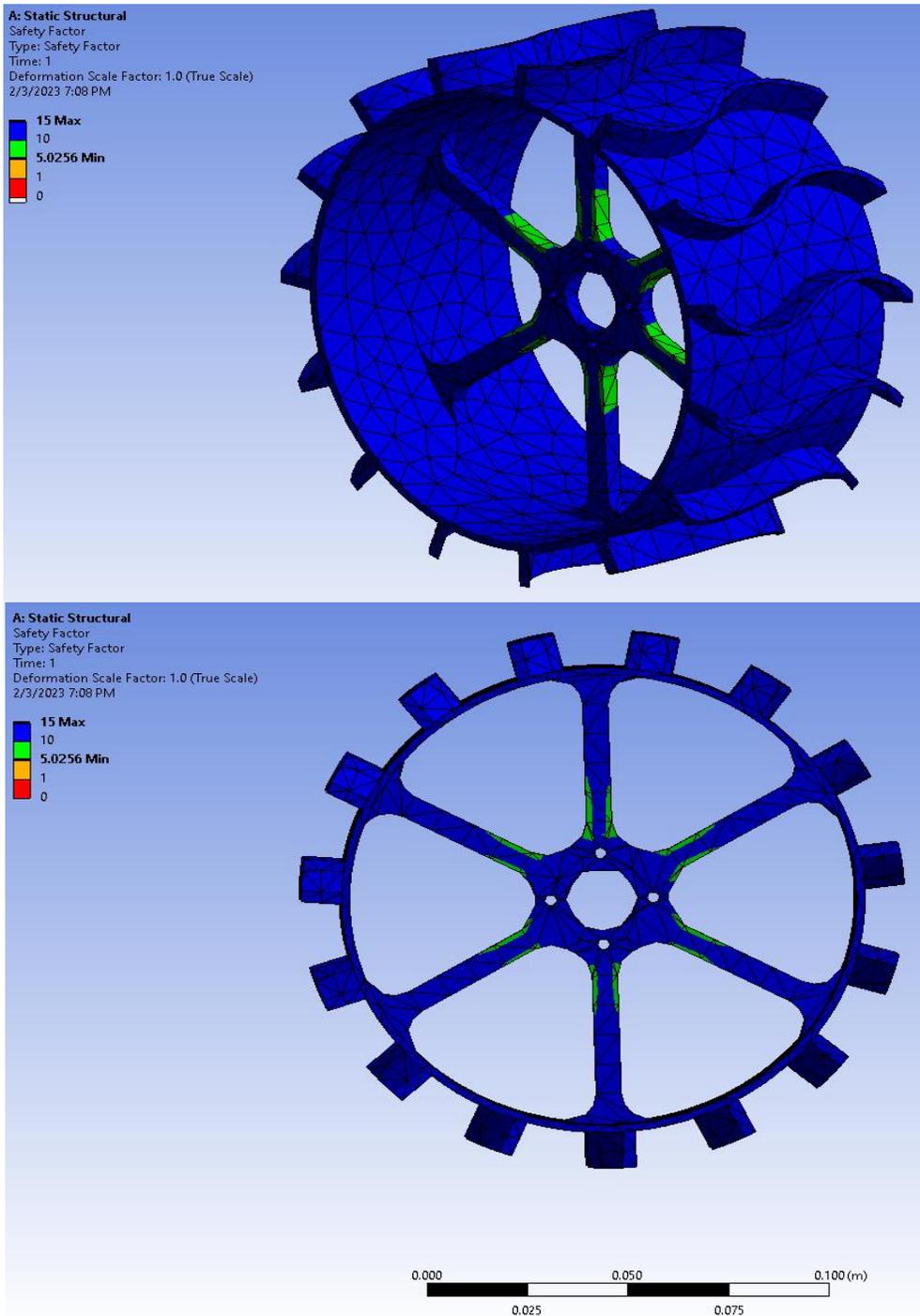
The lowest factor of safety appears near the wheel hub on the supports, while the maximum factor of safety of 15 is shown everywhere else on the wheel. In Figure 33 the results of the compression test are shown, with most of the stress being located towards the bottom of the wheel.

Figure 33: The distribution of von-Mises stresses over the wheel when a compressive force is applied to the top of the wheel while the wheel hub is fixed.
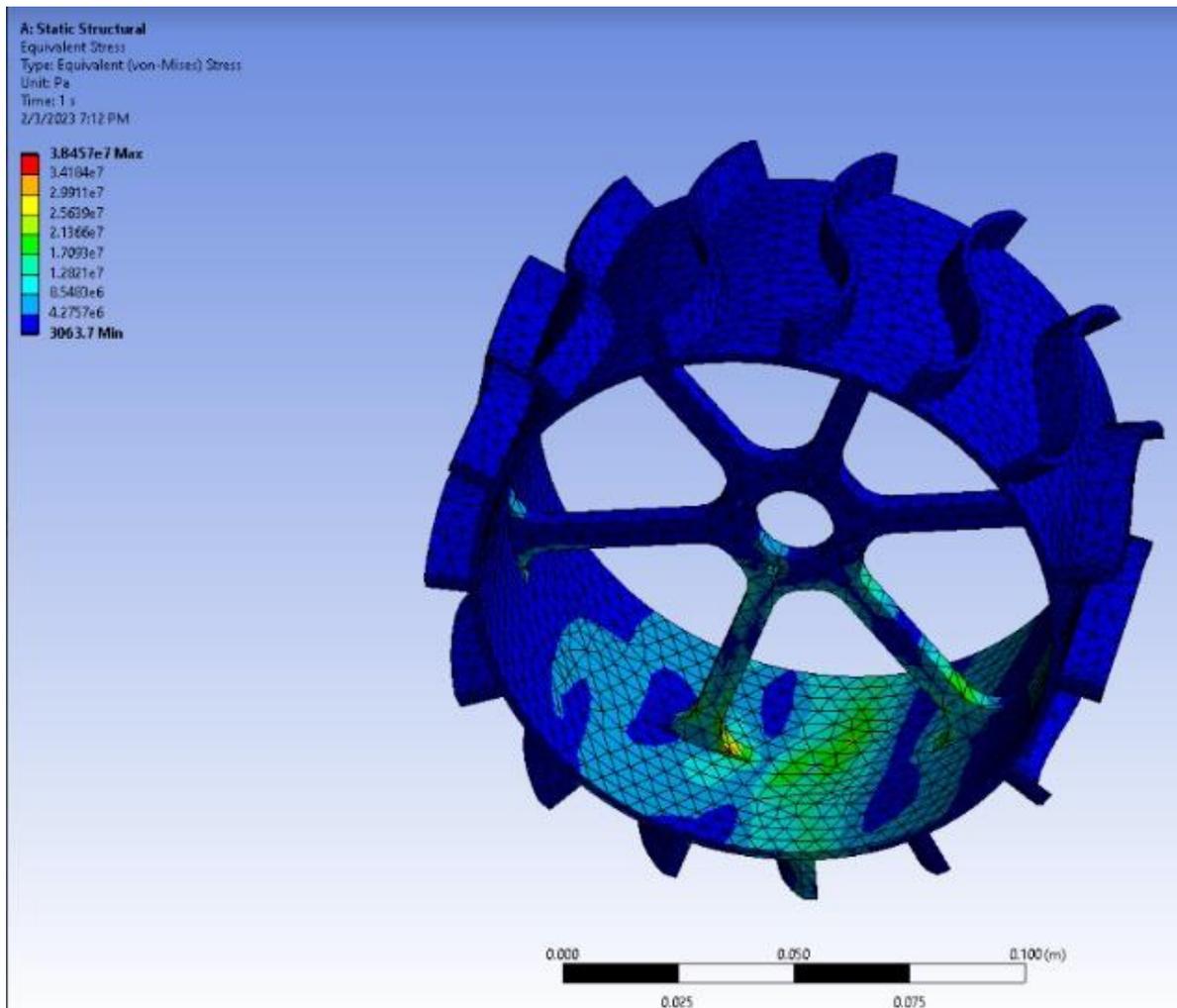
The maximum amount of stress von-Mises generated was 38,457,000 Pa or 38.457 MPa, while the minimum amount of stress present of 306.3 Pa. With the maximum von-Mise stress and the lowest factor of safety, the wheel was determined strong enough when made from 6061 Aluminum under these

load conditions. The initial wheel design was too overbuilt, creating a minimum factor of safety of 15. This prompted a small redesign of the wheel so it wouldn't be so overbuilt, and as a result, the overall weight of the wheel was reduced by 55%. Different trials of experimentation were conducted in Ansys with the wheel design until a factor of safety of 5 was generated. This provided more than enough strength for the wheel to support the full weight of the rover while not being as overbuilt compared to the predecessor. Primarily, everything on the wheel was made thinner, with the inner supports made wider for structural support. After each change, the wheel returned to the Ansys simulation to test if the factor of safety criteria was met. If the criteria were not met, more edits to the wheel took place before returning to the simulation once again. It is worth noting that the simulation parameters are designed to test the component at the maximum amount of force it could encounter. The forces the wheel tread, or the wheel itself, will be exposed to constantly on the lunar surface are far lower than what's simulated.

5.2.3 Wheel–Leg Analysis

In addition to the wheels, the legs are also vital components of the micro rover. The wheel legs connect the motors to the wheels, while also connecting the whole assembly to the main chassis of the rover. The legs needed to be strong enough to not only support the entire weight of the micro rover and payload but also strong enough to prevent any potential catastrophic failures. This subassembly was tested with a downward acceleration applied to the whole subassembly, with a constant force applied downwards on the pivot plate. The downward acceleration and applied force were chosen to be 110 m/s^2 and 140 N respectively. The reason an acceleration force is present was to test how the wheels and legs experienced the impact of falling. It is similar in design to the drop test conducted on the micro rover but more simplified with exaggerated acceleration values. If any part of the subassembly failed because of the downward acceleration, the mobility of the micro rover could be immobilized. The applied force of 140 N was chosen because it provided roughly three times the maximum weight of the micro rover. If the subassembly can support a weight three times the expected weight, it will be more than sufficient to survive expeditions. The bottom of the wheel treads was selected to be fixed to mimic the subassembly standing on the ground.

After all the parameters of the simulation were set up, Figure 34 displayed the distribution of von-Mises stresses experienced on the wheel-leg subassembly. On the legs itself, the maximum amount of stress shown is approximately 8,208,100 Pa. The maximum value of von-Mises stresses the subassembly

experiences is approximately 3.6966 MPa. This maximum value was located on the motor axles that connected the wheels to the legs.

Figure 34: A distribution of von-Mises stresses experienced on the wheel-leg subassembly accelerating downwards while also experiencing an applied force on the main front plate connecting the two legs together.
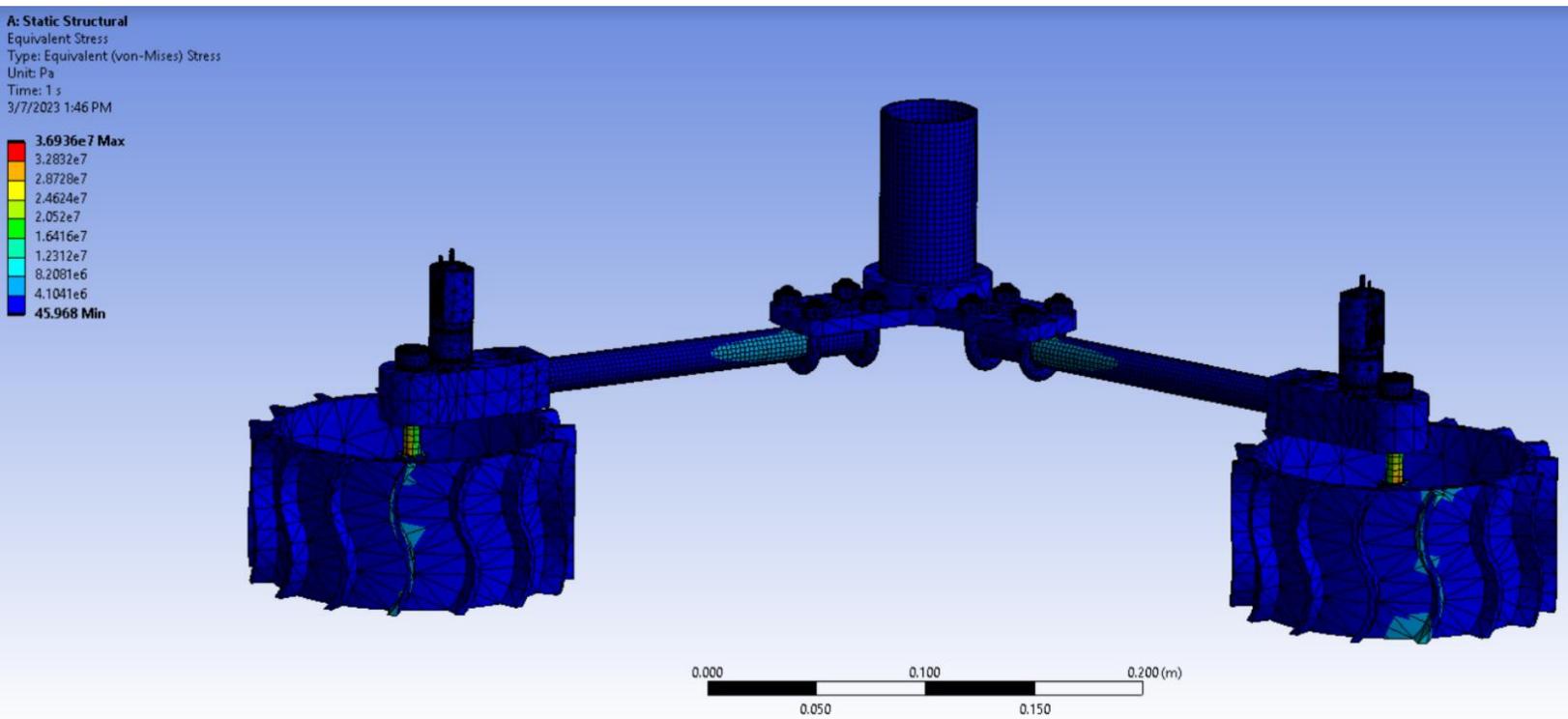
It initially was a surprise to see all the stress located on the motor axles, but with how the simulation was declared, the forces are expected to be seen in this location. The motor axles will support the entire weight of the micro rover, while also connecting the wheels to the rover's chassis. Despite the maximum stress being located on the wheel axel, the axel itself is strong enough to support the required weight of the micro rover because of its factor of safety.

Figure 35: A closer look at the Factor of Safety distribution on the axle that connects the wheel to the motor mount attached to the wheel-leg subassembly.
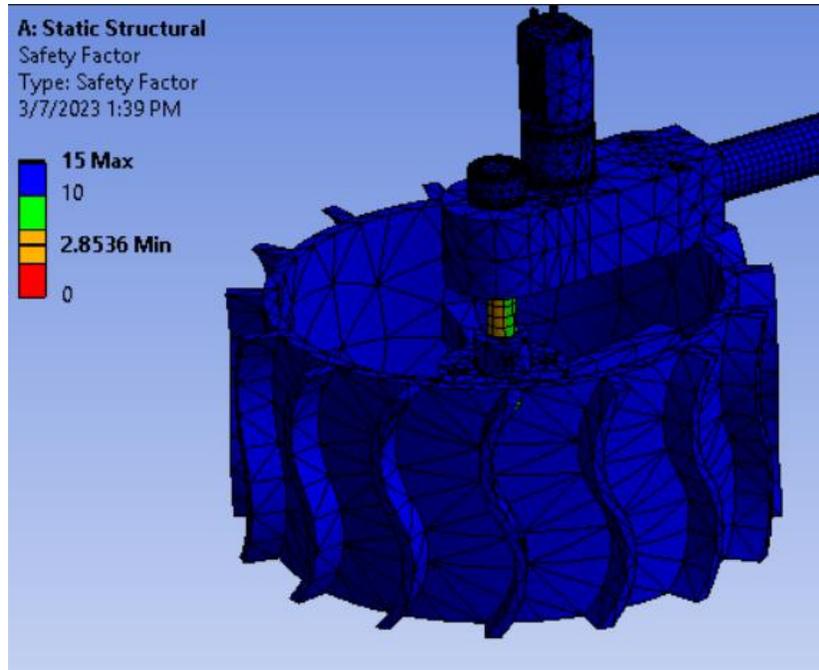
In Figure 35, the factor of safety for the motor axel is found to be 2.8536, while the rest of the subassembly generated a factor of safety of 15. The factor of safety generated on the motor axel is sufficient to properly support the weight of the micro rover. Lastly, the deformation of the wheel legs was analyzed under this scenario. In Figure 36, the deformation from the simulation is shown to increase from the base of the wheels to the main pivot tube connecting the wheel leg to the chassis. The minimum deformation shown on the subassembly is 0.081 mm located on the top half of the wheel, while the maximum amount of deformation of 0.7352 mm is located on the main pivot tube. As shown in the stress and factor of safety analysis, it would've been expected the motor axel would experience the most deformation, but instead, most of the deformation occurs within the pivot tube that connects inside the chassis. However, the deformation overall on the whole subassembly still allows the micro rover to move mechanically as intended without complications, meaning, the wheel-leg assembly is built strong enough for its intended purpose.

Figure 36: A distribution of the deformation experienced on the wheel-leg subassembly accelerating downwards while also experiencing an applied force on the main front plate connecting the two legs together.
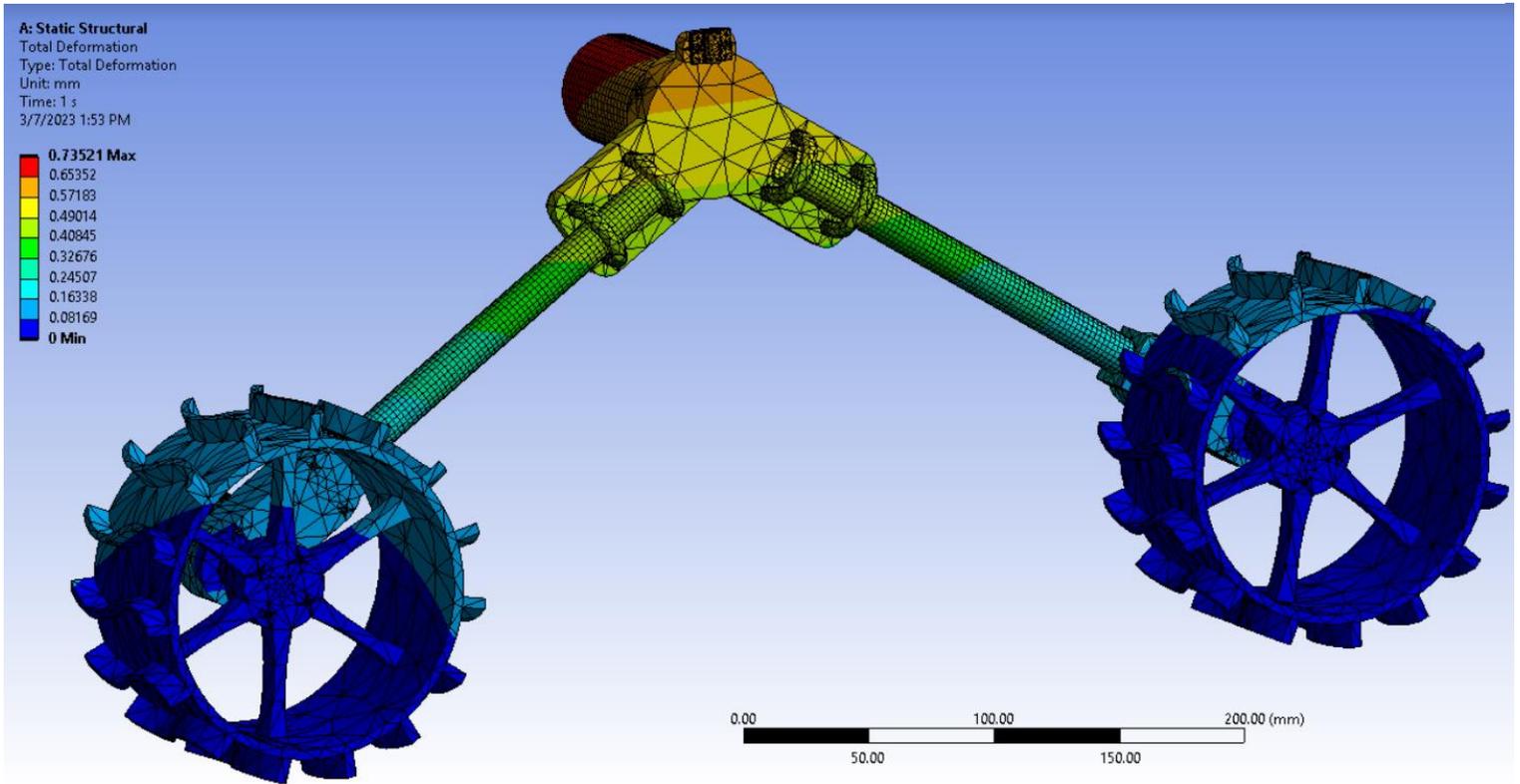
5.2.4 Chassis Analysis

The chassis holds all the electrical components while also connecting all the mechanical components, making the micro rover operable. If the chassis were to fail structurally, it could crush the electronics under its weight causing complications for the entire rover. This simulation tested how the chassis would behave if accelerated downwards at 110 m/s^2 while impacting the ground in a head-on collision. Like the wheel-leg subassembly simulation, the acceleration acted as a simplified variation of the full micro rover drop test conducted. As a result of the applied acceleration, the factor of safety of the entire chassis body was analyzed to see if the subassembly was heavily overbuilt. However, even if the subassembly was overbuilt, no changes were made to the design unless it was critical, because of the weight restriction and the top and bottom plates being thin already.

With simulation parameters set in place, the factor of safety generated throughout the chassis is shown in Figure 37. Most of the chassis in this scenario experienced a factor of safety of 15, but towards the front of the micro rover where the camera is located, a huge decrease is shown. The surrounding area around the camera experienced a factor of safety of 1.429. This location has a lower factor of safety because the top and bottom plates of the chassis are made of 1 mm thick Aluminum 6061 sheets as mentioned.

Figure 37: The Factor of Safety distribution on the chassis body when accelerating downwards and impacting the ground.
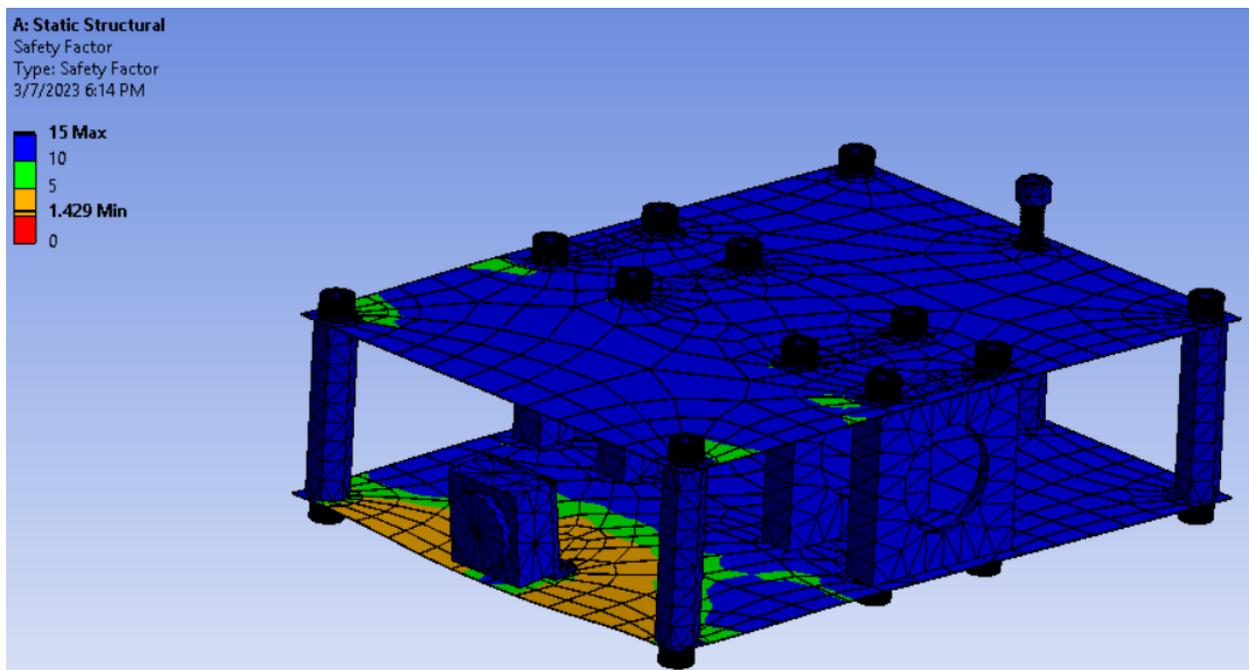
A similar distribution is shown in the equivalent von-Mises stresses on the chassis. In Figure 38, the primary higher concentration of stress values at 40,097,000 Pa is located in the surrounding area near the camera extending to the front left and right hex supports. The remaining portions past the front camera area of the chassis only experienced a stress of 25.08 Pa. What's interesting to note, is that the changes in the factor of safety and even the equivalent stresses only appeared on the bottom plate. One possible reason was because of the bottom plate carried additional weight compared to the top. The bottom of the plate would hit the ground first compared to the top just strictly because of the weight. If

placed in extreme conditions constantly such as this static simulation, the chassis would likely fail in some way. However, if the failure occurred near the camera, the micro rover could remain operable without the use of its full range of sight. This is because the strongest points of impact were designed in the middle of the chassis instead of the front.

Figure 38: The distribution of von-Mises stresses on the chassis body when accelerating downwards and impacting the ground.
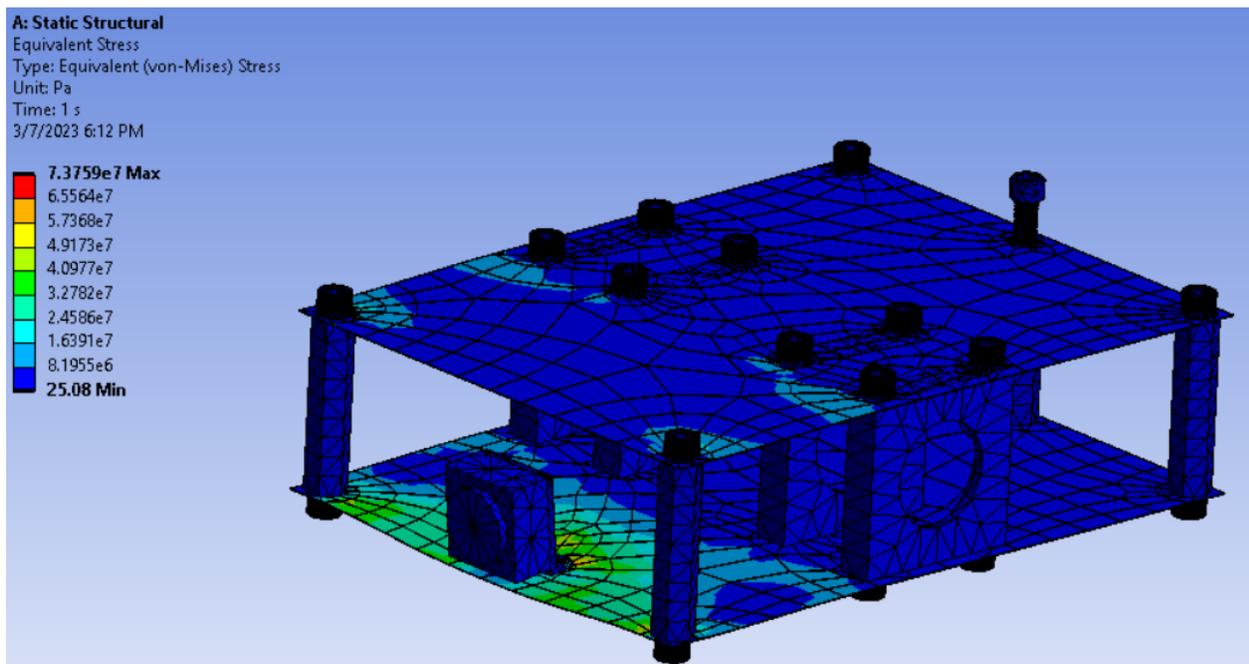
5.2.5 Pivot Analysis

If failure were to occur in the pivot, the rover would lose the suspension system and become unstable as a result. The way that the micro rover is designed, the pivot bar acts as a keystone to a stone bridge, it bonded together the left and right set of wheels on the rover and kept the chassis upright. This simulation focused on the strength of the pivot bar itself under a 200 N load located near the center pivot point facing rearwards, testing if the pivot bar would snap in half. With how the force is applied, it should create a motion like what you'd expect when bending a pencil in your hands or trying to break a stick in half. Lastly, the mounting holes near the end of each pivot bar were selected to be fixed for these simulations.

Under the declared parameters, Figure 39 shows the generated distribution of von-Mise stress. The distribution is relatively even, with a maximum stress of 24.334 MPa, and minimum stress of 263 kPa. The higher concentration of stress occurred towards the edges of the pivot on both sides. This was expected as the force is causing the top edge of the pivot to experience tensile forces, while the bottom edge will experience compressive forces. In addition to stress analysis, the pivot generated a minimum factor of safety of 15 throughout the entire part, meaning that it was heavily overbuilt. Rather than redesigning the component, it was concluded that the part would remain in its current state for a couple of reasons. The first reason is that if the pivot bar was made thinner, it would allow for a lower factor of safety at the cost of potential problems occurring when attaching to the main bearing located on the chassis. Additionally, because of how crucial this component is to the rover, having it overbuilt would ensure the pivot bar would remain strong enough for any force it may encounter.

Figure 39: The distribution of von-Mises stresses the pivot bar experiences when a force is applied backwards, and the ends are fixed in place.
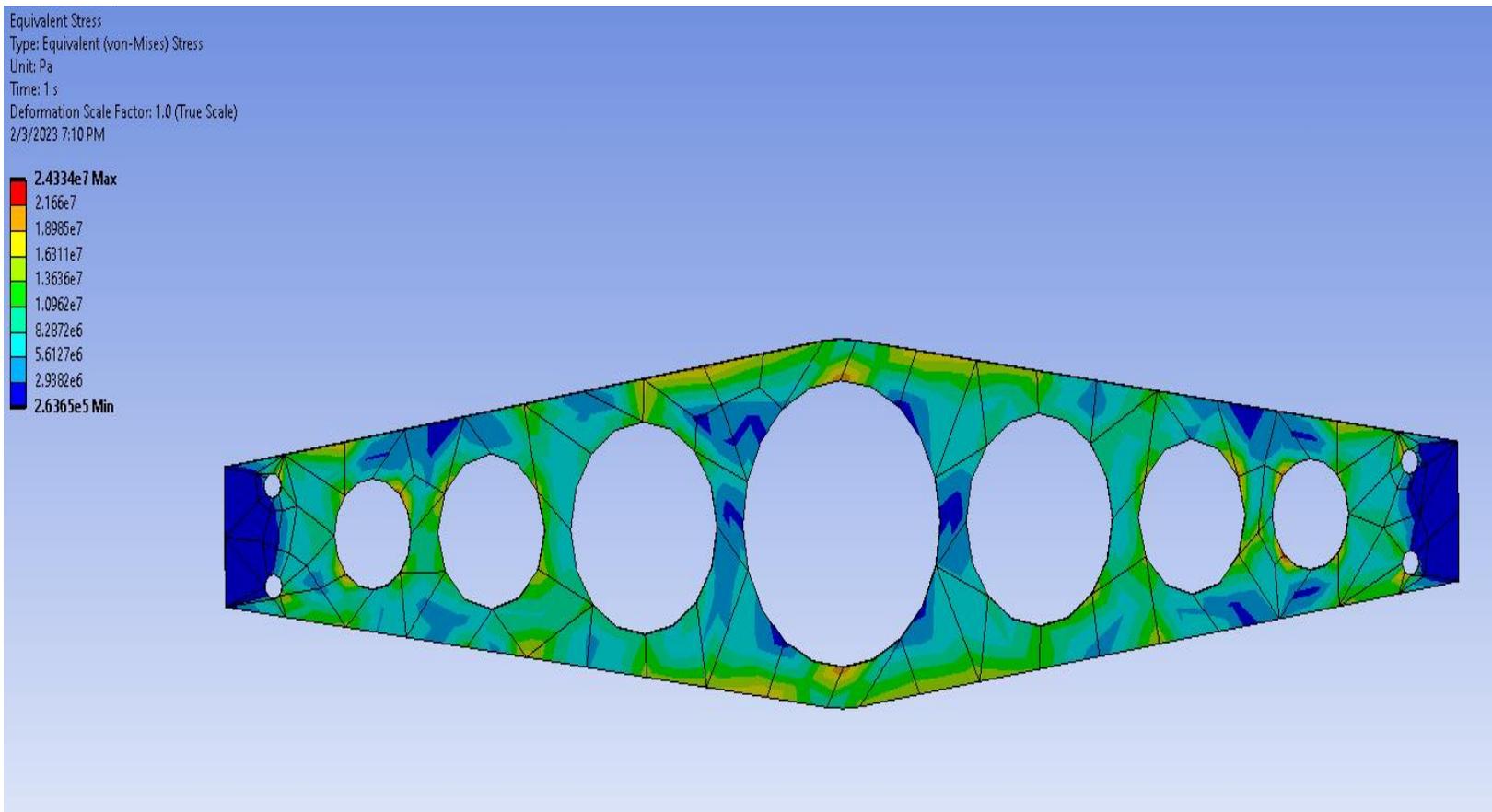
5.2.6 Chassis - Pivot Analysis

The pivot-chassis static simulation referred to the main bearing and axel that houses the pivot bar shown above. This axle runs through the bottom and top plates of the main chassis and is located toward the back of the micro rover chassis. Like the pivot simulation, the strength of the pivot axel was tested to show its interaction with the chassis under a 200 N applied force. The main pivoting tubes on the chassis were selected as fixed, which when combined with the direction of the applied force, the pivot axel would experience a motion like that of pulling a hand lever downwards. This simulation needed to display the distribution of stresses, and the amount of deformation that occurred on the pivot axel. If this axle were to deform too much, it could potentially cause the wheels to lock into place, meaning the micro rover would only be able to traverse relatively flat surfaces with its skid drive. Similarly, if too much stress occurred at this location and caused the axel to snap, the micro rover would suffer a similar fate to what was mentioned with the potential hazards in the pivot.

The simulation results generated the stresses associated with this given scenario as shown in Figure 40. Overall, the stress created an elliptical-shaped distribution ranging from 26.377 MPa to 35.116 MPa with the higher value being located near the pivot axle itself. The distribution shape also extended to the closest inner screws, on the top plate of the chassis. Although the simulation displayed a maximum von-Mises stress of 79.011 MPa, this value cannot be located within the subassembly model. Even after the simulation was re-conducted, this value was still generated but provided no location as to where it was.

Figure 40: The distribution of von-Mise stresses on the axle connecting the pivot bar to the chassis when under an applied force pulling backwards and the inner tubes fixed in place.
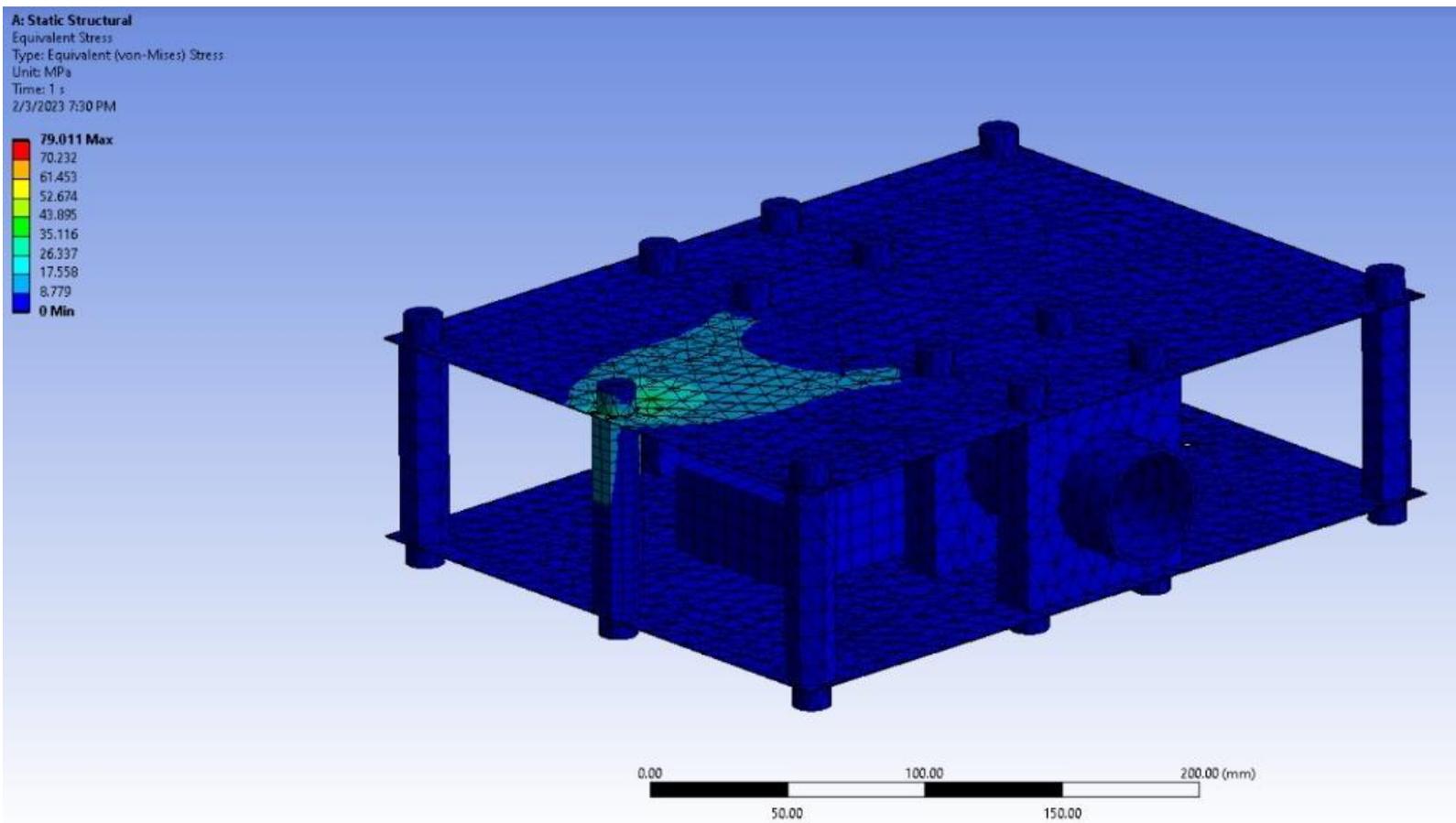
As a result, the maximum stress this component on the subassembly would experience was declared to be 35.116 MPa. The total deformation of the chassis that would occur near the pivot axel is shown in Figure 41. Primarily, the distribution of deformation is even, with a higher concentration being located near the axel itself as expected. The maximum amount of deformation generated occurred towards the top of the axel, but it is only a value of 0.03767 mm. The surrounding area near the axel pivot deformed a range from 0.00837 mm to 0.02511 mm. As a result, no complications from this deformation would occur at the pivot axel when exposed to a force of this magnitude.

Figure 41: The distribution of deformation on the axle connecting the pivot bar to the chassis when under an applied force pulling backwards and the inner tubes fixed in place.
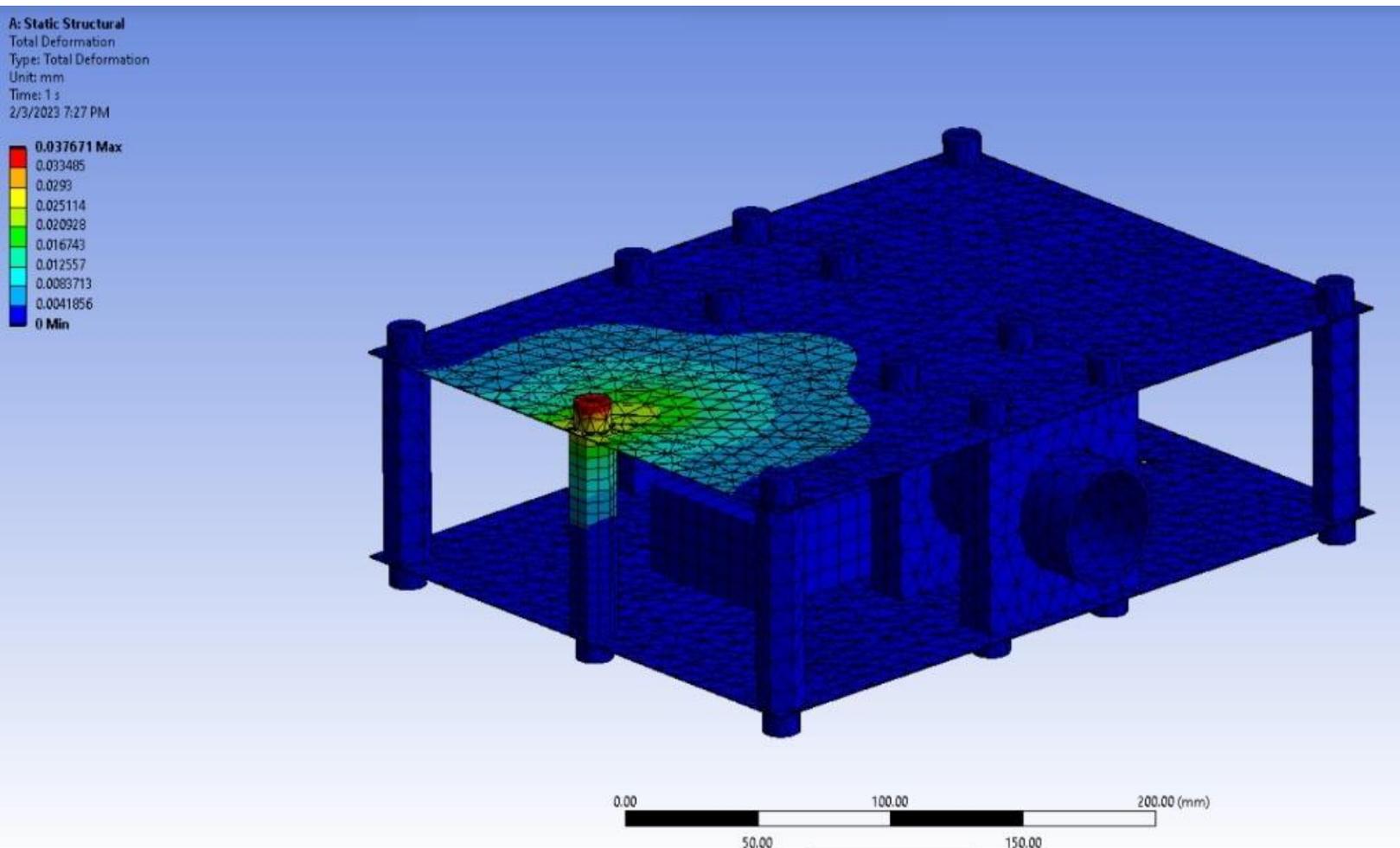
Overall, every major subassembly that was simulated provided enough information to justify the micro rover design as a success. All subassemblies experienced stresses that were below, or just over the yield stress value of 47,500 psi or approximately 327.5 MPa. The factor of safety validated how much stronger the subassembly was for the given simulation scenario, as an example, if the factor of safety

was 2, it meant the component was 2 times stronger than needed for that simulation. The subassembly simulations involving deformation showed that little to no deformation would occur on all components. Even the highest amount of deformation wouldn't impact the functionality of the micro rover as it traversed the lunar environment. The only complications it would cause are the effectiveness of the mechanical components.

5.3 Thermal Analysis

As seen with some of the past rover designs researched, thermal regulation is an important aspect in keeping the internal electronics of a rover operating. Most sensors have a range of temperatures in which they remain operable. If the internal sensor temperature exceeded the maximum or goes below the minimum specified values, failure, and even possible damage may occur. The temperature ranges of every electrical component on the micro rover are shown in Table 3. The Moon has an average temperature range of 120 to -130 °C, and because of this, the level of heating needed for the micro rover's survival was tailored to the electrical component with the least amount of survivability in the cold.

Table 3: Temperature ranges for electrical components selected for the micro rover.

Component	Minimum active temperature (°C)	Maximum active temperature (°C)
Battery	-20	60
Camera	-50	85
Motor	-20	60
Encoder	-30	110
Microcontroller	-40	85

The micro rover design opted to use a combination of an active and passive heating system to regulate the internal temperature. For the passive heating system, the main chassis was wrapped in multilayer insulation (MLI) composed of layers of aluminized polyester film. The polyester MLI has a temperature regulation capability of -250 to 150°C and is specialized in thermal regulation for cryogenic conditions in a vacuum [21]. The MLI works by limiting the amount of heat transfer because of the multiple layers

of reflectors and spacer materials interwoven within the material. It is worth noting that heat in a vacuum is only transferred via surface-to-surface contact radiation instead of transferring via convection. The active heating system consisted of Adhesive Polyimide Heater Plates strips that turn on for a specified amount of time and have a heating capability of 100°C [20]. The active heating solution drew an additional 50,000 $\frac{mW}{h}$ current from the power system when initiated for heating. This brought the total power drawn from the electrical system to be 58,408.71 $\frac{mW}{h}$. If the MLI creates a perfectly sealed interior for heat to radiate from surface to surface, the average heat value generated between the heating sensors was equal to 318,863.16 J. Additionally, the total power consumption of the entire electrical components in tandem with the heat sensors generated power of 3504.52 W. This resulted in the internal temperature of the chassis being brought to -20°C from a starting temperature of -130°C in approximately 90.98 seconds. The heating can remain active for a total of 1.9 hours out of 13 hours before the battery within the micro rover needed to be recharged. This calculation used the following equations:

$$Q = mc\Delta T \quad (1)$$

$$t = \frac{Q}{P} \quad (2)$$

Equation 1 calculated the heat generated by the active and passive heating systems and then was implemented into Equation 2 to calculate the time needed for the sensors to activate to increase the chassis body temperature. The value used in the equations were as follows: $m = 4.6012\ kg$ as the mass of the micro rover, $c = 630\ \frac{J}{kg-K}$ as the approximate specific heat of Aluminum 6061 at 143 K, $\Delta T = 110\ K$ as the change in temperature from 253 K to 143 K, then lastly $P = 3504.52$ W as the total power drawn from the system when heating is activated. Theoretically, using both the active and passive heating systems in tandem should provide the micro rover with enough heat to operate under frigid conditions.

5.4 PID control in a 2D environment

To fine-tune the PID parameters for the control of the differential drive vehicle, a simulation was created in the RVIZ program of Robot Operating System (ROS). This simulation utilized a premade differential drive robot or "turtlebot" as well as a system of publishers and subscribers to estimate the current state of the robot, compute the difference to the desired state, and transmit it back to the robot for correction.

These parameters were then fine-tuned using the Simulink auto-tuner. Using these systems, a test was derived for the turtlebot to navigate between four setpoints in a perfect square to test for any inaccuracies or dampening effects.

Figure 42: Results from the differential drive PID simulation within RVIS.
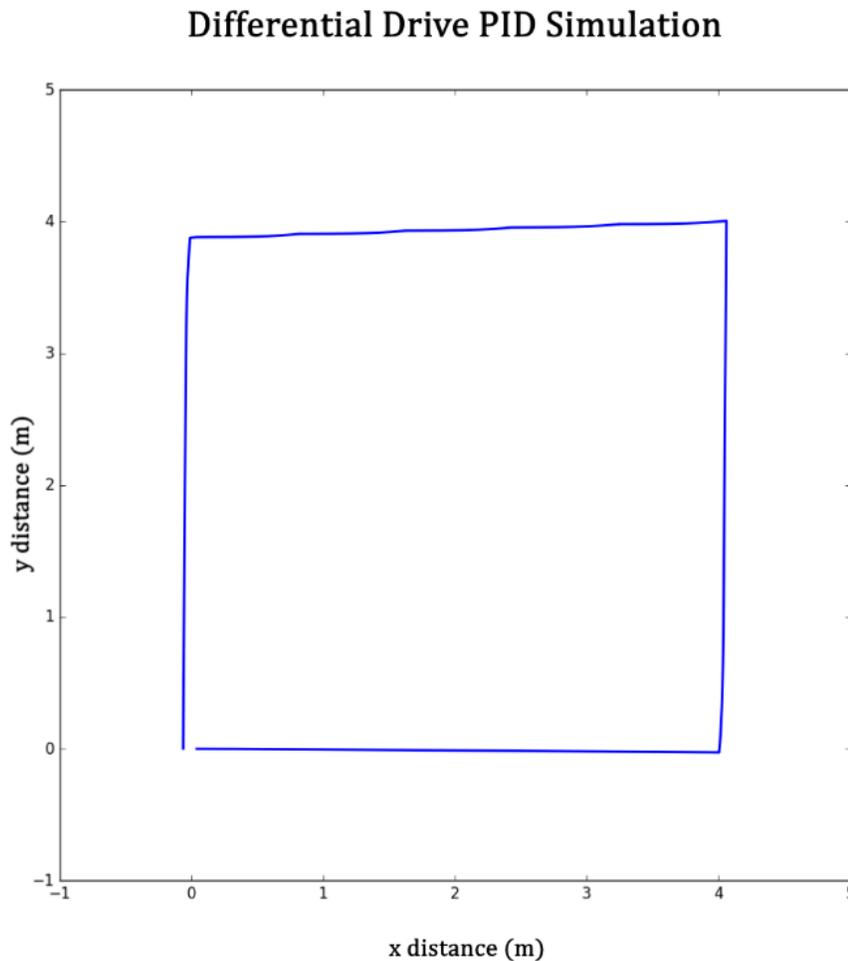
This basic simulation found that the current control system tuning has a small under-dampening effect and slight overshoot that is most apparent in the topmost segment of navigation. Furthermore, as the control system is set up it takes a significant amount of time to traverse between the setpoints, with the entire simulation taking 2 minutes to complete because of effective tuning being accurate up to 0.05 units. As traversal time is not a significant constraint, this completion time was deemed adequate.

5.5 ROS Virtual Environment

After the control simulation, an environmental simulation was created for the robot's rocker bogey system to test how it would traverse a simulated lunar environment. For this purpose, a model of the Apollo 15 landing site in the lunar Hadley Plains was simulated as a virtual environment in the Gazebo simulation software. A model of the fully assembled robot module was placed in it, making sure that lunar environmental conditions such as gravity and a lack of significant atmosphere were accounted for. The robot was then placed on different inclines and tested how it would traverse along the way. A sample of which can be seen in the figure below.

Figure 43: A view of our micro rover within a gazebo simulation depicting the lunar surface.
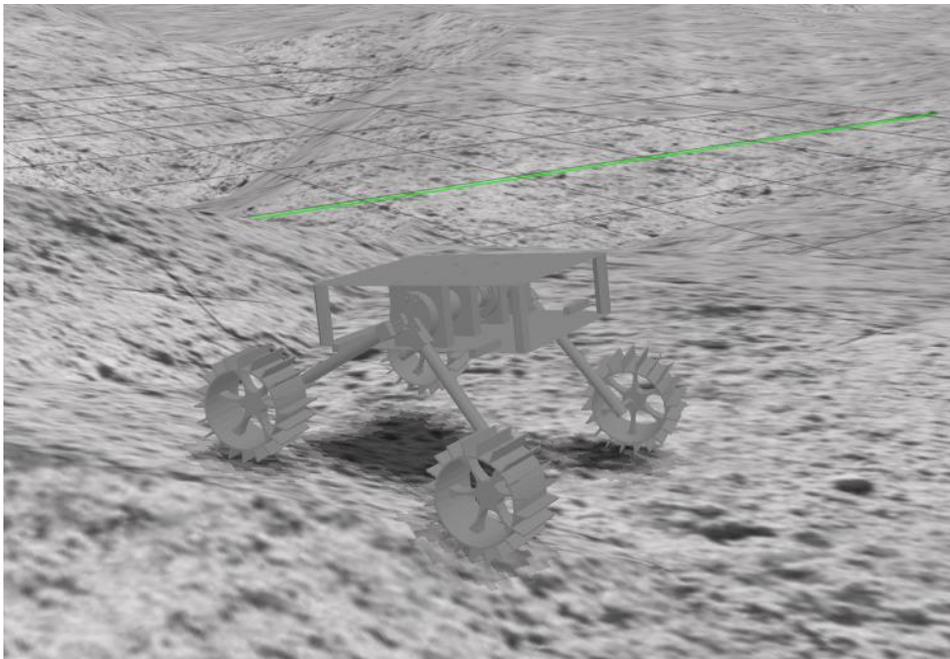
Furthermore, a rudimentary Unified Robot Description Format (URDF) file of the robot was developed, describing its joints and how they move with each other in relation. Then, basic controls of each joint were created, and movement was simulated in RVIZ which can be seen below.

Figure 44: A view of RVIZ simulation parameters in declaring joints on the micro rover model.
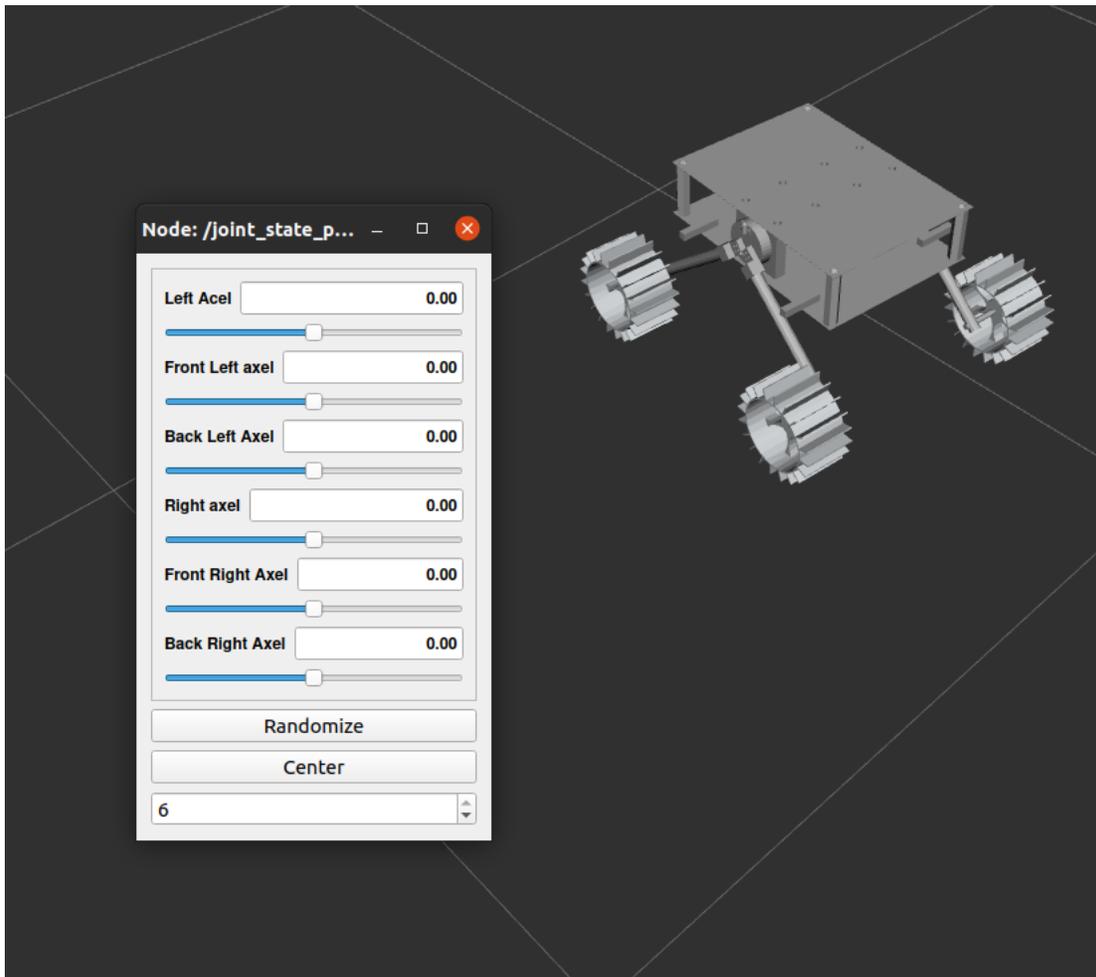
From these results, an understating of the control systems and locomotion of the micro rover was acquired before being built, in addition to a better understanding of how the rover could traverse this hypothetical environment and react to its conditions.

6. Fabrication

6.1 Chassis

The chassis plates were made of two 9" x 12" 2/5 mm thick 6061 aluminum sheets, with holes for 3/8"-16 screws drilled out by hand. Four 3" x 3" x .6" aluminum blocks were milled to house the ball bearings that hold the rocker axles. Additionally, five 3" tall hexagonal standoffs connected the two sheets with additional screws. The aluminum blocks were used in tandem to support the upper and bottom plates.

6.2 Wheel-Leg Assemblies

The two endplates of the wheel legs had a pocket for the rocker axle and had holes for the U-bolts which were milled on a CNC mill. The outer contours of the plates were cut with a bandsaw and then smoothed with a belt sander. The legs were fixed to the endplates with U-bolts that clamp the legs to the end plate itself. A small plate with interior 3 mm threads was bolted to the top of each endplate so one ball joint from the differential linkage could connect to each endplate. The ball bearing holes, gearbox pockets, and fittings for the leg tubes in the motor mounts were also machined using a CNC mill. The outer contours of the motor mounts were cut with a bandsaw and smoothed on using a belt sander. The M3 through holes in the motor mounts were drilled out by hand using a 3D-printed guide.

6.3 Different Linkage

The connecting links of the differential linkage consisted of a threaded rod connecting two off-the-shelf ball-socket joints, which included a screw that connected to the small threaded plates on top of the rocker endplates. The bearing mounting hole and weight-reduction holes of the differential link were cut using a CNC milling machine, and the outer contours were cute with a bandsaw. Then, the component was smoothed with a belt sander.

6.4 Wheels

The design of the wheels was deemed far too complex and expensive to be machined out of the proposed 6061 T6 aluminum. Instead, the wheels were 3D-printed using a carbon-reinforced nylon composite material. The new material, while infeasible for use in cryogenic temperatures, was more than adequate for ground testing on an earth environment.

7. Testing and Performance Evaluation

7.1 Tread Testing

The treading on a wheel is responsible for providing the wheel with traction on any surface it encounters. Some tread designs provide more traction over other tread designs depending on the surface they are driving on. For the micro rover, the tread was designed to be strong and provide the most amount of torque when driving forward. Three primary tread designs were considered: Chevrons, Fins, and Squiggles. The chevron treads were a V-shaped design that are very strong, but also provide a decent amount of grip on the ground. However, the grip on the chevron treading changed depending on the direction the wheel is rotating because of the vertex of the V-shape. The vertex can only point in one direction, leaving the other direction more open. The fin shape was designed as a thin rectangular wall that extended from the wheelbase, similar to how the paddlewheel on a paddle boat is designed. The fins are weaker overall but would provide more torque when pushing forward on the ground because of their larger vertical surface area. Lastly, are the squiggles; an S-shaped design that extended from the wheelbase. They are similar in design characteristics to that of the chevrons in that both designs were strong and provided a decent amount of grip. However, the squiggle tread provided the same amount of traction and torque regardless of which direction the wheel is spinning. The design is symmetrical, with one half of the wheel tread being concave, while the other half is convex. When the wheel changes direction, the half that was originally concave now becomes convex and vice versa.

The selected wheel tread designs were tested for their performance over varying sizes of gravel. The three gravel categories tested included sand with a particle size of 0.06 mm, small gravel with a particle size of 0.2 to 0.5 mm, and lastly, large gravel with a particle size of 12.7 to 19.05 mm. Although the typical lunar regolith is 100 microns in particle size, these gravel sizes showed how effective each tread was under extreme terrain conditions. In addition to the three separate gravel sizes, the tread was varied in length for testing how the grip was affected. Each tread design was tested with a 5 mm, 10 mm, and 15 mm length, and was attached to a testing rig as shown in Figure 45. The testing rig featured a long rod with holes to attach a pull scale that measures in Newtons. The distance between the tension scale and the axle is equal to the radius of the wheel, so the force measured by the scale is the same as the force exerted by the wheel on the ground.

Figure 45: Testing rig designed for measuring the torque of various tread designs in different sizes of gravel.

The testing rig also featured a larger platform towards the back of the pivoting component that allowed a weight to prevent the rig from moving backward as the scale was pulled. Three trials were conducted for each tread design and length at each different size of gravel. A sample of a wheel tread going through each size of gravel is shown in Figure 46.

Figure 46: Example of a tread design's torque being tested in 3 varying sizes of gravel.

For the sake of consistency in the data collection, a single team member was responsible for pulling the scale at a constant rate to the best of their abilities for all the trails. The force displayed on the scale was recorded just before the tread slipped out from its grip in the gravel. Table 4 below shows the results of this experiment in units of newtons.

Table 4: Data table showing the trial results of each tread design's performance in varying sizes of gravel.

Tread Type		Terrain (mm)								
		Sand (5)	Small Gravel (5)	Large Gravel (5)	Sand (10)	Small Gravel (10)	Large Gravel (10)	Sand (15)	Small Gravel (15)	Large Gravel (15)
Trial 1 (N)	Fins	2	2	1.5	4	3	2.5	5	3.5	2
	Chevron	2	1	1	3.5	3	2.5	4	3	2
	Squiggle	2.5	2	1.5	3.5	3	2.5	4.5	3.5	2
Trial 2 (N)	Fins	1.5	1.5	1	2.5	3.5	2.5	4.5	3	2.5
	Chevron	1.5	1	1	4	3.5	2	3.5	2.5	2.5
	Squiggle	2	2	1.5	3.5	4	2.5	5	3.5	3.5

Trial 3 (N)	Fins	2	1.5	1.5	3	3	3	4.5	2.5	2
	Chevron	2	1	1.5	3.5	3	2.5	3.5	3	2.5
	Squiggle	2.5	2	2.5	3.5	3.5	2.5	4.5	3	2.5

For the most part, every tread design had the same basic trend. The larger particle sizes result in lower values of grip, and torque produced by each tread. Additionally, it was found that as the length of the tread increases, so does the amount of torque generated. A further breakdown of this data is shown in Table 5 below by showing the average value of all three trials under each column. According to the averaged values, the squiggle tread design produced more torque in almost every test conducted compared to the fins and chevrons. Of the three designs, the chevrons appeared to have generated the lowest torque overall, with the fins generating the 2nd most torque. In terms of selecting tread length, the squiggles with 15 mm length have a higher torque generation overall compared to the 10 and 5mm length variants. With all the testing data, the S-shaped squiggles are the selected tread design for the micro rover wheels. This is because it offered the most amount of grip on almost any type of surface the micro rover could encounter on the lunar surface.

Table 5: Average performance values from the varying tread designs testing trials.

Tread Type		Terrain (mm)								
		Sand (5)	Small Gravel (5)	Large Gravel (5)	Sand (10)	Small Gravel (10)	Large Gravel (10)	Sand (15)	Small Gravel (15)	Large Gravel (15)
Pull Scale Averages (N)	Fins	1.83	1.67	1.33	3.16	3.16	2.67	4.67	3	2.16
	Chevron	1.83	1	1.16	3.67	3.16	2.33	3.66	2.83	2.33
	Squiggle	2.33	2	1.83	3.5	3.5	2.5	4.67	3.34	2.67

7.2 Lunar Regolith Simulation

The permanently shadowed lunar polar regions are classified as some of the oldest lunar highlands. While typical lunar regolith has a mean grain size of ∼100 μm, with ∼10% of the material smaller than 10 μm, the polar regions have been found to have been subjected to intense meteorological bombardment. As a result, the upper layer of the regolith in these regions may be much finer-grained than the typical regolith. To test the traction capabilities of the lunar micro rover in these regions, it was essential to find an appropriate analog with grain size ranging from 20-100 micrometers.

To fully assess the potential long-term interactions of a finalized design with the lunar surface, it would be necessary to utilize a more suitable wheel material along with a regolith analog that closely replicates both the physical and chemical composition of the lunar surface. This would provide a more accurate representation of the potential performance of the design in a real-world setting. Since the design of the lunar rover is preliminary, there is no need to replicate the specific chemical composition of the lunar surface when utilizing carbon fiber 3D-printed wheels.

Initially, garnet sand and pool filter sand were selected as simulants for lunar regolith to test the mobility capabilities of the lunar micro rover. Both materials have similar physical properties to the lunar regolith, having a similar grain size distribution ranging from 40-100 microns. Garnet sand has been used before as a regolith simulant specifically in SSC-2 designed for hardware testing and micro rover trafficability and slope climbing capabilities. Additionally, they are readily available materials and are relatively inexpensive. However, an additional alternative needed to be found due to supply chain issues and the non-delivery of the aforementioned purchased materials. Ultimately, flour was utilized as a regolith analog due to budget, and it is a readily available material. This flour still roughly met the requirements mentioned above, as it was estimated to have a grain size between 50-200 μm.

7.3 Drivetrain Test

The first test performed on the prototype was a test of the drivetrain. A plastic underlayer was laid over a flat surface, then bricks were laid on either side, creating a lane approximately one meter wide and two meters long. This lane was then filled with flour until it had a depth of over two inches in all locations. The lunar micro rover was then placed with all wheels on the flour and manually given the

command to move forward. The rover successfully traversed to the end of the lane. Upon successful completion, the rover was commanded to reverse the full length of the lane and did so successfully.

Figure 47: Setup of initial drivetrain test where the micro rover drives forward in the flour mimicking lunar dust.

Next, a few minor obstacles were added to the rover's path. These consisted of small rocks collected from the surrounding environment. These rocks were meant to provide only the most basic resistance to the rover and were not meant to stress the system in any way. They merely served as verification that more harsh testing could continue without modification to the existing design of the rover. Once the rocks and rover were introduced to the testing environment, the same command to move forward was given. The rover again moved forward through the length of the lane, then back again.

Figure 48: Setup of secondary drivetrain test where the micro rover will traverse small rocks within the flour mimicking lunar dust.

Figure 49: The micro rover navigating the secondary drivetrain test mid-traversal over a small rock.

After the successful navigation of both the initial and secondary drivetrain test, a third, and final test was required to ensure the stability of the drivetrain before moving on to more difficult tests. This final test saw the addition of two bricks laid side by side in front of one of the wheels, with the intent of forcing the Rocker-Bogie system to actuate. Once again, the rover traversed the obstacle successfully.

Figure 50: Setup of tertiary drivetrain test where the micro rover is to climb over bricks on the side, while the other side will have to climb over stacked rocks placed within the flour mimicking lunar dust.

7.4 Drop Test

The drop test was designed to simulate the initial deployment of the rover from a lander. The drop test was conducted slightly above 4 inches. Though it is acknowledged that the drop from a lander to the lunar surface would exceed 4 inches, it would take place with lunar gravity. 4 inches (.102 meters) in Earth's gravity was found to be equivalent to a 2-foot (.61 meters) drop on the Moon. The test was also conducted to verify the simulations conducted via Ansys, as discussed in a previous section.

$$t = \sqrt{\frac{2h}{g}}, \quad v(t) = gt + v_0$$

$$On\ Earth: \quad t = \sqrt{\frac{2*.102}{9.8}} = 1.44\ s, \quad v(.144) = 9.8*.144 = 1.41\ ^m/_s$$

$$On\ the\ moon: \quad t = \sqrt{\frac{2*.61}{1.6}} = .873\ s, \quad v(.873) = 1.6*.873 = 1.40\ ^m/_s$$

Figure 51: Setup of the drop test conducted on the micro rover to test its survivability of deployment on the Moon.

The rover was held at the desired height and released. Upon impacting the ground, the rover was given the command to move forward. The rover was able to drive away successfully, surviving the drop test. Sensors were not used to measure the strains on all the components of the rover mentioned in the analysis. Rather, this was a pass/fail test. Though the exact values of the stresses found in the simulations cannot be verified without further testing and equipment, the result that the rover would survive the test was validated.

7.5 Slope and Step Test

The rover's ability to effectively climb up a slope is very important since the rover is to be going in and out of craters on the moon. To test the capabilities, the rover was subjected to a small-scale slope test where a brick was placed at an angle of approximately 35°. This angle was selected from looking at previously developed lunar rovers, which had max slope climb angle between 18-35° [3]. While this test was completed on brick the team has confidence in the ability to similarly replicate this on the lunar regolith.

Figure 52: The micro rover climbing up an incline made from bricks to test the drivetrain's torque and grip when climbing.

The rover was also tested to see the max step obstacle size it could traverse. For this test, bricks were stacked to replicate a set of stairs. The rover was able to climb up the bricks giving the team confidence in its ability to easily traverse over small obstacles that it may face on the moon.

Figure 53: The micro rover climbing up a set of stairs made from bricks to test the drivetrain's torque and grip when climbing.

8. Future Work

Many additional factors beyond the scope of this paper must be considered for a complete micro rover mission, such as the communication capabilities the rover may have, how it is transported to its destination, and the deployment procedure of the rover. Of the past projects reviewed, only Virginia Tech's micro rover went into the details about communication, the lander, and transportation. The proposed rovers each have two antennas for communication using the Deep Space Network connected via a relay satellite in lunar orbit. The relay satellite was proposed to inhabit an orbit that passes over the polar regions of the moon, allowing the satellite to communicate with the rovers for 35 minutes before passing below the horizon [2]. The orbit itself took approximately 150 minutes to reposition above the micro rover for communication [2].

The lander used for Virginia Tech's mission was constructed using aluminum walls, doors, legs, and a bed designed to be both "protective and lightweight" [2]. The general design consisted of four legs connected to the housing portion of the micro rover, with landing pads attached at the bottom of each leg, and struts to support the legs' connection to the main body [2]. For temperature regulation, avionic instruments were mounted near the propulsion system radiator on one of the lander's walls. The propulsion system of the lander uses two R-40B engines and two tanks that rely on hypergolic fuel and oxidizers [2]. It was found that liquid propulsion proved best for the mission, as solid and electric propulsion systems were excluded due to the ΔV and impulse requirements. To ensure a safe landing, avionics components were added to the structure of the lander. At the ceiling of the rover compartment, there was an IMU, five-course sun sensors on the walls, three control-mounted gyroscopes, and six thrusters [2]. Upon landing, the lander would then deploy a ramp for the rover to drive off for successful deployment on the surface.

The orbiter and its design were also critical to the mission plan. The orbiter would serve as a transporter and a lander to place the rover payload on the surface of the moon but would also send communications between Earth and the rover. The orbiter was a cylindrical shape with solar panels, being that the orbiter's main power source is solar energy [2]. The propulsion system used by the orbiter is the same liquid hypergolic fuel and oxidizer as mentioned in the lander, as the high ISP of the bipropellant made it more favorable [2]. The communication system of the orbiter consisted of two small quadrivial helix antennas, an S-band dish antenna, and three transponders connected to the S-band power amplifier [2].

93

The communication system took advantage of BPSK modulation and was engineered for all the antennas to communicate with the rover and send the data back to Earth [2]. Lastly, the orbiter featured a star tracker that in conjunction with an attitude control system kept a low slew rate and low altitude error. Four sun sensors assist the star tracker if the slew rate needed to be reduced, while an IMU measured the rotational velocity allowing the precise attitude to be determined [2]. Building a mission plan with supporting infrastructure such as a lander or orbiter is equally as vital for the creation of a micro rover project. The supporting infrastructure could expand into details that can affect the overall design, deployment procedure, or overall mission plan.

Due to the limited time and budget of the project, there were some ways that the project could have been expanded upon but was not. There was an intention to complete thermal analysis on the rover design, however, there were problems with the generated simulation outputs reported after every test. Ansys Workbench 2022 was used to simulate the scenario of how the heat would be distributed primarily in the chassis in -130°C lunar temperature. However, the simulation was unsuccessful in providing accurate results. As mentioned, Ansys had a steep learning curve when it came to using the software for static purposes. For thermal purposes, it was even harder for a simulation to get properly running. A modified assembly was created, shown in Figure 54, to mimic the behavior of the MLI over the rover. Within the simulation, mimic heating sensors within the chassis were selected to generate heat that would radiate from surface to surface. Then, the exterior of the chassis was selected to experience -130°C as mentioned. After a simulation concluded, it was often found that no heat distribution was generated at all. Additionally, some simulations would require 10 hours to solve but would fail after 5 hours of calculating. The simulation parameters assumed the interior had little to no heat loss and would radiate the heat produced by the sensors in surface-to-surface contact, meaning a heat distribution should have been generated in the simulation results. The CAD model was checked for any holes in the event the outside temperature was leaking into the interior, but the CAD model was perfectly enclosed. The thermal simulation testing even went as far as putting the electronics in a simplified box similarly shaped to the chassis. Unfortunately, no valid results were generated every time the simplified simulation was solved.

Figure 54: Modified chassis CAD model for the use of thermal simulations within Ansys Workbench 2022.
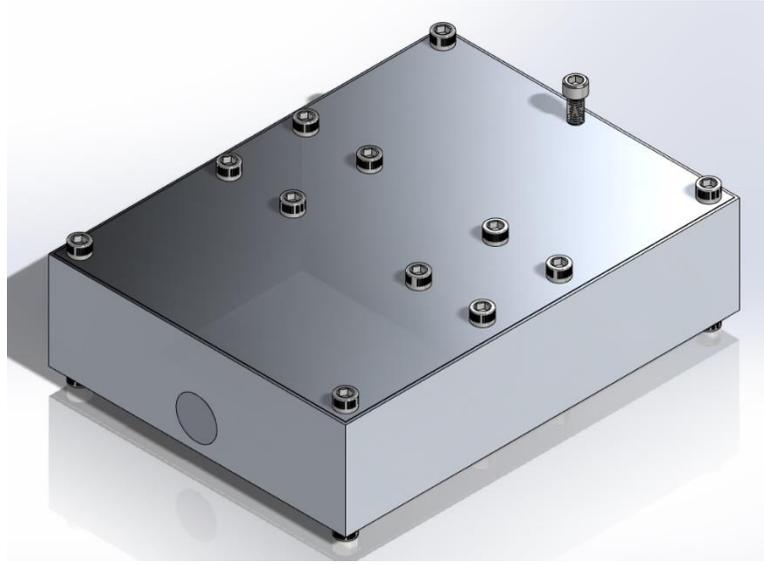
Many online resources were referred to for troubleshooting this issue. The online tutorials for conducting a thermal simulation in Ansys primarily used convection heating instead of radiation. Because the Moon is in a vacuum, convection heating isn't the primary way for heat to be transferred, resulting in only looking for online resources that used radiation. Despite even looking at the online resources involving only radiation heating, the thermal simulation still ran into the same issue of no heat being shown as properly distributed. Although no valid thermal simulation results were generated, it is fully acknowledged that simulated thermal analysis must be done to maximize the efficiency of the heating systems for a rover. However, the sensors selected should provide more than enough heat for the chassis to operate on the lunar surface in tandem with the MLI despite the failure of the Ansys thermal simulations.

There was considerable difficulty in feeding IMU and GPS data into the EKF algorithm when concerning the software of the micro rover. The relatively low sample rate of the rover's sensors when compared to state-of-the-art counterparts resulted in suboptimal noise reduction and an inability to estimate position while estimating attitude fared better. Additionally, difficulty in data communication between different functions of the autonomy architecture resulted in an inability to achieve full autonomy. Still, each independent autonomy function was verified either through testing onboard the

rover or simulated testing in the ROS environment. Significant further work is possible in integrating these functions into full autonomous capability for the rover.

9. Broader Impacts

The significance of this project and the choices made by the team goes beyond the raw engineering of the rover. Engineers have a responsibility to consider the broader impacts their projects may have and the stakeholders that may be affected by the project.

9.1 Stakeholders

The fact that the mission does not have a specific scientific goal means that the stakeholders of the mission would change depending on the scientific research done. For example, scientists that may be tasked with working with samples brought back by the mission could be impacted negatively if the scientific mission does not meet its goals. Based on the discoveries made by the mission, there could be an impact on the general community interested in the research conducted on the Moon. However, this could also spur a new wave of interest in space travel, or it could cause doubt and fear throughout the general population. These impacts could span from citizens to scientists to professionals and larger figures. The discoveries made by the mission could impact the modern space race for better or for worse. This would bring in stakeholders such as the involved countries' governments, militaries, and citizens. In addition, if the mission experiences a faulty landing and does not end up in the ocean, this brings in stakeholders that populations of people close to the impact location of the rover upon reentry. In a more specific sense, the mission's success would affect the stakeholders in any companies contracted to complete this mission and the companies themselves.

9.2 Other Considerations

Considering environmental impacts while participating in the aerospace industry is essential as the industry has large and costly impacts on the environment. The team acknowledges the need to limit environmental impacts whenever possible. This includes impacts from fuel and launch vehicles used during launch, space debris that could be created by the mission, and damage that could be done to flora and fauna located at launch and reentry locations. For example, the team considered the environmental impacts of manufacturing parts versus buying commercial-off-the-shelf components. By buying commercial-off-the-shelf parts, the team does not know how the parts were manufactured or the impact that the manufacturing process may have had on the environment. Therefore, wherever plausible based on time and budget constraints, the team manufactured parts to monitor possible impacts.

Considering the long-term goal of creating many of the designed rovers to work together in a swarm, the team's design sees economic benefits as these robots can be made at low-cost and in high quantity to cover a larger area. If these rovers were operating in the same location, not much additional support infrastructure such as base stations are required relative to the number of rovers operating. This larger coverage would allow for more scientific data to be collected and analyzed at a lower cost, presenting desirable economies of scale for this rover's design and mission architecture.

10. Conclusion

Ultimately, the final micro rover designed and fabricated in this project met several of the initial goals. The preliminary design choices made by both the electrical and mechanical sub-teams were made possible through research on relevant past micro rover projects. Prominent mechanical design restrictions included the overall weight of the rover, obstacle size, and material behavior in extreme lunar cryogenic temperatures. The most prominent electrical design considerations included the minimization of subsystem masses and power consumption, modular autonomous navigational functions, and data collection through sensors. When designing the final micro rover, all the above factors were considered and tested in both a theoretical and practical capacity. Although the micro rover did not achieve some of the preliminary goals and simulation data, a foundation has been established for future MQP teams to improve upon the micro rover's design and analysis procedures. Ultimately, the hope is that this micro rover will contribute to the further exploration of the Moon's polar surfaces through the advancement of micro rover technology.

References

[1] Sank, Jeffrey, and John H. Scott. "Power and Energy for the Lunar Surface." National Aeronautics and Space Administration, 29 Apr. 2022, https://ntrs.nasa.gov/api/citations/20220005893/downloads/Power%20and%20Energy%20for%20the%20Lunar%20Surface.pdf.

[2] Quinn, Alison. "AIAA Home." *Project Penguin*, Virginia Polytechnic Institute & State University, 2018, www.aiaa.org/docs/default-source/uploadedfiles/education-and-careers/university-students/design-competitions/1stplace_virginia_tech_space_design.pdf?sfvrsn=59cff8b5_0.

[3] Schweitzer, Lydia. "Micro Rover Mission for Measuring Lunar Polar Ice." *IEEE Xplore*, Carnegie Mellon University, 2022, ieeexplore.ieee.org/Xplore/dynhome.jsp.

[4] Akinyele, Jesulona. *Worcester Polytechnic Institute*, 26 May 2022, www.wpi.edu/news/can-you-dig-it-wpi-student-team-takes-nasa-mining-challenge.

[5] Cunningham, Andrew. "Inspection and Reconnaissance Micro-Rover for Use in Extraterrestrial Environments." *Worcester Polytechnic Institute*, 25 Apr. 2013, web.wpi.edu/Pubs/E-project/Available/E-project-042513-103357/.

[6] Arm, Phillip. "SpaceBok: A Dynamic Legged Robot for Space Exploration | IEEE ..." *SpaceBok: A Dynamic Legged Robot for Space Exploration*, IEEE, 2019, ieeexplore.ieee.org/document/8794136/.

[7] Kawashima, Nobuki, and Kazuya Take. "Laser Energy Transmission for a Wireless Energy Supply to Robots." *Robotics and Automation in Construction*, 2008, doi:10.5772/6194.

[8] Wilson, J. W., et al. "Radiation Exposure in the Moon Environment." NASA/ADS, Harvard University, 29 Nov. 2011, https://ui.adsabs.harvard.edu/abs/2011LPICo1667.4016W/abstract.

[9] R.M, Paulo. "Thermal Modeling and Design of a Micro-Rover for Lunar Polar ... - USRA." *i-SAIRAS2020-Papers*, Carnegie Mellon University, 19 Oct. 2020, www.hou.usra.edu/meetings/isairas2020fullpapers/pdf/5058.pdf.

[10] Sheperd, Steve. "Design and Management Guide for Electrical Systems for Space." NASA Electronic Parts and Packaging (NEPP), 2017, https://nepp.nasa.gov/docuploads/D41D389D-04D4-4710-BBCFF24F4529B3B3/Dmg_Space-00.pdf.

[11] Kaufman, Marc. "Full Moon's Electric Charge Can Affect Space Weather." National Geographic, National Geographic Society, 18 Nov. 2010,

https://www.nationalgeographic.com/science/article/101118-science-space-full-moon-electric-charge#:~:text=The%20biggest%20hazards%20of%20an,lead%20to%20unexpected%20electrical%20discharges.

[12] Stanford University School of Engineering. "How Do We Build Electronic Materials That Can Survive Radiation?" Stanford University, 20 Apr. 2017, https://engineering.stanford.edu/magazine/article/how-do-we-build-electronic-materials-can-survive-radiation.

[13] NASA. "NASA's Coating Technology Could Help Resolve Lunar Dust Challenge." NASA, 4 Aug. 2020, https://www.nasa.gov/feature/langley/nasa-s-coating-technology-could-help-resolve-lunar-dust-challenge.

[14] Ashford, Bill. "The Temperature Ratings of Electronic Parts." Electronics Cooling, 1 Feb. 2004, https://www.electronics-cooling.com/2004/02/the-temperature-ratings-of-electronic-parts/.

[15] Curtis, Howard D. "Orbital Mechanics for Engineering Students." *ScienceDirect*, Elsevier Ltd, 2020, www.sciencedirect.com/book/9780081021330/orbital-mechanics-for-engineering-students. Chapters 2, 6, 8, and 9

[16] Bate, Roger. *Fundamentals of Astrodynamics: Second Edition*. Dover Books on Physics, 2015.

[17] Karur, Karthik, et al. "A Survey of Path Planning Algorithms for Mobile Robots." *Vehicles*, vol. 3, no. 3, Aug. 2021, pp. 448–68. https://doi.org/10.3390/vehicles3030027.

[18] Cowlagi, Raghvendra. (2011). Hierarchical Motion Planning for Autonomous Aerial and Terrestrial Vehicles.

[19] Noreen. "A Comparison of RRT, RRT* and RRT*-Smart Path Planning Algorithms." *International journal of computer science and network security: IJCSNS*. 16.10 (2016): n. pag. Print.

[20] ublox, "NEO-6 u-blox 6 GPS Modules," GPS.G6-HW-09005-E data sheet, 12 May 2011, https://content.u-blox.com/sites/default/files/products/documents/NEO-6_DataSheet_%28GPS.G6-HW-09005%29.pdf.

[21] TDK InvenSense, "ICM-20948 World's Lowest Power 9-Axis MEMS MotionTracking™ Device" DS-000189 data sheet, 2 Jun. 2017, https://cdn.sparkfun.com/assets/7/f/e/c/d/DS-000189-ICM-20948-v1.3.pdf.

[22] Kurokesu, "C1 PRO INDUSTRIAL USB CAMERA" Data Sheet, 7 Jun. 2021, https://kurokesu.com/uploads/doc/C1-PRO/Kurokesu_c1-pro_%2329.pdf.

[23] "Arducam 4-12mm Varifocal C-Mount Lens for Raspberry Pi HQ Camera, with C-Cs Adapter." *Arducam*, 13 Nov. 2020, www.arducam.com/product/arducam-4-12mm-varifocal-c-mount-lens-for-raspberry-pi-hq-camera-with-c-cs-adapter/.

[24] "Pololu - 488:1 Metal Gearmotor 20Dx46L Mm 12V CB with Extended Motor Shaft." *Pololu Robotics & Electronics*, www.pololu.com/product/3497.

[25] "Pololu - Magnetic Encoder Pair Kit for 20D mm Metal Gearmotors, 20 CPR, 2.7-18V" *Pololu Robotics & Electronics*, www.pololu.com/product/3499.

Appendices

Appendix A: Mission Planning Calculations and Code

In this MQP, a lunar rover and communications module from Earth is sent as the payload of a multistage unmanned rocket to the southern polar region of the Moon through controlled flight. No other parameters are given or constrained beyond design and weight of the rover, so a mission plan is devised in several phases that keeps delta-v to a minimum.

Launch window and lead angle correlate to when the Moon is approaching its perigee with the Earth, which occurs around the Supermoons, giving several opportunities for launch. Basic maneuvers of the mission involve a series of Hohmann transfers and other timed boosts for lunar capture and escape as well as rover release and recovery.

In[229]:=

Mission Plan
Basic Details of Earth Heliocentric Orbit and Lunar Geocentric Orbit (in two subparts)
Geocentric Hohmann Transfer 1 (Surface to LEO, Phase I)
Geocentric (Cislunar) Hohmann Transfer 2 plus Inclination Change (LEO to Lunar SOI, Phase II)
Capture (Lunar SOI to LMO, Phase III)
Rover Release (LMO to Low Perilune Orbit, Phase IV)
Rover Return (Low Perilune Orbit to LMO, Phase V)
Lunar Escape (LMO to Lunar SOI, Phase VI)
Geocentric Hohmann Transfer 3 (Lunar SOI to LEO, Phase VII)
Earth Capture plus Inclination Change and Reentry (LEO to Surface, Phase VIII)

In[230]:=

---

0. Basic Details of Earth Heliocentric Orbit and Lunar Geocentric Orbit
The orbital velocity of the Earth about the Sun and the Moon about the Earth is computed along with the Earth and Moon SOI radii.

0a. Earth Heliocentric Orbit (Earth/Sun)
Std. Grav. Parameters

In[231]:=
muS=1.327124400189×10^20;(* Sun, m^3/s^2 *)

In[232]:=
mu=3.986004418×10^14;(* Earth, m^3/s^2 *)

In[233]:=
muM=4.90486959×10^12;(* Moon, m^3/s^2 *) Body Masses / Radii

In[234]:=
mSun=1.9885634719459146×10^30;(* kg *)

In[235]:=
mEarth=5.972168×10^24;(* kg *)

In[236]:=
mMoon=7.34767309×10^22;(* kg *)

In[237]:=
RE=6378.1370×1000;(* m *)

In[238]:=
RM=1737.4×1000;(* m *)
Earth SOI

In[239]:=
aEorbS=149.60×10^6×1000(* m *)
Out[239]=
$1.496×10^{11}$
In[240]:=
rSOIE=aEorbS(mEarth/mSun)^(2/5)(* m *)
Out[240]=
$9.24631×10^8$

Heliocentric Orbital Parameters (Ellipse)

In[241]:=
eEorbS=0.0167086(* unitless, almost circular *)
Out[241]=
0.0167086
In[242]:=
rEorbSp=aEorbS(1-eEorbS)(* m *)
Out[242]=
$1.471×10^{11}$
In[243]:=
rEorbSa=aEorbS(1+eEorbS)(* m *)
Out[243]=
$1.521×10^{11}$
In[244]:=
epEorbS=-muS/(2aEorbS)(* J/kg *)
Out[244]=
$-4.43558×10^8$
In[245]:=
Verbos=Sqrt[2(epEorbS+muS/rEorbSp)](* m/s *)
Out[245]=
30286.4
In[246]:=
VEorbSa=Sqrt[2(epEorbS+muS/rEorbSa)](* m/s *)
Out[246]=
29290.9
In[247]:=
pEorbS=aEorbS(1-eEorbS^2)(* m *)
Out[247]=
$1.49558×10^{11}$
In[248]:=
hEorbS=Sqrt[pEorbSmuS](* m^2/s *)
Out[248]=
$4.45514×10^{15}$
In[249]:=
TEorbS=2PiSqrt[aEorbS^3/muS]/(60×60×24)(* days *)
Out[249]=
365.265
In[250]:=

iEorbS=7.155Pi/180(* Solar equator plane inclination *)
Out[250]= 0.124878

0b. Lunar Geocentric Orbit (Moon/Earth)

Moon SOI

In[251]:=
aMorbE=384748×1000 //N(* m *)
Out[251]=
3.84748×10^8
In[252]:=
rSOIM=aMorbE(mMoon/mEarth)^(2/5)(* m *)
Out[252]=
6.62496×10^7

Geocentric Orbital Parameters (Ellipse)

In[253]:=
eMorbE=0.0549006(* unitless, almost circular *)
Out[253]=
0.0549006
In[254]:=
rMorbEp=aMorbE(1-eMorbE)(* m *)
Out[254]=
3.63625×10^8
In[255]:=
rMorbEa=aMorbE(1+eMorbE)(* m *)
Out[255]=
4.05871×10^8
In[256]:=
epMorbE=-mu/(2aMorbE)(* J/kg *)
Out[256]=
-518002.
In[257]:=
VMorbEp=Sqrt[2(epMorbE+mu/rMorbEp)](* m/s *)
Out[257]=
1075.34
In[258]:=
VMorbEa=Sqrt[2(epMorbE+mu/rMorbEa)](* m/s *)
Out[258]=
963.416
In[259]:=
pMorbE=aMorbE(1-eMorbE^2)(* m *)
Out[259]=
3.83588×10^8
In[260]:=
hMorbE=Sqrt[pMorbEmu](* m^2/s *)
Out[260]=
3.91022×10^{11}
In[261]:=

TMorbE=2PiSqrt[aMorbE^3/mu]/(60×60×23.9344696)(* days *)
Out[261]=
27.5644
In[262]:=
iMorbE=5.145Pi/180(* Moon/Earth ecliptic plane inclination, rad *)
Out[262]= 0.0897972

---

1. Geocentric Hohmann Transfer 1 (Surface to LEO, Phase I)
Earth LEO (Circular)
In[263]:=
zo=1000×1000;(* m *)
In[264]:=
ro=RE+zo
Out[264]=
$7.37814×10^6$
In[265]:=
epo=-mu/(2ro)(* J/kg *)
Out[265]=
$-2.70123×10^7$
In[266]:=
ho=Sqrt[romu](* m^2/s *)
Out[266]=
$5.42303×10^{10}$
In[267]:=
Vo=Sqrt[mu/ro](* m/s *)
Out[267]= 7350.14
Hohmann Transfer 1 (Surface to LEO)
In[268]:=
rt1p=RE;
In[269]:=
rt1a=ro;
In[270]:=
et1=(rt1a-rt1p)/(rt1a+rt1p)//N(* unitless *)
Out[270]=
0.0726941
In[271]:=
at1=(rt1a+rt1p)/2(* m *)
Out[271]=
$6.87814×10^6$
In[272]:=
pt1=at1(1-et1^2)(* m *)
Out[272]=
$6.84179×10^6$
In[273]:=
ept1=-mu/(2at1)(* J/kg *)
Out[273]=

-2.89759×10^7

In[274]:=

Vt1p=Sqrt[2(ept1+mu/rt1p)](* m/s *)

Out[274]=

8187.66

In[275]:=

Vt1a=Sqrt[2(ept1+mu/rt1a)](* m/s *)

Out[275]=

7077.94

Diagram 1: Hohmann Transfer 1, Surface to LEO

In[276]:=

Apse=Plot[0,{x,-rt1p,rt1a},Frame□True,PlotStyle□{Black,Thickness[0.003]}];
LEO=PolarPlot[ro/(1+0Cos[θ]),{θ,0,2Pi},Frame□True,
PlotStyle□{Green,Thickness[0.003]},AspectRatio□True]; Hohmann1=PolarPlot[pt1/(1-
et1Cos[θ]),{θ,Pi,2Pi},Frame□True, PlotStyle□{Dashed,Gray,Thickness[0.003]},AspectRatio□True];
Surface=PolarPlot[RE/(1+0Cos[θ]),{θ,0,2Pi},Frame□True,
PlotStyle□{Blue,Thickness[0.003]},AspectRatio□True]; Earth=RegionPlot[x^2+y^2≤RE^2,{x,-
2RE,2RE},{y,-2RE,2RE}]; Show[Apse,Earth,Surface,Hohmann1,LEO,
Graphics[{PointSize[0.02],Blue,Point[{RECos[Pi],0}]}],
Graphics[{PointSize[0.02],Black,Point[{0,0}]}],
Graphics[{PointSize[0.02],Green,Point[{roCos[0],roSin[0]}]}], PlotRange□{{-1.1rt1a,1.1rt1a},{-
1.1rt1a,1.1rt1a}}, AspectRatio□True,PlotLabel□"Surface to LEO (via Hohmann 1)"]

Out[281]=
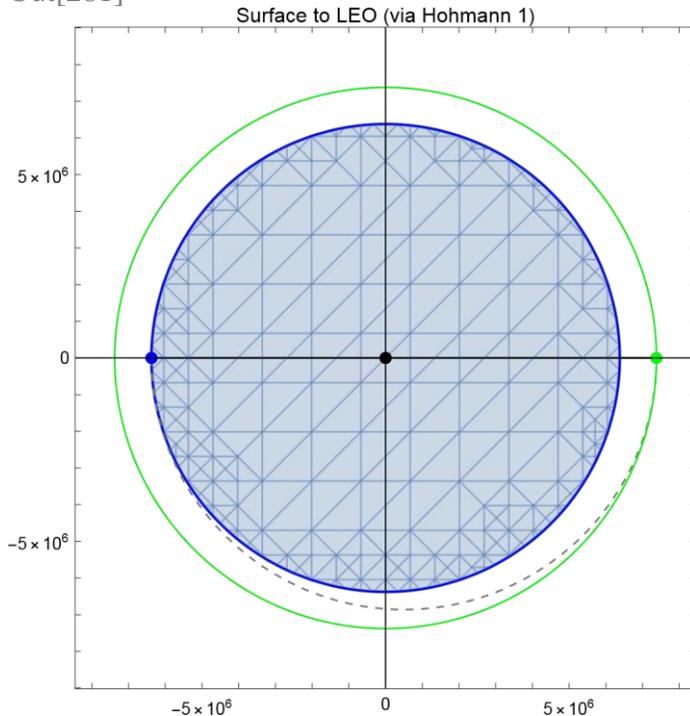
In[282]:=

Export["SurfacetoLEO.png",%]

Out[282]=

107

SurfacetoLEO.png

---

2. Geocentric Hohmann Transfer 2 (LEO to Lunar SOI, Phase II)

Since the Moon orbits within the Earth' s SOI, any transfer from an LEO to the Moon SOI will be governed by the Earth's gravity not the Sun's gravity.

In[284]:=

rMorbEa/rSOIE

Out[284]=

0.438954

Here, we perform a second Hohmann transfer from a parking orbit at low altitude (LEO) to the Moon' s

SOI with a simultaneous plane change to account from the Moon's deviation from the ecliptic (SunEarth) plane. Note that the s/c leaves on the *left* side, after orbiting the Earth in counterclockwise fashion until the best time for the next maneuver.

In[285]:=

rt2p=ro(* m *)

Out[285]=

7.37814×10^6

In[286]:=

rt2a=rMorbEp-rSOIM(* m *)

Out[286]=

2.97375×10^8

In[287]:=

at2=(rt2a+rt2p)/2(* m *)

Out[287]=

1.52377×10^8

In[288]:=

ept2=-mu/(2at2)(* J/kg *)

Out[288]=

-1.30794×10^6

In[289]:=

et2=(rt2a-rt2p)/(rt2a+rt2p)(* unitless *)

Out[289]=

0.95158

In[290]:=

pt2=at2(1-et2^2)(* m *)

Out[290]=

1.4399×10^7

In[291]:=

ht2=Sqrt[pt2mu](* m^2/s *)

Out[291]=

7.57592×10^{10}

In[292]:=

Vt2p=Sqrt[2(ept2+mu/rt2p)](* m/s *)

Out[292]=

10268.1

In[293]:=

Vt2a=Sqrt[2(ept2+mu/rt2a)](* m/s *)

Out[293]=

254.759

Diagram 2: LEO to Lunar SOI

In[294]:=

Apse=Plot[0,{x,-rt2p,rt2a},Frame□True,PlotStyle□{Black,Thickness[0.003]}];
MoonOrbit=PolarPlot[rt2a/(1+0Cos[θ]),{θ,0,2Pi},
Frame□True,PlotStyle□{Red,Thickness[0.003]},AspectRatio□True]; Hohmann2=PolarPlot[pt2/(1-
et2Cos[θ]),{θ,Pi,2Pi},Frame□True, PlotStyle□{Dashed,Gray,Thickness[0.003]},AspectRatio□True];
LEO=PolarPlot[ro/(1+0Cos[θ]),{θ,0,2Pi},Frame□True,
PlotStyle□{Green,Thickness[0.003]},AspectRatio□True]; Show[Apse,LEO,Hohmann2,MoonOrbit,
Graphics[{PointSize[0.02],Blue,Point[{0,0}]}],
Graphics[{PointSize[0.02],Green,Point[{roCos[Pi],0}]}],
Graphics[{PointSize[0.02],Red,Point[{rt2aCos[0],rt2aSin[0]}]}], PlotRange□{{-1.1rt2a,1.1rt2a},{-
1.1rt2a,1.1rt2a}}, AspectRatio□True,PlotLabel□"LEO to Lunar SOI (via Hohmann 2)"]

Out[298]=
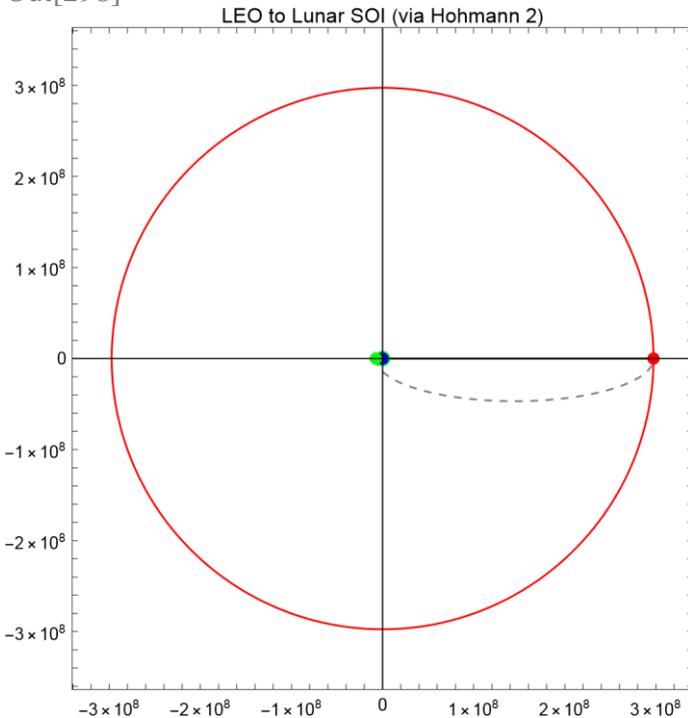
In[299]:=

Export["LEOtoMoonSOI.png",%]

Out[299]=

LEOtoMoonSOI.png

In[300]:=

---

3. Capture (Lunar SOI to LMO, Phase III)

At the edge of the lunar SOI, the spacecraft will follow a flyby hyperbola, but at the perilune (periapsis at the Moon), it will boost to slow down into a low moon orbit (LMO).

In[301]:=
Vi=Vt2a(* m/s *)
Out[301]=
254.759

In[302]:=
Vpl=VMorbEp(* Moon orbital speed at perigee, m/s *)
Out[302]=
1075.34

In[303]:=
α=0;(* rad *)

In[304]:=
Vinfi=Sqrt[Vi^2+Vpl^2-2ViVplCos[α]](* m/s *)
Out[304]=
820.585

In[305]:=
epC=Vinfi^2/2-muM/rSOIM(* J/kg *)
Out[305]=
262644.

In[306]:=
aC=-muM/(2epC)(* m *)
Out[306]=
-9.33749×10^6

In[307]:=
zpC=500×1000(* m *)
Out[307]=
500000

In[308]:=
rpC=zpC+RM(* m *)
Out[308]=
2.2374×10^6

In[309]:=
VpC=Sqrt[2(epC+muM/rpC)](* m/s *)
Out[309]=
2215.79

In[310]:=
eC=1-rpC/aC(* unitless *)
Out[310]=
1.23961

In[311]:=
pC=aC(1-eC^2)(* m *)
Out[311]=
5.01091×10^6

In[312]:=
θI=ArcCos[(1/eC)(pC/rSOIM-1)](* rad *)

110

Out[312]=

2.41236

In[313]:=

%*180/Pi(* deg *)

Out[313]=

138.218

In[314]:=

θInf=ArcCos[-(1/eC)](* rad *)

Out[314]=

2.50935

In[315]:=

%*180/Pi(* deg *)

Out[315]=

143.775

3a: Lunar SOI Entry to Capture LMO (SOI)

In[316]:=

FlybyOrbit=PolarPlot[pC/(1+eCCos[θ]),{θ,-θInf,0},Frame□True,
PlotStyle□{Dashed,Gray,Thickness[0.003]},AspectRatio□True];
MoonSOI=PolarPlot[rSOIM/(1+0Cos[θ]),{θ,0,2Pi},Frame□True,
PlotStyle□{Black,Dotted,Thickness[0.003]},AspectRatio□True];
LMO=PolarPlot[rM2/(1+0Cos[θ+θInf/2]),{θ,0,2Pi},Frame□True,
PlotStyle□{Brown,Thickness[0.003]},AspectRatio□True; Moon=
RegionPlot[x^2+y^2≤RM^2,{x,-2RM,2RM},{y,-2RM,2RM},PlotStyle□{Gray}];
Show[Moon,FlybyOrbit,LMO,MoonSOI, Graphics[{PointSize[0.02],Gray,Point[{0,0}]}],
PlotRange□{{-1.1rSOIM,1.1rSOIM},{-1.1rSOIM,1.1rSOIM}}, AspectRatio□True,PlotLabel□"Lunar
SOI Entry and Lunar Capture/LMO"]

Out[320]=

Lunar SOI Entry and Lunar Capture/LMO
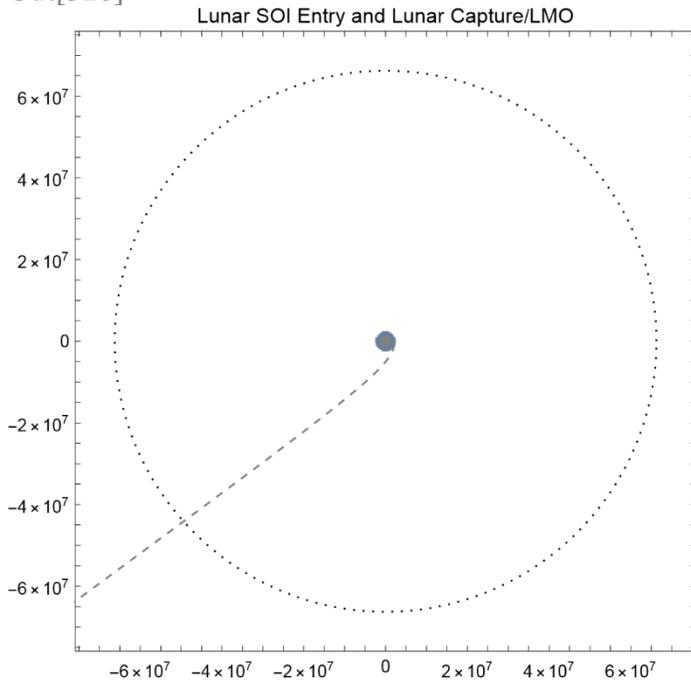
In[321]:=
Export["MoonSOIEntrytoCapture.png",%]
Out[321]=
MoonSOIEntrytoCapture.png
In[322]:=
LMO (Circular, Pole-to-Pole)
In[323]:=
rM2=zpC+RM(* m *)
Out[323]=
2.2374×10^6
In[324]:=
epM2=-muM/(2rM2)(* J/kg *)
Out[324]=
-1.09611×10^6
In[325]:=
VM2=Sqrt[muM/rM2](* m/s *)
Out[325]=
1480.61
In[326]:=

In[327]:=

FlybyOrbit=PolarPlot[pC/(1+eCCos[θ]),{θ,-θI,0},Frame□True,
PlotStyle□{Dashed,Gray,Thickness[0.003]},AspectRatio□True];
MoonSOI=PolarPlot[rSOIM/(1+0Cos[θ]),{θ,0,2Pi},Frame□True,
PlotStyle□{Black,Dotted,Thickness[0.003]},AspectRatio□True];
LMO=PolarPlot[rM2/(1+0Cos[θ+θInf/2]),{θ,0,2Pi},Frame□True,
PlotStyle□{Brown,Thickness[0.003]},AspectRatio□True]; Moon=
RegionPlot[x^2+y^2≤RM^2,{x,-2RM,2RM},{y,-2RM,2RM},PlotStyle□{Gray}];
Show[Moon,FlybyOrbit,LMO, Graphics[{PointSize[0.02],Brown,Point[{rM2Cos[0],rM2Sin[0]}]}],
PlotRange□{{-2rM2,2rM2},{-2rM2,2rM2}}, AspectRatio□True,PlotLabel□"Lunar Capture/LMO"]

Out[331]=

Lunar Capture/LMO
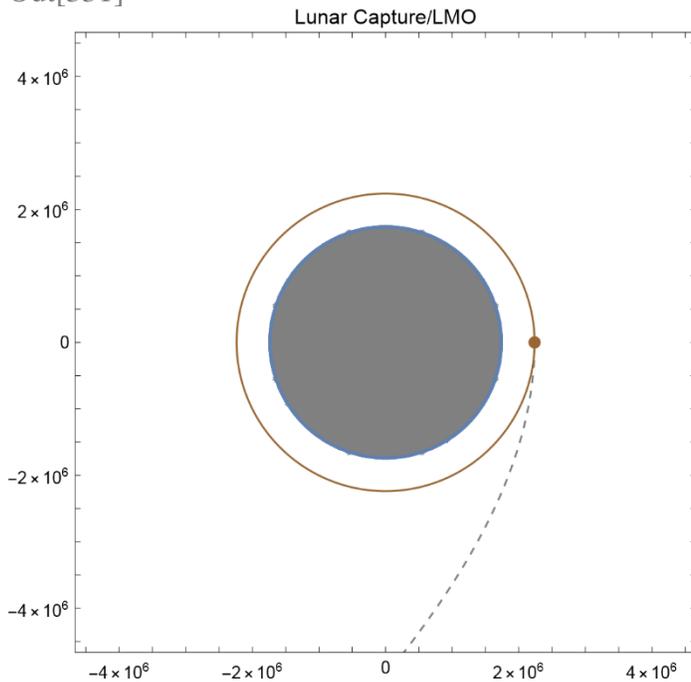
In[332]:=

Export["CapturetoLMO.png",%]

Out[332]=

CapturetoLMO.png

In[333]:=

---

4. Rover Release (LMO to LPO, Phase IV)

At the Moon the spacecraft will descend from an LMO to a low perilune orbit (LPO) to facilitate release, follow-up communication, and recovery of the rover. LPO (Elliptical, Pole-to-Pole)

In[334]:=

zMp=25×1000(* altitude, m *)

Out[334]=

25000

In[335]:=

rMp=zMp+RM(* m *)

Out[335]=

1.7624×10^6

In[336]:=

rMa=rM2(* m *)

Out[336]=

2.2374×10^6

In[337]:=

eM=(rMa-rMp)/(rMa+rMp)

Out[337]=

0.118756

In[338]:=

aM=(rMa+rMp)/2(* m *)

Out[338]=

1.9999×10^6

In[339]:=

epM=-muM/(2aM)(* J/kg *)

Out[339]=

-1.22628×10^6

In[340]:=

VMp=Sqrt[2(epM+muM/rMp)](* m/s *)

Out[340]=

1764.53

In[341]:=

VMa=Sqrt[2(epM+muM/rMa)](* m/s *)

Out[341]=

1389.92

In[342]:=

pM=aM(1-eM^2)(* m *)

Out[342]=

1.9717×10^6

In[343]:=

hM=Sqrt[pMmuM](* m^2/s *)

Out[343]=

3.10981×10^9

5: LMO to/from LPO (Lunar S. Pole)

In[344]:=

DropOffOrbit=PolarPlot[pM/(1+eMCos[θ+Pi/2]),{θ,0,2Pi},Frame☐True,
PlotStyle☐{Dashed,Gray,Thickness[0.003]},AspectRatio☐True];
LMO=PolarPlot[rM2/(1+0Cos[θ+Pi/2]),{θ,0,2Pi},Frame☐True,
PlotStyle☐{Brown,Thickness[0.003]},AspectRatio☐True]; Moon=
RegionPlot[x^2+y^2≤RM^2,{x,-2RM,2RM},{y,-2RM,2RM},PlotStyle☐{Gray}];
Show[Moon,DropOffOrbit,LMO,
Graphics[{PointSize[0.02],Brown,Point[{rM2Cos[Pi/2],rM2Sin[Pi/2]}]}],
Graphics[{PointSize[0.02],Black,Point[{rMpCos[3Pi/2],rMpSin[3Pi/2]}]}], PlotRange☐{{-
1.1rM2,1.1rM2},{-1.1rM2,1.1rM2}}, AspectRatio☐True,PlotLabel☐"LMO to/from LPO (Lunar
South Pole)"]

LMO to/from LPO (Lunar South Pole)
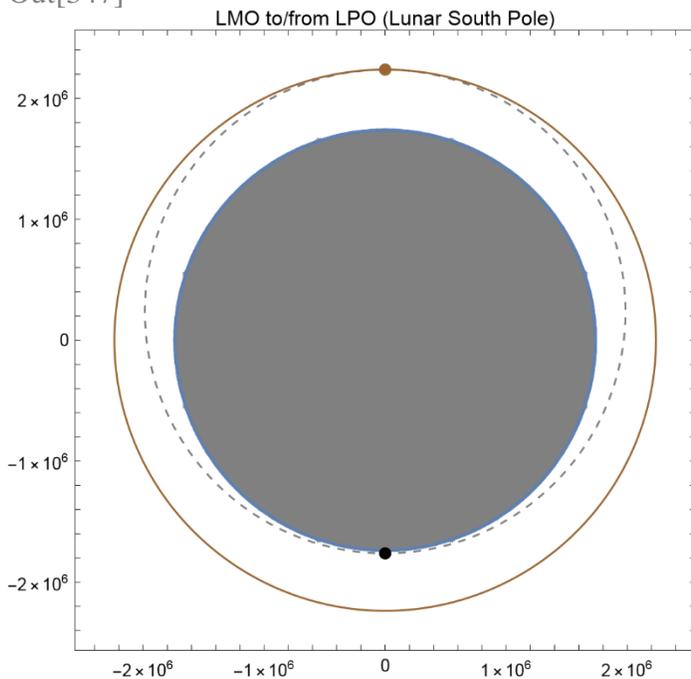
In[348]:=
Export["LMOtoLPO.png",%]
Out[348]= LMOtoLPO.png

Lander Release to the Moon

Small thrusters, parachutes, and/or air balloons are used to slow vertical descent.
5. Rover Return (LPO to LMO, Phase V)

Lander Launch from the Moon

Small thrusters are used to launch the rover from the Moon to LMO.

---

6. Lunar Escape (LMO to Lunar SOI, Phase VI)
Diagram 6a: LMO Exit to Lunar SOI (LMO)
In[349]:=
FlybyOrbit=PolarPlot[pC/(1+eCCos[θ]),{θ,0,θI},Frame□True,
PlotStyle□{Dashed,Gray,Thickness[0.003]},AspectRatio□True];
MoonSOI=PolarPlot[rSOIM/(1+0Cos[θ]),{θ,0,2Pi},Frame□True,
PlotStyle□{Black,Dotted,Thickness[0.003]},AspectRatio□True];
LMO=PolarPlot[rM2/(1+0Cos[θ+θInf/2]),{θ,0,2Pi},Frame□True,
PlotStyle□{Brown,Thickness[0.003]},AspectRatio□True; Moon=
RegionPlot[x^2+y^2≤RM^2,{x,-2RM,2RM},{y,-2RM,2RM},PlotStyle□{Gray}];
Show[Moon,FlybyOrbit,LMO, Graphics[{PointSize[0.02],Brown,Point[{rM2Cos[0],rM2Sin[0]}]}],
PlotRange□{{-2rM2,2rM2},{-2rM2,2rM2}}, AspectRatio□True,PlotLabel□"Exit from LMO"]
Out[353]=

Exit from LMO
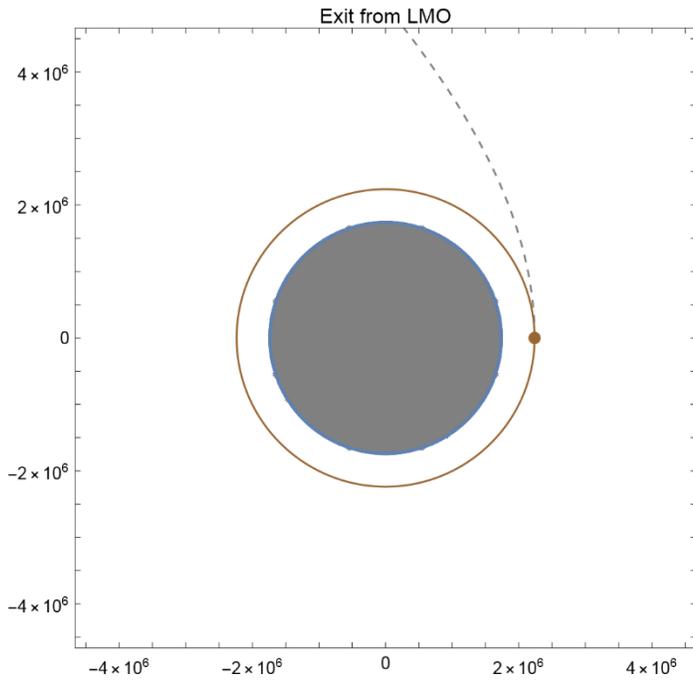
In[354]:=

Export["LMOExit.png",%]

Out[354]=

LMOExit.png

In[355]:=

In[356]:=

**FlybyOrbit=PolarPlot[pC/(1+eCCos[θ]),{θ,0,θInf},Frame⧠True,
PlotStyle⧠{Dashed,Gray,Thickness[0.003]},AspectRatio⧠True];
MoonSOI=PolarPlot[rSOIM/(1+0Cos[θ]),{θ,0,2Pi},Frame⧠True,
PlotStyle⧠{Black,Dotted,Thickness[0.003]},AspectRatio⧠True];
LMO=PolarPlot[rM2/(1+0Cos[θ+θInf/2]),{θ,0,2Pi},Frame⧠True,
PlotStyle⧠{Brown,Thickness[0.003]},AspectRatio⧠True]; Moon=
RegionPlot[x^2+y^2≤RM^2,{x,-2RM,2RM},{y,-2RM,2RM},PlotStyle⧠{Gray}];**
Show[Moon,FlybyOrbit,LMO,MoonSOI, Graphics[{PointSize[0.02],Gray,Point[{0,0}]}],
PlotRange⧠{{-1.1rSOIM,1.1rSOIM},{-1.1rSOIM,1.1rSOIM}},
AspectRatio⧠True,PlotLabel⧠"LMO to Lunar SOI Exit"]
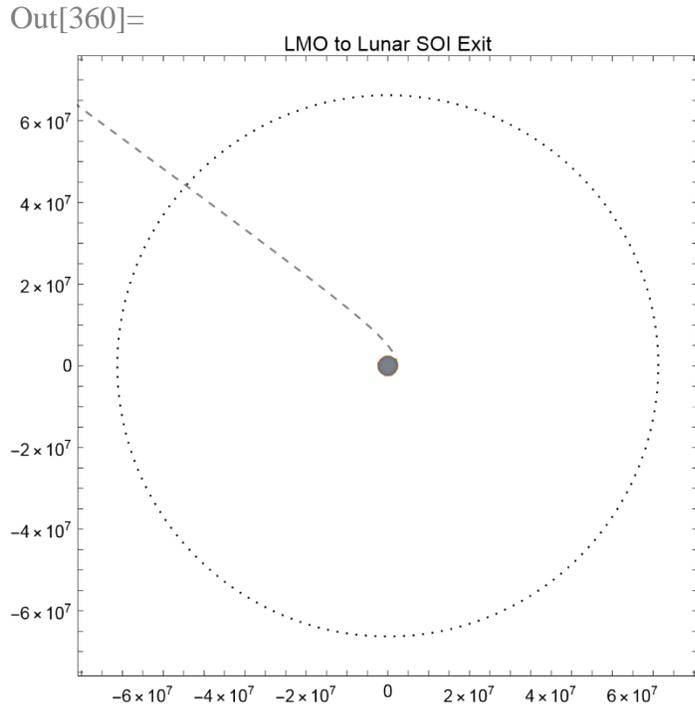
Out[360]=

In[361]:=

Export["LMOtoMoonSOIEscape.png",%]

Out[361]=

LMOtoMoonSOIEscape.png

In[362]:=

---

7. Geocentric Hohmann Transfer 3 plus Inclination Change (Lunar SOI to LEO, Phase VII)

In[363]:=

ro2=ro(* m *)

Out[363]=

117

7.37814×10^6

In[364]:=

rt3a=rMorbEp-rSOIM(* m *)

Out[364]=

2.97375×10^8

In[365]:=

rt3p=ro2;

In[366]:=

at3=(rt3a+rt3p)/2(* m *)

Out[366]=

1.52377×10^8

In[367]:=

ept3=-mu/(2at3)(* J/kg *)

Out[367]=

-1.30794×10^6

In[368]:=

et3=(rt3a-rt3p)/(rt3a+rt3p)(* unitless *)

Out[368]=

0.95158

In[369]:=

pt3=at3(1-et3^2)(* m *)

Out[369]=

1.4399×10^7

In[370]:=

ht3=Sqrt[pt3mu](* m^2/s *)

Out[370]=

7.57592×10^{10}

In[371]:=

Vt3p=Sqrt[2(ept3+mu/rt3p)](* m/s *)

Out[371]=

10268.1

In[372]:=

Vt3a=Sqrt[2(ept3+mu/rt3a)](* m/s *)

Out[372]=

254.759

Diagram 7: Lunar SOI to Earth Re-Entry

In[373]:=

Apse=Plot[0,{x,-rt3a,rt3p},Frame□True,PlotStyle□{Black,Thickness[0.003]}];
MoonOrbit=PolarPlot[rt3a/(1+0Cos[θ]),{θ,0,2Pi},Frame□True,
PlotStyle□{Green,Thickness[0.003]},AspectRatio□True];
Hohmann3=PolarPlot[pt3/(1+et3Cos[θ]),{θ,Pi,2Pi},Frame□True,
PlotStyle□{Dashed,Gray,Thickness[0.003]},AspectRatio□True];
LEO2=PolarPlot[ro2/(1+0Cos[θ]),{θ,0,2Pi},Frame□True,
PlotStyle□{Red,Thickness[0.003]},AspectRatio□True];
Show[Apse,LEO2,Hohmann3,MoonOrbit, Graphics[{PointSize[0.02],Blue,Point[{0,0}]}],
Graphics[{PointSize[0.02],Red,Point[{ro2Cos[0],ro2Sin[0]}]}],

Graphics[{PointSize[0.02],Green,Point[{rt3aCos[Pi],rt3aSin[Pi]}]}], PlotRange□{{-
1.1rt3a,1.1rt3a},{-1.1rt3a,1.1rt3a}}, AspectRatio□True,PlotLabel□"Moon SOI to LEO (via
Hohmann 3)"]

Moon SOI to LEO (via Hohmann 3)
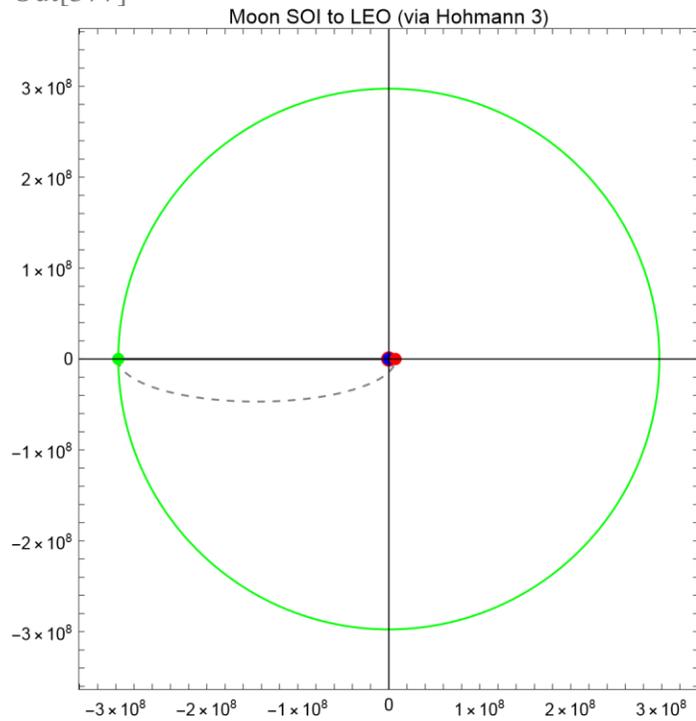
Export["MoonSOItoLEO.png",%]
MoonSOItoLEO.png

119

8. Earth Capture plus Inclination Change and Reentry (LEO to Surface, Phase VIII)
Diagram 8: LEO to Earth Surface (Re-Entry)
In[380]:=
Apse=Plot[0,{x,-rt1p,rt1a},Frame□True,PlotStyle□{Black,Thickness[0.003]}];
LEO2=PolarPlot[ro/(1+0Cos[θ]),{θ,0,2Pi},Frame□True,
PlotStyle□{Red,Thickness[0.003]},AspectRatio□True]; Hohmann4=PolarPlot[pt1/(1-et1Cos[θ]),{θ,0,Pi},Frame□True,
PlotStyle□{Dashed,Gray,Thickness[0.003]},AspectRatio□True];
Surface=PolarPlot[RE/(1+0Cos[θ]),{θ,0,2Pi},Frame□True,
PlotStyle□{Blue,Thickness[0.003]},AspectRatio□True]; Earth=RegionPlot[x^2+y^2≤RE^2,{x,-2RE,2RE},{y,-2RE,2RE}]; Show[Apse,Earth,Surface,Hohmann4,LEO2,
Graphics[{PointSize[0.02],Red,Point[{roCos[0],roSin[0]}]}],
Graphics[{PointSize[0.02],Black,Point[{0,0}]}],
Graphics[{PointSize[0.02],Blue,Point[{RECos[Pi],RESin[Pi]}]}], PlotRange□{{-1.1rt1a,1.1rt1a},{-1.1rt1a,1.1rt1a}}, AspectRatio□True,PlotLabel□"LEO to Surface (via Hohmann 4)"]
Out[385]=

LEO to Surface (via Hohmann 4)
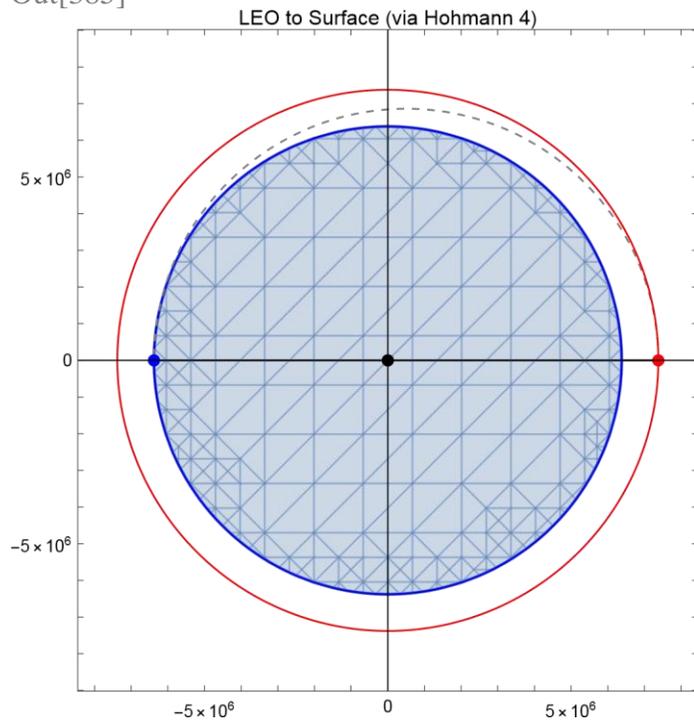
In[386]:=
Export["LEOtoSurface.png",%]
Out[386]=
LEOtoSurface.png
In[387]:=

Delta-V Calculations
To the Moon
Boost 1 : Surface to Hohmann 1
In[388]:=

120

λ=28.57Pi/180;(* Kennedy Space Center, Latitude, rad *)

In[389]:=

Vi1=464Cos[λ]//N(* Earth rotational speed, m/s *)

Out[389]=

407.5

In[390]:=

Vf1=Vt1p(* Perigee speed of Hohmann 1, m/s *)

Out[390]=

8187.66

In[391]:=

ΔV1=Vf1-Vi1(* m/s *)

Out[391]=

7780.16

Boost 2 : Hohmann 1 to LEO

In[392]:=

Vi2=Vt1a(* Apogee speed of Hohmann 1, m/s *)

Out[392]=

7077.94

In[393]:=

Vf2=Vo(* Orbital speed of LEO, m/s *)

Out[393]=

7350.14

In[394]:=

ΔV2=Vf2-Vi2(* m/s *)

Out[394]=

272.196

Boost 3 : LEO to Hohmann 2

In[395]:=

Vi3=Vo(* m/s *)

Out[395]=

7350.14

In[396]:=

Vf3=Vt2p(* m/s *)

Out[396]=

10268.1

In[397]:=

ΔV3=Vf3-Vi3(* m/s *)

Out[397]=

2917.93

Boost 4 : Hohmann 2 to SOI Entry Plane Change

In[398]:=

Δi=Pi/2+iMorbE; (* Equitorial to Polar Shift + Moon-Earth Inclination Difference, rad *)

In[399]:=

ΔV4=2Vt2aSin[Δi/2](* m/s *)

Out[399]=

376.092

In[402]:=

28.57(* Latitude of Kennedy Space Center *)

Out[402]=

28.57

In[403]:=

23.44+5.14(* Earth tilt + Earth-Moon Inclination Difference *)

Out[403]=

28.58

Boost 5: SOI Entry to LMO

In[404]:=

Vi5=VpC(* m/s *)

Out[404]=

2215.79

In[405]:=

Vf5=VM2(* m/s *)

Out[405]=

1480.61

In[406]:=

ΔV5=Vf5-Vi5(* m/s *)

Out[406]=

-735.176

Boost 6: LMO to LPO (Rover Release)

In[407]:=

Vi6=VM2(* m/s *)

Out[407]=

1480.61

In[408]:=

Vf6=VMa(* m/s *)

Out[408]=

1389.92

In[409]:=

ΔV6=Vf6-Vi6(* m/s *)

Out[409]=

-90.6935

To Earth

Boost 7: LPO to LMO (Rover Return)

In[410]:=

Vi7=VMa(* m/s *)

Out[410]=

1389.92

In[411]:=

Vf7=VM2(* m/s *)

Out[411]=

1480.61

In[412]:=

ΔV7=Vf7-Vi7(* m/s *)

Out[412]=

90.6935

Boost 8: LMO to SOI Exit

In[413]:=

Vi8=VM2(* m/s *)

Out[413]=

1480.61

In[414]:=

Vf8=VpC(* m/s *)

Out[414]=

2215.79

In[415]:=

ΔV8=Vf8-Vi8(* m/s *)

Out[415]=

735.176

Boost 9 : SOI Exit to Hohmann 3 Plane Change

In[416]:=

Δi=Pi/2+iMorbE; (* Equitorial to Polar Shift + Moon-Earth Inclination Difference, rad *)

In[417]:=

ΔV9=2Vt2aSin[Δi/2](* m/s *)

Out[417]=

376.092

Boost 10 : Hohmann 3 to LEO

In[418]:=

Vi10=Vt3p(* m/s *)

Out[418]=

10268.1

In[419]:=

Vf10=Vo(* m/s *)

Out[419]=

7350.14

In[420]:=

ΔV10=Vf10-Vi10(* m/s *)

Out[420]=

-2917.93

Boost 11: LEO to Hohmann 4

In[421]:=

Vi11=Vo

Out[421]=

7350.14

In[422]:=

Vf11=Vt1a

Out[422]=

7077.94

In[423]:=

ΔV11=Vf11-Vi11(* m/s *)

Out[423]=

-272.196

Boost 12 : Hohmann 4 to Surface

In[424]:=

Vi12=Vt1p(* Perigee speed of Hohmann 1, m/s *)

Out[424]=

8187.66

In[425]:=

λ=28.57Pi/180;(* Kennedy Space Center, Latitude, rad *)

In[426]:=

Vf12=464Cos[λ]//N(* Earth spin speed, m/s *)

Out[426]=

407.5

In[427]:=

ΔV12=Vf12-Vi12(* m/s *)

Out[427]=

-7780.16

Delta-V for Lunar Rover Mission (Launch to Drop Off)

In[428]:=

RoverDescentBoost=0-Sqrt[muM/rMp](* m/s *)

Out[428]=

-1668.25

In[429]:=

TotheMoon=Abs[ΔV1]+Abs[ΔV2]+Abs[ΔV3]+Abs[ΔV4]+Abs[ΔV5]+Abs[ΔV6](* m/s *)

Out[429]=

12172.2

In[430]:=

TotheMoon+Abs[RoverDescentBoost](* m/s *)

Out[430]=

13840.5

Delta-V for Lunar Rover Mission (Return to Re-Entry)

In[431]:=

RoverLiftOffBoost=Sqrt[muM/rMp]-0(* m/s *)

Out[431]=

1668.25

In[432]:=

TotheEarth=Abs[ΔV7]+Abs[ΔV8]+Abs[ΔV9] +Abs[ΔV10]+Abs[ΔV11]+Abs[ΔV12](* m/s *)

Out[432]=

12172.2

In[433]:=

TotheEarth+Abs[RoverLiftOffBoost](* m/s *)

Out[433]=

13840.5

Total Mission Delta-V

In[434]:=

RoverBoosts=2Sqrt[muM/rMp](* m/s *)

Out[434]=

3336.5

In[435]:=

TotheMoon+TotheEarth+RoverBoosts(* m/s *)

Out[435]=

27681.

In[436]:=

Time-of-Flight Calculations

Period LEO

In[437]:=

To=2PiSqrt[ro^3/mu]/(60×60×23.9344696)(* days *)

Out[437]=

0.0731989

In[438]:=

to=To/2(* days *)

Out[438]=

0.0365995

Hohmann Transfer 1 (Surface to LEO)

In[439]:=

Tt1=2PiSqrt[at1^3/mu]/(60×60×23.9344696)(* days *)

Out[439]=

0.0658857

In[440]:=

tt1=Tt1/2(* days *)

Out[440]=

0.0329428

Hohmann Transfer 2 (LEO to Lunar SOI)

In[441]:=

Tt2=2PiSqrt[at2^3/mu]/(60×60×23.9344696)(* days *)

Out[441]=

6.8701

In[442]:=

tt2=Tt2/2(* days *)

Out[442]=

3.43505

Lunar SOI Entry/Escape

In[443]:=

EC=ArcCosh[(eC+Cos[θI])/(1+eCCos[θI])]

Out[443]=

2.56368

In[444]:=

tSOI=Sqrt[(-aC)^3/muM](eCSinh[EC]-EC)/(60×60)(* hrs *)

Out[444]=

19.4535

In[445]:=

TM2=2PiSqrt[rM2^3/muM]/(60×60×23.9344696)(* days *)

Out[445]=

0.110193

In[446]:=

tM2=TM2

Out[446]=

0.110193

LMO/LPO

In[447]:=

TM=2PiSqrt[aM^3/muM]/(60×60×23.9344696)(* days *)

Out[447]=

0.093122

In[448]:=

tM=TM/2(* days *)

Out[448]=

0.046561

Minimum TOF from Launch to Rover Drop Off

In[449]:=

to+tt1+tt2+tM+tM2(* days *)

Out[449]=

3.66135

Minimum TOF from Recovery to Re-Entry

In[450]:=

to+tt1+tt2+tM+tM2(* days *)

Out[450]=

3.66135

Total Minimum Mission TOF (excluding wait time)

In[451]:=

2*%(* days *)

Out[451]=

7.32269

In[452]:=

Other Important Considerations

Lead Angle (Launch Considerations)

In[453]:=

ω=Sqrt[mu/rt2a^3](* Moon ang vel, rad/s *)

Out[453]=

3.89324×10^{-6}

In[454]:=

TOF=PiSqrt[at2^3/mu](* sec *)

Out[454]=

295978.

In[455]:=

(Pi-ωTOF)*180/Pi(* deg *)
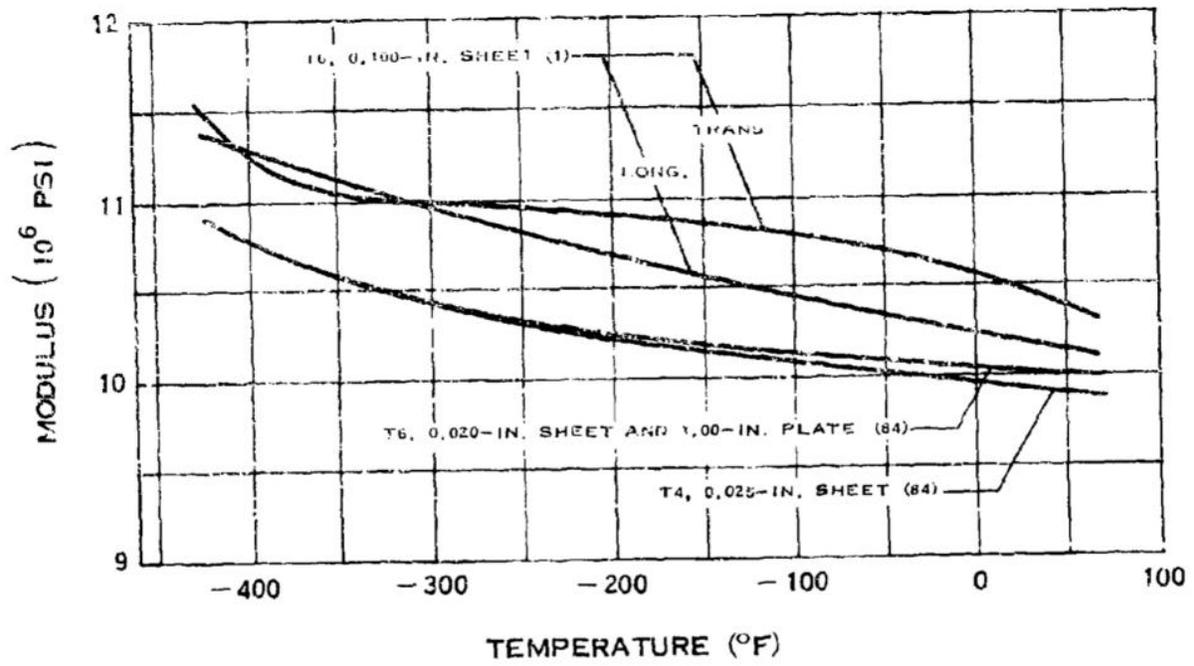
Out[455]=

113.977

Appendix B: 6061-T6 Aluminum Properties
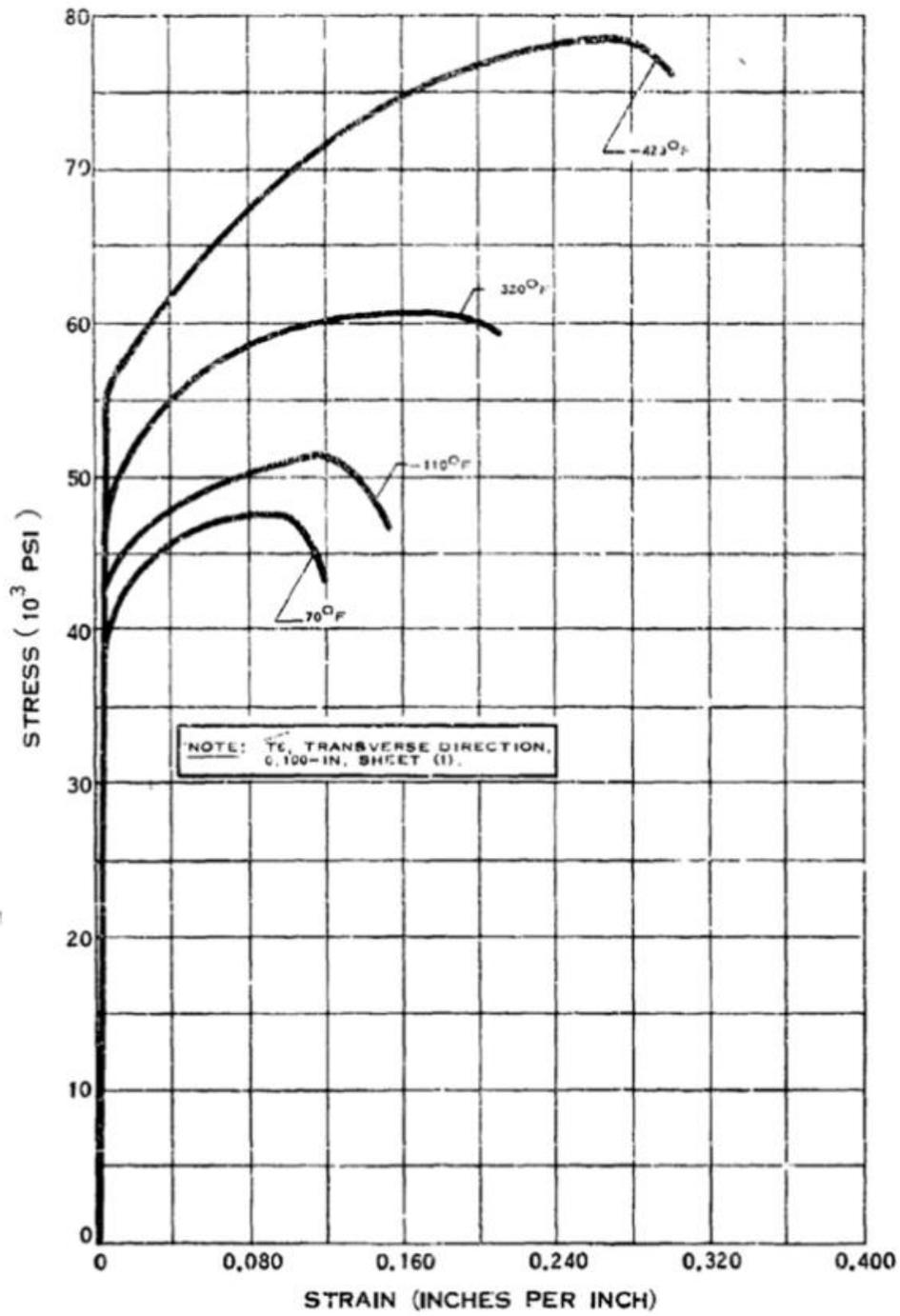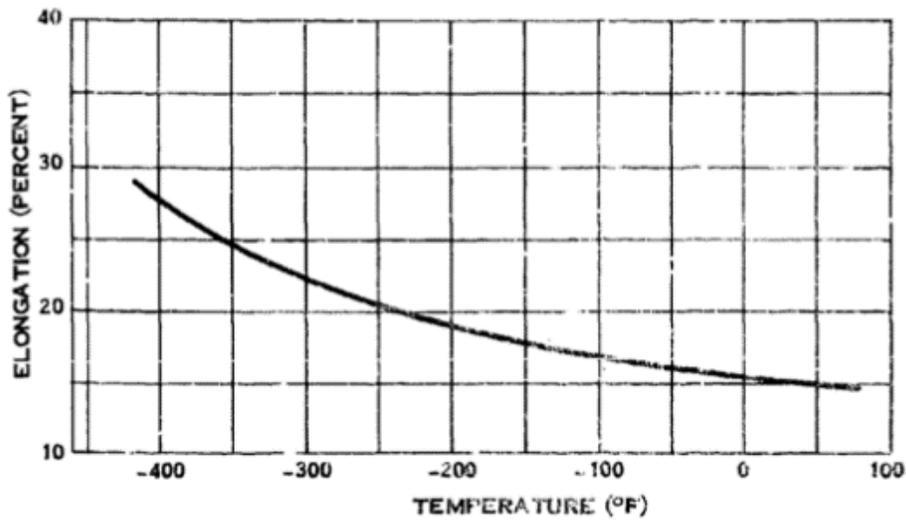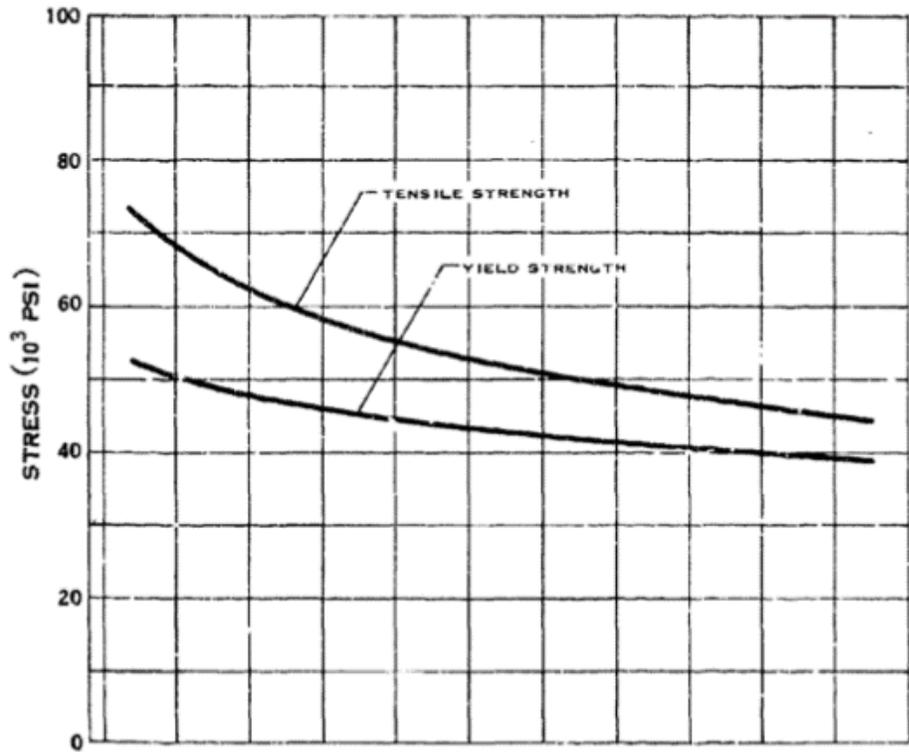
TYPICAL PROPERTIES OF 6061-T6 ALUMINUM

MODULUS OF ELASTICITY OF 6061
ALUMINUM

Appendix C: Electrical sub team's timeline by academic term

A-Term

	Week 1	Week 2	Week 3	Week 4	Week 5	Week 6	Week 7
	8/29 - 9/3	9/4 - 9/10	9/11 - 9/17	9/18 - 9/24	9/25 - 10/1	10/2 - 10/8	10/9 - 10/13
Literature review	███	███	███	███	███	███	███
Electrical components				███	███	███	
Programming							███

B- Term

	Week 8	Week 9	Week 10	Week 11	Week 12	Week 13	Week 14	Week 15
	10/24 - 29	10/30 - 11/5	11/6 - 11/12	11/13 - 11/19	11/20 - 11/22	11/28 - 12/3	12/4 - 12/10	12/11 - 12/16
Programming	███	███	███	███	███	███	███	███
Motor control		███	███	███	███	███	███	███
Path finding algorithm		███	███	███	███	███	███	███
Electronic integration	███	███	███	███	███			
Electrical components	███	███	███					

C-Term

	Week 16	Week 17	Week 18	Week 19	Week 20	Week 21	Week 22	Week 23
	1/10 - 1/14	1/15 - 1/21	1/22 - 1/28	1/29 - 2/4	2/5 - 2/11	2/12 - 2/18	2/19 - 2/25	2/26 - 3/4
Wiring	▓							
Research GPS/INS Electronics	▓	▓						
Report and Documentation	▓	▓	▓	▓	▓	▓	▓	▓
State Estimation/Sensor Fusion		▓	▓	▓				
Software Testing Prep Work		▓	▓	▓	▓			
Path Planning Algorithm		▓	▓	▓	▓	▓		
Motor Control Algorithm		▓	▓	▓	▓	▓		
Vehicle Simulation Model		▓	▓	▓	▓	▓		
Testing			▓	▓	▓	▓	▓	▓
Software Virtual Testing			░	░	░	░		
Software IRL Testing				░	░	░	░	░